Ultra-Stable Telescope Research and Analysis (ULTRA) Program

NASA ROSES 2017 D.15 Award

Phase 1 Report

April 1, 2019

Laura Coyle, Scott Knight, Allison Barto, Cody Allard
Ball Aerospace and Technologies Corp.

Matthew East, Conrad Wells, Keith Havey, Chris Sullivan, Lynn Allen
Harris Corporation

Jon Arenberg
Northrop Grumman Corporation Aerospace Systems

Todd Lawton, Kevin Patton, Bob Hellekson
Northrop Grumman Corporation Innovation Systems

Marcel Bluth, Matthew Nielsen, Austin Van Otten
SGT, a KBR Wyle Business Unit

Laurent Pueyo, Remi Soummer
Space Telescope Science Institute

Table of Contents

Acronym List

AI&T	Assembly, Integration and Test
AOS	Aft-Optics Subsystem/Structure
APLC	Apodized Pupil Lyot Coronagraph
CME	Coefficient of Moisture Expansion
COTS	Commercial Off-the-shelf
CTE	Coefficient of Thermal Expansion
CWFS	Continuous Wavefront Sensing
DFP	Disturbance Free Payload
DM	Deformable Mirror
DOF	Degree(s) of Freedom
DTA	Deployable Tower Assembly
FEA	Finite Element Analysis
FT	Fourier Transform
GSE	Ground Support Equipment
GSFC	Goddard Space Flight Center
HabEx	Habitable Exoplanet Observatory
HOWFS	High-Order Wavefront Sensor
IR	Infrared
JPL	Jet Propulsion Laboratory
JSC	Johnson Space Center
JWST	James Webb Space Telescope
L2	Sun-Earth Lagrange Point 2
LOS	Line of Sight
LOWFS	Low-Order Wavefront Sensor
LUVOIR	Large UV/Optical/Infrared Surveyor
mas	Milli-arcsecond

mK	Milli-Kelvin
MSFC	Marshall Space Flight Center
nm	Nanometers
OTA/OTE	Optical Telescope Assembly/Element
pm	Picometers
PM	Primary Mirror
PMBP	Primary Mirror Backplane (general)
PMBSS	Primary Mirror Backplane Support Structure (Webb-specific)
PMSA	Primary Mirror Segment Assembly
ppb / ppt	Parts per billion/trillion
PSD	Power Spectral Density
PSF	Point Spread Function
PTT	Piston, Tip and Tilt
RMS	Root-mean-square
ROC	Radius of Curvature
RSS	Root-sum-of-squares
SAO	Smithsonian Astrophysical Observatory
SF	Set and Forget
SFE	Surface Figure Error
SiC	Silicon Carbide
SM/SMA	Secondary Mirror (Assembly)
SOTA	State of the Art
STDT	Science and Technology Definition Team
TPF	Terrestrial Planet Finder
TRL	Technology Readiness Level
ULE®	Ultra-Low Expansion Glass, ULE® 7972 titania-silicate glass is a Corning, Inc. product

ULTRA	Ultra-Stable Large Telescope Research and Analysis (this study)
UV	Ultraviolet
VIPPS	Vibration Isolation and Precision Pointing System (Lockheed Martin)
WFE	Wavefront error
WFIRST	Wide Field Infrared Survey Telescope
WFSC	Wavefront Sensing and Control
ZERODUR®	Low expansion glass ceramic is a SCHOTT AG Advanced Optics product

1   Executive Summary

This report documents the results from Phase 1 of the Ultra-Stable Large Telescope Research and Analysis (ULTRA) study. The contract was awarded to our industry team (Ball Aerospace, Harris Corp., Northrop Grumman Corp. Aerospace Systems, Northrop Grumman Corp. Innovation Systems, SGT and the Space Telescope Science Institute) through the NASA ROSES-17 solicitation, element D.15[1] – which calls for a one-year system-level engineering design and modeling study for a >10-m class UV/optical/IR segmented-aperture telescope with sub-nanometer wavefront stability.

This challenging stability requirement is driven by the science goal to directly image and characterize exo-Earths with a high contrast coronagraph. Two mission concepts requiring sub-nanometer stability are the Large UV/Optical/Infrared Surveyor (LUVOIR)[2] and the Habitable Exoplanet Observatory (HabEx)[3], both of which are under consideration by the 2020 Astrophysics Decadal Survey. This study augments the work completed by the LUVOIR and HabEx Science and Technology Definition Teams (STDTs) and their NASA center engineering teams[4,5] by identifying and prioritizing key technologies for near-term development that will result in credible system architectures. While this study uses these mission concepts (especially LUVOIR) to perform specific assessments, the findings are applicable to similar architectures with comparable stability needs.

Our approach is a holistic systems architecture study treating the observatory, telescope and coronagraph as a complete system and considering the impacts of instability in both the temporal and spatial domains. It is guided via the formalism of error budgets, where sub-system allocations are compared to current capabilities, often including trade studies of potential technologies or approaches. Technology gaps are identified where current capabilities will not meet allocations and roadmaps are provided to prioritize and propose a path forward for development of the most urgent technologies. The resulting technology gap list, gap classification and technology development road map for the work performed in this study are shown in **Figure 1, Table 1** and **Figure 2**, respectively. The general approach for maturing key technologies is to demonstrate them

---

[1] NASA ROSES D.15 Element
https://nspires.nasaprs.com/external/viewrepositorydocument/cmdocumentid=602546/solicitationId=%7B7537A31 C-AA12-E8D0-F3CF-2BD999B21B0A%7D/viewSolicitationDocument=1/D.15%20SLSTD%20Amend%2050.pdf.

[2] Matthew R. Bolcar, "The Large UV/Optical/Infrared Surveyor (LUVOIR): Decadal Mission concept technology development overview," Proc. SPIE 10398 (5 September 2017).

[3] Phil Stahl, "Overview of a telescope concept design for the Habitable-zone Exoplanet Direct Imaging Mission," SPIE Conference: UV/Optical/IR Space Telescopes and Instruments: Innovative Technologies and Concepts VIII, (September 2017).

[4] Matthew R. Bolcar, Kunjithapatham Balasubramanian, Julie Crooke, Lee Feinberg, Manuel Quijada, Bernard J. Rauscher, David Redding, Norman Rioux, Stuart Shaklan, H. Philip Stahl, Carl M. Stahle, Harley Thronson, "Technology gap assessment for a future large-aperture ultraviolet-optical-infrared space telescope," J. Astron. Telesc. Instrum. Syst. 2(4), 041209 (2016).

[5] Rhonda Morgan, Keith Warfield, Gary Kuan, H. Phil P. Stahl, Bertrand Mennesson, Bala Balasubramanian, Dimitri Mawet, Shouleh Nikzad, Joel Nissen, Stuart Shaklan, Eugene Serabyn, Karl Stapelfeldt, Steven Warwick, "Technology maturity for the habitable-zone exoplanet imaging observatory (HabEx) concept," Proc. SPIE 10698, Space Telescopes and Instrumentation 2018: Optical, Infrared, and Millimeter Wave, 106980S (6 July 2018).

at the component level, then combine them in sub-system testbeds to gain understanding of the interactions early in the development process, then continue to build up higher fidelity testbeds.

Area	Active Sensing & Control				Low Disturbance			Structures			Mirrors and Mirror Mounting					Path Forward for TRL Advancement
Technology	Segment Dynamic Sensing & Control	Laser Metrology	System Control Methodology	Thermal Sensing & Control	LOS Stability	Payload Isolation	Low Disturbance Mechanisms	Stable Composite Structures	Microdynamics	Stable Joining (Hinges/Latches)	Stable Mirrors	Mirror Mounting	PMSA Figure Actuation (if needed)	Coronagraph Design (LOWFS/HOWFS)	Infrastructure/ External Metrology	
Current TRL	3	5	2	4	3	5	2	5	2	4	5	4	3	4/5	-	
Knowledge Gap	X		X	X	X		X		X	X		X	(X)			Analysis/ Measurements
Low-TRL Gap	**X**		**X**		**X**								**(X)**			**Component-Level Demo**
Mid-TRL Gap				**X**						**X**		**X**				**Analysis/ Subsystem Demo**
Engineering Gap		X				X		X			X				X	Analysis
System-Level Gap		X				X			X			X				System/ Subsystem Demos
Showstopper																Unknown

Figure 1: ULTRA Study Technology Gap List. Includes current TRL, gap classification (see Table 1 for definitions), and suggested path forward for TRL advancement. Technology gaps were identified using the LUVOIR Architecture A as the baseline design. Low TRL gaps are the highest priority for near term development. See Section 12 for more detail.

Table 1: Classification of technology gaps.

Knowledge Gap	Do not have measurements or knowledge of performance at the picometer level, but do not know of anything yet that will cause an issue. May transition to Low- or Mid-TRL gap as knowledge is gained.
Low-TRL Gap	Technologies are identified but need development to show they are feasible.
Mid-TRL Gap	Current technologies appear feasible but need to be proved in flight-like ways through brassboards.
Engineering / Manufacturing Gap	A solution is available, but it takes engineering and process work to make sure it can be built to cost and schedule.
System-Level Gap	Components or subsystems have been proven but need to be integrated into a larger system to characterize interactions.
Architectural Show Stopper	No known technologies can provide a solution.

Figure 2: Roadmap for component and subscale, subsystem demonstrations for ultra-stable optical systems with segmented primary mirrors. This roadmap leverages work being done at NASA centers, universities and industry through a variety of programs (NASA ROSES, IRAD, etc.).

There is a need to balance the most promising technologies with the existing cost and schedule resources. The full development path in **Figure 2** will take a significant amount of time and funding, so the ULTRA study team has identified several areas for near-term investment (the next 2-3 years) listed in **Table 2.** These are the priority for understanding and substantiating the technical and fiscal feasibility of LUVOIR.

Within these near-term activities, there are a few areas that are critical for success of the proposed LUVOIR architecture. The results from the ULTRA study corroborate previous analysis that mid spatial frequencies (especially segment-level piston-tip-tilt) will be most damaging to contrast stability in the coronagraph. Thus, low-TRL active sensing and control technologies at the segment level should be given highest priority. In addition, an assessment of the structural stability due to microdynamics and other non-linear impulses as well as the line-of-sight (LOS) stability using payload isolation should also be investigated as soon as possible. If the results reveal state of the art (SOTA) techniques are not sufficient, other solutions are currently low-TRL. These priorities will tackle the most difficult parts of the stability problem with the longest lead times first and provide a solid foundation for additional demonstrations and testbeds.

Table 2: Top level priorities that can achieve significant advancement in the next 2-3 years. The most difficult aspects of the stability problem and thus the highest priorities are underlined for emphasis.

Modeling/Analysis	o Cross check first order PSD-based stability budgets with end-to-end modeling. o Develop structural and thermal LUVOIR models rooted in known/expected material capability (these models could also be made available to the ultra-stable community as a common platform to evaluate other system elements; some models already in progress from STDT work). o Model nested controls systems.
Component/Subsystem Demonstrations	o <u>Prove stability of hinges/latches with simple deployable tube section, including microdynamics regime.</u> o <u>Prove LOS stability at milliarcsecond level (DFP).</u> o Prove millikelvin thermal sensing and control in structures, light-weighted optics. o <u>Prove picometer-level edge sensing in flight-like geometry at required bandwidth.</u> o <u>Prove picometer-level actuation at required bandwidth and loading; characterize induced dynamics.</u> o Prove integration of sensing/control technologies into PMSAs. o Prove stability of PMSA mounting approach. o Characterize stability of Mirror Cell Subsystem Testbed. o Characterize interaction of nested controls in Control Architecture Testbed.
Facilities/Metrology	o Continue investments in NASA and university facilities to advance precision metrology and environmental facilities capable of ultra-stable measurements. o Leverage above resources to complete component-level demonstrations in a relevant environment (including measurement of stability-related material properties)

2 ULTRA Study

2.1 Study Milestones and Results

The key technical milestones of the ULTRA study are:
1. Develop technical details of time domain aspect of stability, controls and coronagraph observations.
2. Develop thorough list of on-board and off-board disturbances important at picometer levels.
3. Develop trade space for technologies/architectures.
4. Develop technology gaps/roadmaps.

The results presented in this study address all four of the objectives stated above with no major changes in scope. However, it was known that the study would be an iterative process, especially when developing the stability budget, so for the first cycle the focus was on first-order sensitivity analysis rather than end-to-end simulations. This approach yielded significant insight into the technology gaps for ultra-stable segmented mirror architectures and is an appropriate methodology for a system with many open trades. It also allowed the team members to study specific areas of ultra-stability in parallel, maximizing the efficiency of the one-year study.

2.2 Lessons Learned and Risks for Future Work

It is the recommendation of the study team that future work should focus on the PSD-based error budgeting approach to provide maximum relief to the sub-systems (see Section 4.6) and that another cycle of analysis should be run leveraging the first order results from this study. It is not expected that the next cycle will significantly alter the technology priorities identified in this report, but it will yield additional knowledge for the refinement of the stability budgets and the interaction of systems. This may have implications for the detailed performance requirements for the technology gaps discussed in the study.

For each technology gap, the team has identified a path forward for development, but there is some risk that not all gaps can be closed. To mitigate this risk, the lowest TRL technologies are recommended for immediate development. It is also recommended that sub-system interactions also be understood early in the process with near-term testbed demonstrations. If these demonstrations fall short of the needed performance, architectural changes or other technologies in the trade space can be investigated. Finding these shortfalls as early as possible in the development process should reduce cost and schedule impacts to a later phase.

2.3 Interactions with STDTs

The ULTRA study team has been in close contact with the LUVOIR STDT and has received up-to-date opto-mechanical models and analyses that have aided our work. The team has also participated in regular telecons with the STDT members to share results and compare insights so results from the ULTRA study can be leveraged in their work. Study team members also interact with the HabEx STDT to understand their architectural concerns and share relevant results from ULTRA.

Results from the ULTRA study will be shared with the broader community through this report, submission of white papers to the 2020 Astrophysics Decadal Survey, presentations to relevant working groups (i.e. Exoplanet Technology Colloquium) and conference participation.

3 Systems Engineering Approach for Ultra-Stable Optical Systems

The ambitious science goals for future space telescope mission concepts often require large-area primary mirrors to achieve the high resolution and greater photon flux required to detect faint objects, such as Earth-like planets orbiting sun-like stars. To support these aperture increases and leverage NASA investments for the James Webb Space Telescope, some telescope designs are transitioning from monolithic to segmented primary mirrors. However, these same science goals also require the optical systems to produce highly stable wavefronts and segmentation of the primary mirror makes some aspects of system stability more difficult.

One of the most extreme wavefront stability requirements comes from the science goal of directly imaging exoplanets with a coronagraph, which requires the detection of an object ~10 billion times fainter than its host star. This 10^{-10} raw contrast corresponds to wavefront stability in some modes on the order of picometers.[6,7] While this value provides insight, in that optical systems will need to operate in a new regime of "ultra-stable optical systems" where the smallest units of concern are picometers rather than nanometers, the full picture is far more complex than that single metric and in some areas there are significantly larger allocations (see Section 4.4). Regardless, a passively stable system like the Hubble Space Telescope or Webb is limited to nanometer-level stability given the expected environmental/system-induced disturbances.[8,9] Some additional, active wavefront sensing and control (WFSC) and thermal sensing and control capability will be required beyond traditional passive approaches to achieve picometer-level stability. These types of active controls will be needed for both monolithic and segmented primary mirrors, though the segmented architecture will be more complex due to the larger number of degrees of freedom (DOFs) that must be controlled.

The ULTRA study performs a system-level engineering assessment to evaluate current methods for achieving stable telescopes and to identify areas where additional technologies can provide the three orders of magnitude improvement in optical stability, compared to Webb or Hubble, required for this application. This analysis must include evaluation of the system as a whole ("photons in to electrons out") to avoid placing overly restrictive requirements on sub-systems that will likely already be operating at or beyond their current capability. However, it is not practical to start with end-to-end simulations when much of the architecture is undefined – performing analysis in terms of "stability sensitivities" is a reasonable starting point for the first few iterations to narrow the trade space and identify technology gaps, which can then be used as inputs to more comprehensive modeling.

---

[6] Bijan Nemati, Mark T. Stahl, H. Philip Stahl, Stuart B. Shaklan, "The effects of space telescope primary mirror segment errors on coronagraph instrument performance," Proc. SPIE 10398, UV/Optical/IR Space Telescopes and Instruments: Innovative Technologies and Concepts VIII (5 September 2017).

[7] Bijan Nemati, H. Philip Stahl, Mark T. Stahl, Garreth Ruane, "HabEx Telescope WFE stability specification derived from coronagraph starlight leakage," Proc. SPIE 10743, Optical Modeling and Performance Predictions X, (17 September 2018).

[8] D. Scott Acton, et. al., "Wavefront sensing and controls for the James Webb Space Telescope," Proc. SPIE 8442, Space Telescopes and Instrumentation 2012: Optical, Infrared, and Millimeter Wave, 84422H (21 September 2012).

[9] John E. Krist, "High-contrast imaging with the Hubble Space Telescope: performance and lessons learned," Proc. SPIE 5487, Optical, Infrared, and Millimeter Space Telescopes, (12 October 2004).

Thus, a key feature of this study is that it is an iterative process to refine stability budgets, identify trade spaces, and evaluate technologies, as shown in **Figure 3**. While top level stability budget allocations are fixed by the coronagraph performance (optimization of the coronagraph design is outside the scope of this study, though it should be considered as part of a comprehensive approach to the ultra-stability problem), allocations to the various sub-systems can be rebalanced as the design matures to avoid excessive burden on any one component or technology. While significant progress has been made during this study, there is still more work to be done, especially in end-to-end simulations.
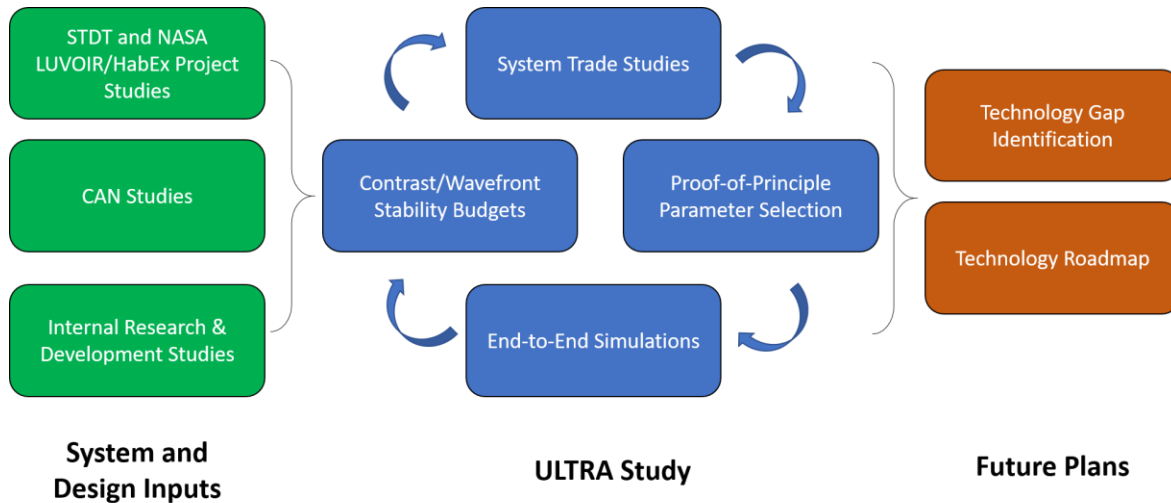
Figure 3: The study approach is an iterative process to refine stability budgets and define the system architecture, resulting in a list of current technology gaps and a roadmap for maturing them.

3.1   Baseline Design: LUVOIR Architecture A

Given the typical complexity of flagship missions, the trade space for a 10-m class, ultra-stable architecture is large. Our study team used "Architecture A" from the LUVOIR STDT as the baseline point design[10] but much of the approaches and results presented in this report are directly applicable to monolithic telescopes as well. LUVOIR Architecture A consists of a 15-meter diameter, segmented primary mirror in an on-axis, obscured configuration. The coronagraph is an Apodized Pupil Lyot (APLC) type with two internal deformable mirrors (DMs) that correct static optical field error to create a "dark hole" and can also correct some wavefront error drift on the order of 0.002 Hz (10-minute update rate) depending on the target star brightness. A coronagraph dark hole is a region of the detector with low background signal that can support high contrast imaging. The dark hole for an APLC is typically annular and centered on the host star under observation, as in **Figure 4**. The inner radius of the dark hole is called the "inner working angle" and sets the limit for how close a planet can be to its host star and still be detected. The outer radius of the dark hole is called the "outer working angle" and is limited by the spatial resolution of the DMs (approximately the number of actuators across the telescope pupil divided by 2). The

---

[10] Matthew R. Bolcar, Julie Crooke, Jason E. Hylan, Ginger Bronke, Christine Collins, James Corsetti, Joe Generie, Qian Gong, Tyler Groff, William Hayden, Andrew Jones, Bryan Matonak, Sang Park, Lia Sacks, Garrett West, Kan Yang, Neil Zimmerman, "The large UV/optical/infrared surveyor (LUVOIR): decadal mission study update," Proc. SPIE 10698, Space Telescopes and Instrumentation 2018: Optical, Infrared, and Millimeter Wave, (6 July 2018).

phrase "digging the dark hole" refers to the process by which the deformable mirrors are adjusted to correct for static errors in the telescope to create the annular region. This report is focused on stability – or "maintaining the dark hole".
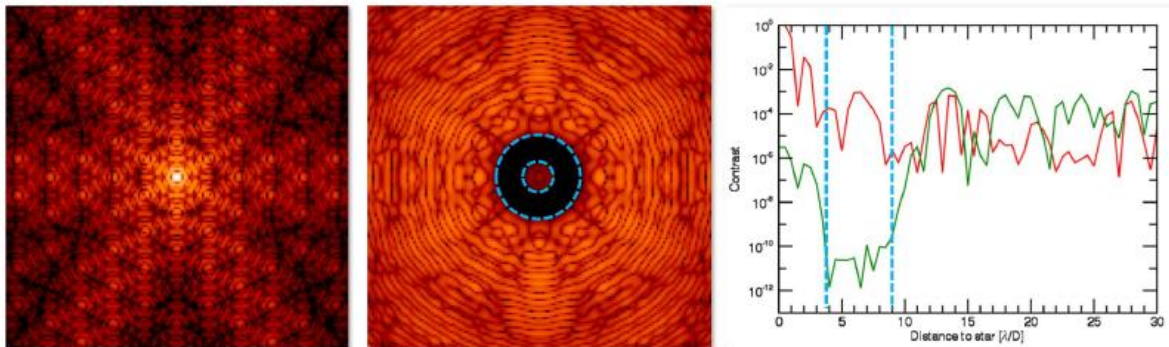
Figure 4: Left: The simulated PSF of a bright star with a segmented telescope and no coronagraph or aberrations (log scale). Center: The inclusion of a coronagraph creates an annular region with very low background called the "dark hole" where exoplanets can be detected. The inner and outer working angles are defined by the dotted blue lines. Right: A slice through both PSFs reveal the ability of the coronagraph to create very low contrast (~10^{-11}) in the dark hole annulus.[11]

While this study is focused on the stability requirements imposed by the most stringent instrument – the coronagraph – the system impacts of the various trade studies are also considered to ensure they do not adversely affect other instruments or systems. The notional active control system, pictured in **Figure 5**, consists of multiple loops operating at different temporal frequencies. These loops act together to sense and control the system wavefront to maintain the required stability.

---

[11] Lucie Leboulleux, Laurent Pueyo, Jean-François Sauvage, Thierry Fusco, Johan Mazoyer, Anand Sivaramakrishnan, Mamadou N'Diaye, Rémi Soummer, "Sensitivity analysis for high-contrast imaging with segmented space telescopes," Proc. SPIE 10698, Space Telescopes and Instrumentation 2018: Optical, Infrared, and Millimeter Wave, 106986H (6 July 2018).
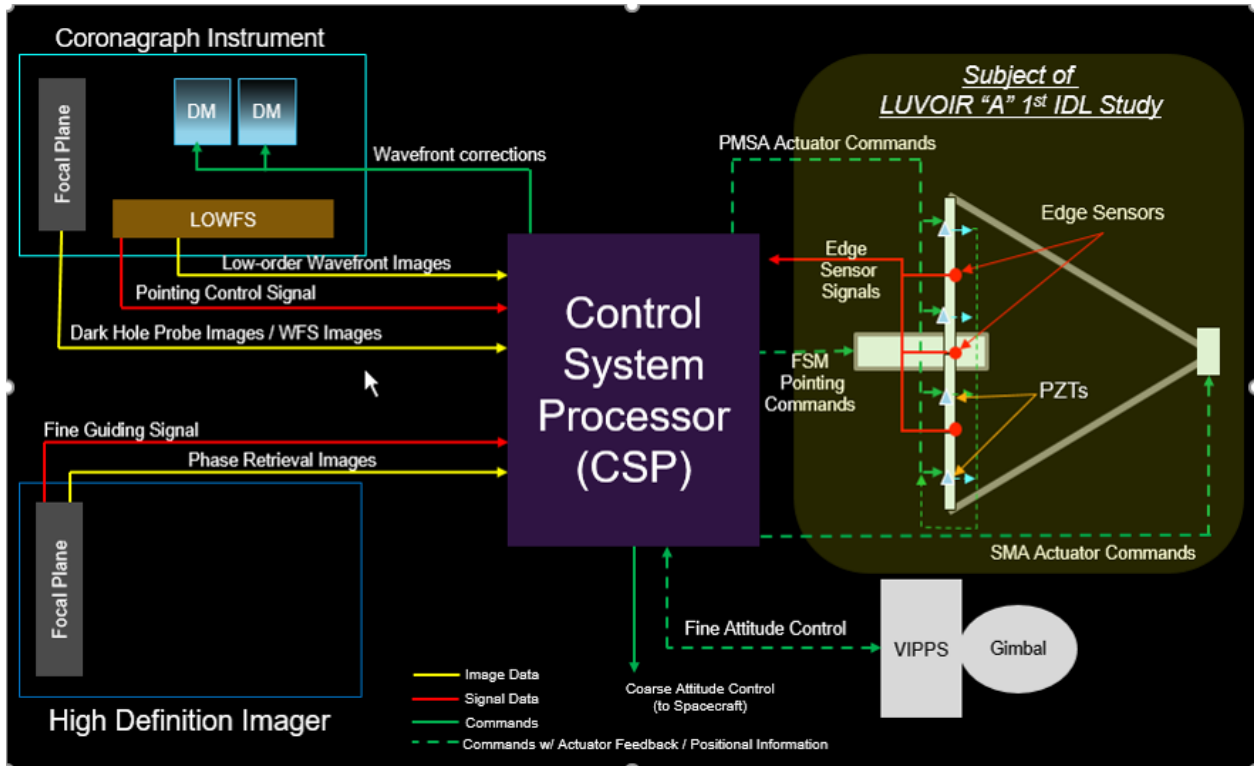
Figure 5: Notional control block diagram for LUVOIR Architecture A.[12] Multiple active sensing and control systems operating at a variety of spatial and temporal bands are required to produce picometer-level wavefront stability.

3.2   Spatial and Temporal Bandwidths

Previous work on LUVOIR coronagraph stability requirements have focused on the spatial domain, specifically considering "pupil" or "global" errors that are associated with monolithic modes of the primary mirror and independent errors on individual primary mirror segments (PMSAs). It is known that different spatial distributions of wavefront error will have different impacts on coronagraph contrast, with the most difficult requirement of "10 pm per 10 minutes" being driven by segment-level piston and tip/tilt over the course of a coronagraph observation.[6]

The temporal aspect of the requirements has not been studied in as much detail, which is why the temporal domain is a focus area for the ULTRA study. A comprehensive stability budget must consider the system disturbances, responses, and active control strategies in the various spatial and temporal domains. Ultimately, the system should be assessed over these domains as a continuum (described by curves) but a reasonable starting point is to bin frequencies based on breakpoints in the system design (i.e. primary mirror segmentation, control loop bandwidths, etc.) For the purposes of this report, the spatial frequencies bins are listed in **Table 3** and the temporal frequency bins are listed in **Table 4**.

---

[12] Lee Feinberg; Matthew Bolcar; Scott Knight; David Redding," Ultra-stable segmented telescope sensing and control architecture." Proc. SPIE Volume 10398, (2017).

Table 3: Definition of spatial frequency bins. The breakpoints have been chosen based on Architecture A segmentation, but could be updated for different segmentation approaches.

Bin Label	Spatial Frequency	Description
Low	2-4 cycles/diameter	Global alignment of PM; Low order PM modes (backplane); Can be compensated with SM motion
Mid	4-15 cycles/diameter	PMSA rigid body motion; Low order PMSA modes
High	15-60 cycles/diameter	PMSA mid spatial modes (i.e. mount print through)
High +	> 60 cycles/diameter	PMSA high spatial modes above the DM correction range (outside dark hole but considering aliasing into the science field)

Table 4: Definition of temporal frequency bins. The breakpoints have been chosen based on the notional bandwidth of the active sensing and control systems.

Bin Label	Temporal Frequency	Description
LF1	48 hours < F < 0.001 Hz	Observing scenario and Coronagraph high order wavefront sensor (HOWFS) bandwidth, depending on target star brightness
LF2	0.001 Hz < F < 0.01 Hz	Coronagraph Zernike low order wavefront sensor (LOWFS) bandwidth, depending on target star brightness
LF3	0.01 Hz < F < 1 Hz	Telescope alignment (PM/SM rigid body motion) bandwidth
MF	1 Hz < F < 10 Hz	PM segment-level rigid body sensing and control
HF	>10 Hz	Uncontrolled or effects removed with image processing

A visual summary of the temporal domain problem is shown in **Figure 6**. On its own, the coronagraph is most sensitive to "quasi-static" errors, or phenomena that drift on the order of an

exposure.[13,14] Very slow drifts will be mitigated by the observing scenario, wherein the observatory slews to a bright star to dig the dark hole then slews to the target star to collect data. This effectively chops the wavefront error at ~48-hour cadence and sets the lower limit on the temporal domain. Very fast drifts will cause blurring in the coronagraph focal plane, which causes a blurred "halo" that can be removed in image post-processing. Quasi-static disturbances that look like speckle evolution during the exposure will be the most confusing when trying to detect a planet.

Active sensing and control loops provide stability across a range of temporal frequencies. At low temporal frequencies (LF1/LF2), there are many loops working simultaneously, which will provide a multiplicative effect on the error attenuation and increase the allowable uncorrected wavefront error. At high temporal frequencies (HF), damping and isolation in combination with image post-processing also provide some relaxation on wavefront stability. At mid temporal frequencies (LF3/MF), there are fewer controls and the coronagraph has the highest sensitivity to errors, so this is the main region of concern for active wavefront and thermal controllers.
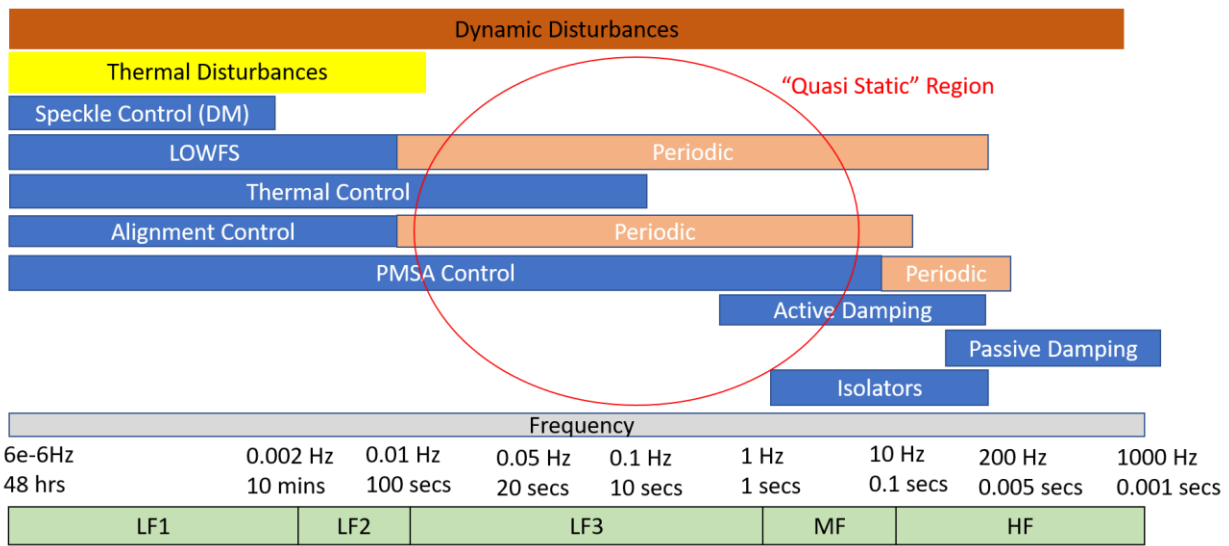
Figure 6: Expected disturbances and notional control systems in the temporal domain. The green bar represents the notional bandwidths of the frequency "bins" described in Table 4. The "quasi static" region is of highest concern since the coronagraph is most sensitive to errors in this frequency regime and there are fewer active/passive controls.

[13] Mark T. Stahl, Stuart B. Shaklan, H. Philip Stahl, "Preliminary analysis of effect of random segment errors on coronagraph performance," Proc. SPIE 9605, Techniques and Instrumentation for Detection of Exoplanets VII, 96050P (24 September 2015).

[14] Lucie Leboulleux, Jean-François Sauvage, Laurent A. Pueyo, Thierry Fusco, Rémi Soummer, Johan Mazoyer, Anand Sivaramakrishnan, Mamadou N'Diaye, Olivier Fauvarque, "Pair-based Analytical model for Segmented Telescopes Imaging from Space for sensitivity analysis," J. Astron. Telesc. Instrum. Syst. 4(3) 035002 (17 August 2018).

4 Error Budgeting

Error budgets are used to flow mission-level performance requirements down to sub-systems and components. Optical budgets typically dictate the allowable wavefront error contribution or optic motion that will maintain the top-level requirements. For the ULTRA study, error budget allocations are flowed down the optical sub-systems, then assessed against current technology capabilities in order to identify potential gaps and motivate additional technology development.

4.1 Traditional Approach

The traditional approach to error budgeting uses a branching tree structure to flow top-level requirements down to subsystems. Using a similar approach to the Webb optical budgets, [15] the ULTRA budget is organized by system (telescope vs. science instrument), then error phenomenon (thermal/dynamics), then optical subsystem (PM/SM/TM, etc.). For complex systems, it is reasonable to assume errors combine in quadrature, though the structure can be altered for additive combinations. The budgets also include compensation of certain wavefront errors through active sensing and control systems, which allows for larger "pre-correction" wavefront errors and corresponding optic motions that can be flowed to each sub-system.

The starting point for the ULTRA budget is a first order LUVOIR budget created on Ball Aerospace internal research and development (IRAD) funding during the LUVOIR cooperative agreement notice (CAN) study.[16,17] The ULTRA budget only considers the stability portion of the LUVOIR budget, which was updated with a matrix structure to explicitly track the spatial and temporal bins defined in Section 3.2. The top-level allocations have also been updated based on the coronagraph modeling work performed during this study. Since updates to the budget allocations have been ongoing due to the iterative process, some of the analysis sections use an interim version of the stability budget (see Section 4.4). This is to be expected as the allocations and analysis mature in parallel. A highlighted note at the end of each section compares the conclusions of the analysis to the updated stability budget using scaling from the top-level allocations. Given the maturity level of the budget, margin and uncertainty allocations are not included and the current allocations should not be considered final.

4.2 Top-Level Contrast Stability Budget

The key metric for coronagraph performance is imaging contrast, so the top-level stability budget is also allocated in terms of contrast, as in **Figure 7**. This study allocated a top-level raw contrast stability of 10^{-10} based on desired exoplanet yields from the LUVOIR STDT's design reference

---

[15] Paul A. Lightsey, Allison A. Barto, James Contreras. "Optical Performance for the James Webb Space Telescope," Proc. SPIE 5487 (2004).

[16] Cooperative Agreement Notice (CAN) FY2017 NNG16401001C 2020 Astrophysics Decadal Large Mission Concept Large Ultraviolet Optical Infrared (LUVOIR) Systems Studies at NASA Goddard Space Flight Center.

[17] Paul A. Lightsey, J. Scott Knight, Lee D. Feinberg, Matthew R. Bolcar, Stuart B. Shaklan, "First-order error budgeting for LUVOIR mission," Proc. SPIE 10398, UV/Optical/IR Space Telescopes and Instruments: Innovative Technologies and Concepts VIII, 103980C (5 September 2017);

mission.[18] Moving one level down, wavefront stability is not the only term that needs to be budgeted. The electric field entering the coronagraph contains amplitude and phase errors, both of which will affect the final contrast. Amplitude errors at non-pupil planes can couple into phase errors as the wavefront propagates, leading to contrast degradation. However, for most well-behaved optical systems, well controlled wavefront error will result in very low amplitude-to-phase errors. Thus, the detailed analysis in the ULTRA study is focused on wavefront stability, but a small fraction of contrast is allocated to amplitude stability, which can be further characterized using end-to-end simulations when the wavefront terms are better understood.
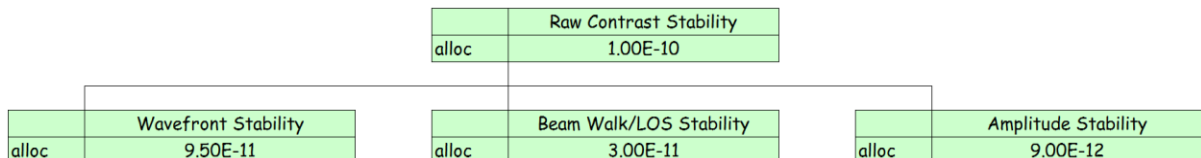
Figure 7: Top level contrast stability budget for ULTRA study. The desired raw contrast is flowed to three main sub-allocations – wavefront (phase) and amplitude stability and beam walk/LOS stability. Most of the allocation is given to wavefront stability, since it has the largest expected contribution.

Beam walk due to optic misalignments will also degrade contrast, though its allocation is also small since wavefront errors from beam shear on the ideal surface shape (accounted for in wavefront stability branch) are typically much larger than the errors from beam shear due to manufacturing residuals (accounted for in beam walk branch). Preliminary analysis of beam walk due to observatory LOS correction may contribute to wavefront error (WFE) at the picometer level and will likely consume most of the allocation (See Section 6).

4.3 Converting Contrast to WFE: End to End Coronagraph Simulations

To gain an understanding of the impact of wavefront error on contrast stability at various spatial and temporal scales, both analytical and computational coronagraph simulations were performed.

In the analytical approach, the goal is to derive the allowable wavefront error drift for a given observing scenario from first principles. The framework used is shown in **Figure 8**. This figure illustrates how the flux from the planet and star are attenuated as a function of the coronagraph design and the telescope stability (aka wavefront stability) to achieve a desired signal to noise ratio of greater than 1 at the desired contrast (setting a minimum threshold for the successful detection of an exoplanet).

---

[18]C. Stark, et. al., "Lower Limits on Aperture Size for an ExoEarth Detecting Coronagraphic Mission," Ap. J. 808 (2015).
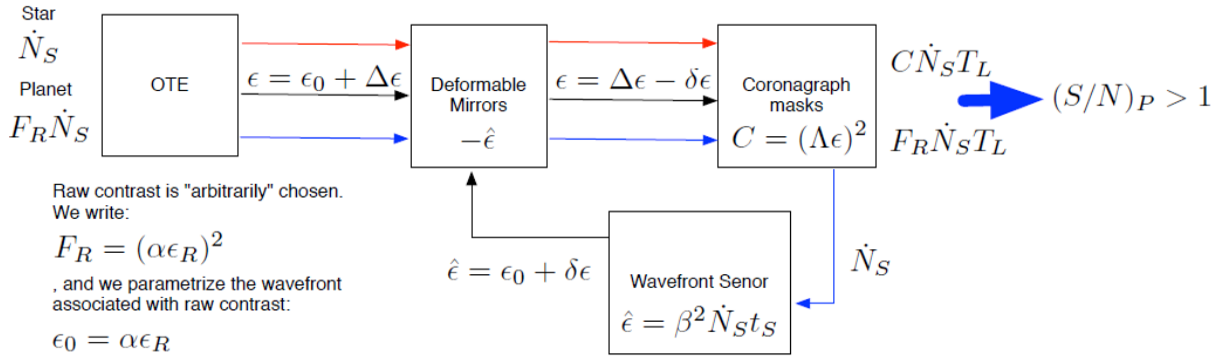
Figure 8: Analytical framework for coronagraph simulations developed during the ULTRA study to calculate the allowable wavefront drift during an exposure as a function of system parameters.

Variables include:

- $\dot{N}_s$ – the photon arrival rate from the host star in the current bandpass
- F_R – the flux ratio between the planet and the star
- ϵ – the WFE entering the coronagraph
- ϵ_0 – the static WFE (corrected with DM in WFSC)
- $\Delta\varepsilon$ – the wavefront drift in the Optical Telescope Assembly (OTA) during WFSC
- $(S/N)_P$ – the desired signal-to-noise ratio for the planet
- C – the starlight suppression (contrast) of the coronagraph instrument
- Λ – the coronagraph's sensitivity to a given mode (type of WFE)
- $\hat{\epsilon}$ – the figure applied to the deformable mirror to cancel the sensed WFE
- $\delta\epsilon$ – the error in the DM figure due to WFSC limitations (~shot noise)
- T_L – the long exposure time for the science observation
- t_s – the short exposure time for WFSC
- β – the efficiency of the wavefront sensor[19] ($\beta > 1$ for a non-ideal wavefront sensor operating in same band as the science observations)

This framework contains four key assumptions. First, that the nominal contrast floor is removed via simple point spread function (PSF) subtraction in image post-processing. More sophisticated PSF subtraction algorithms can potentially relax the drift requirements since they can be more robust to larger incident wavefront changes ($\Delta\varepsilon$). Second, that there is no crosstalk between the various spatial scales (i.e. energy from high scales will be distributed in different areas of the coronagraph dark hole and low/mid spatial scales are broken down into orthonormal eigenmodes for individual analysis). Third, that there is no wavefront drift in the optics of the coronagraph instrument. This is not true in practice, however, the bulk of the drifts are expected to occur at the OTA level, not in the instruments. As a result, we neglect this latter contribution for now. Fourth, that the deformable mirrors (DMs) can perfectly reproduce and correct the sensed wavefront modes with no lag, so the closed loop contrast stability is driven by the wavefront sensing error. The sensing error is modeled as photon noise based on the incident stellar flux:

---

[19] Guyon, O., "Limits of Adaptive Optics for High-Contrast Imaging", ApJ, Vol 629, Issue 1 (2005).

$$SNR_{WFS} = \frac{\epsilon}{\beta}\sqrt{\dot{N}_s t_s} \qquad\qquad [1]$$

The analysis was performed for two observing scenarios: "Set and Forget" for which no WFS&C is carried out during the science exposures and "Continuous WFS&C". **Figure 9** illustrates a notional time evolution of the incident wavefront under both scenarios.

Both scenarios have the same allowable contrast change, but different allowable wavefront drift per unit time, given by the following equations:

$$dWFE_{set} = \frac{\Delta\epsilon}{T_L} = \frac{1}{(S/N)_P{}^3}\frac{\dot{N}_s F_R{}^{3/2}}{2\alpha^3\Lambda} \qquad\qquad [2]$$

$$dWFE_{continuous} = \frac{\Delta\epsilon}{t_s} = \frac{1}{(S/N)_P{}^2}\frac{\dot{N}_s F_R{}^{3/2}}{2\beta^2\alpha\Lambda^3} \qquad\qquad [3]$$
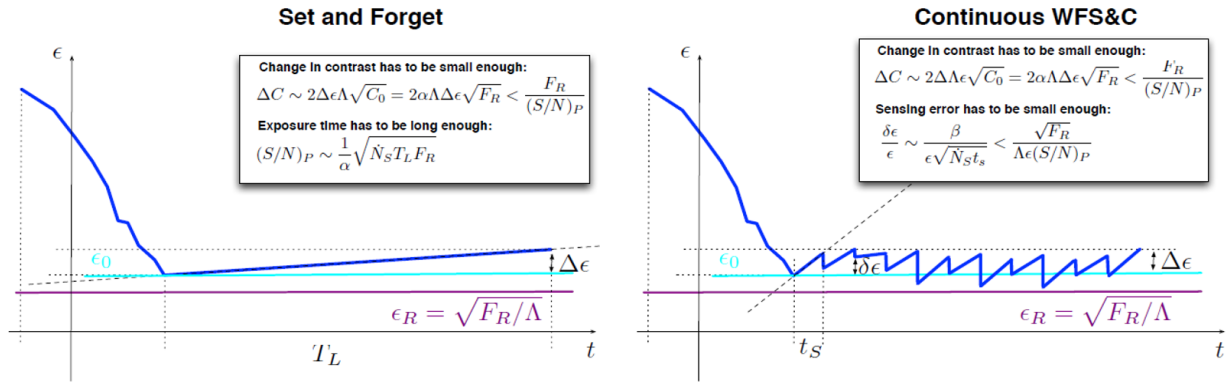
Figure 9: Time evolution of wavefront error for "Set and Forget" (left) and "Continuous WFSC" (right) observing scenarios. The total allowable drift is the same, but the drift rate of change is a function of the time constant for each scenario.

The "Set and Forget" wavefront error is driven by how far the desired contrast is from the flux ratio of the planet to star (α) while the "Continuous WFSC" wavefront error is driven by the wavefront sensor sensitivity (β). With these expressions derived, a computational simulation of an APLC is performed to calculate coronagraph-specific terms like Λ. The simulations were carried out for the LUVOIR B pupil geometry (8-m off axis), but we expect similar relative performance when optimized for LUVOIR A (15-m on axis), especially when analysis of spatial frequencies is normalized in cycles per aperture and scaled for difference in throughput (or other key parameters). LUVOIR A simulations can be performed in the next phase as the stability budget allocations, noise sources and trade studies mature alongside this analysis. The resulting wavefront drift allocations for the spatial and temporal bands described in Section 3.2 are shown in **Table 5**. These values assume all contrast degradation is allocated to the individual band – for a stability budget, they must be scaled down (see Section 4.4).

Table 5: Wavefront drift allocations for the LUVOIR B APLC as a function of spatial and temporal band. Assumptions: Raw contrast 10^10, planet to star ratio 10^11, mv = 5 host star, each band consumes full budget. Three values are shown for the mid spatial band, representing allowable segment piston, tip and tilt (PTT) respectively.

	Low Spatial Frequency (low)	Mid Spatial Frequency (mid)	High Spatial Frequency (hi)
Low Temporal Frequency 1 (LF1)	50 pm/10 hours (SF) 100 nm/10 min (CFWS)	[1,1.7,1.7] pm/10 hours (PTT – SF) [0.8,4,5] nm/10 min (PTT – CWFS)	0.04 pm/10 hours (SF) 0.6 pm/10 min (CWFS)
Low Temporal Frequency 2 (LF2)	100 nm/10 min	[0.8,4,5] nm/10 min (PTT)	0.6 pm/10 min (CWFS)
Low Temporal Frequency 3 (LF3)	100 nm/10 min	PSD < [24,35,38] pm RMS (PTT)	PSD < 10 pm RMS
Mid Temporal Frequency (MF)	PSD < 100 pm RMS	PSD < [24,35,38] pm RMS (PTT)	PSD < 10 pm RMS
High Temporal Frequency (HF)	PSD < 100 pm RMS	PSD < [24,35,38] pm RMS (PTT)	PSD < 10 pm RMS

These results provide a refinement to the "10 picometers per 10 minute" rule of thumb for 10^{-10} contrast stability. As expected, the continuous WFSC observing strategy provides significant relief on the required wavefront stability at low temporal frequencies (CWFS vs. SF for LF1 band in **Table 5**). For this coronagraph, the sensitivity Λ for the high spatial frequencies is roughly 10 times higher than the mid spatial frequencies, which results in a wavefront requirement that is ~1000x tighter in the high than the mid- ($dWFE_{continuous} \sim 1/\Lambda^3$). This is mostly because the high spatial frequencies are modeled as pure sine wave errors and mid-spatial frequencies are modeled with eigenmodes of segment piston, tip and tilt (PTT), which spread the error over a spectrum of sine waves even if adjacent segments have alternating errors (ex. "up-down-up-down", etc. for piston); this spreading out relaxes the requirement on segment motions compared to a pure tone with the same amplitude and fundamental frequency. More work is needed to refine the very tight "hi" allocations, especially at low temporal frequencies, since they may be too pessimistic as a result of using pure sine waves which are not likely to appear in a physical telescope. A visual representation of the allowable drift trends from the analytical calculations are shown in **Figure 10** and **Figure 11**.

Moreover, analysis of segment-to-segment eigenmodes reveals additional relaxation for certain segments, as shown in the allowable piston error for outer edge segments in **Figure 11**. However, these segment-level eigenmodes of the coronagraph (like the pure sine wave errors used to assess high spatial frequencies) may not be physically realizable in a real telescope – additional analysis of "optomechanical modes" is needed to form a complete assessment and may provide some refinement to the values in **Table 5**. However, those values are still quite useful in gaining a high-level understanding of the relative requirements in the various spatial and temporal scales.
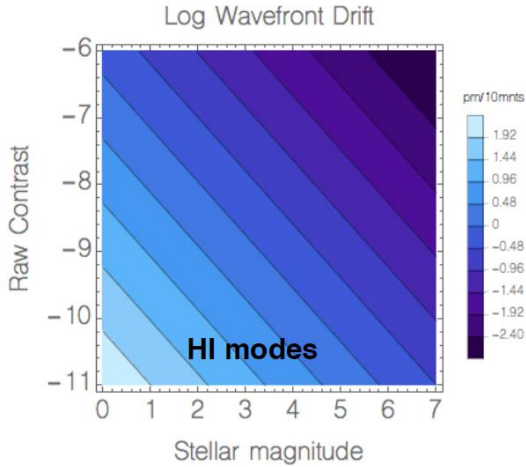
Figure 10: Allowable wavefront drift for high spatial frequency errors (pure sine waves) as a function of desired contrast and stellar magnitude.
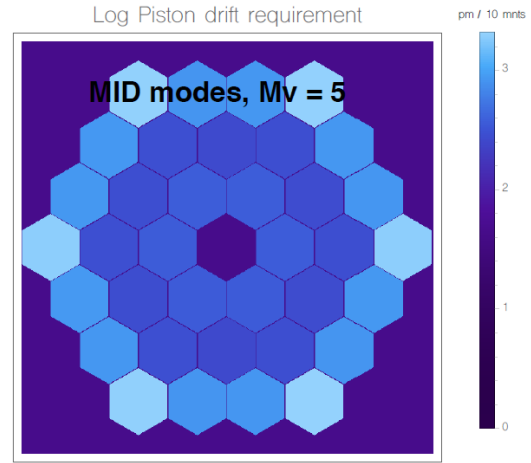
Figure 11: Allowable wavefront drift for mid (segment-level) spatial frequency errors for 10^{-10} raw contrast with a magnitude 5 star. Allowable piston varies from segment to segment.

Monte Carlo end-to-end diffraction simulations were also run to validate the assumptions underlying the analytic results. Histograms of resulting contrast for the "Set and Forget" scenario with mid (segment-level) spatial frequency errors are shown in **Figure 12**. The results confirm that the allowable wavefront errors calculated with the analytical model do result in ~10^{-10} raw contrast. Similar high-fidelity diffraction simulations have not yet been run for the "Continuous WFSC" scenario, but the results of the analytical model are in line with detailed calculations presented in the literature, one set of which is shown in **Figure 13**.[6,20,21]
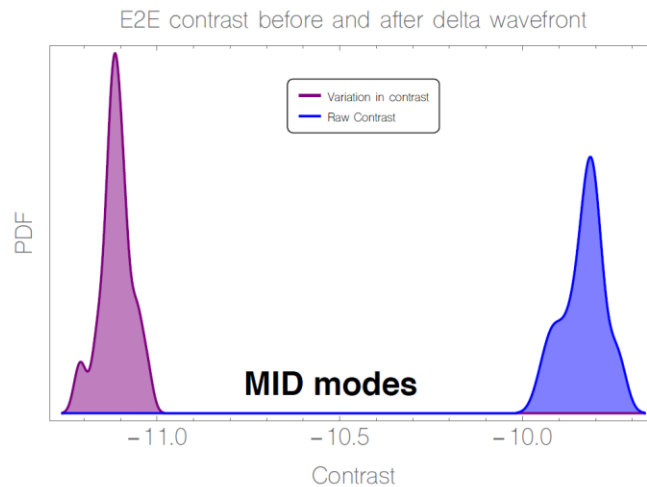
Figure 12: Results of Monte Carlo simulation for mid spatial frequency errors for the "Set and Forget" scenario result in the expected 10^{-10} contrast.

[20] Douglas E. S., Males J. R., Clark J. et al., "Laser Guide Star for Large Segmented-aperture Space Telescopes I Implications for Terrestrial Exoplanet Detection and Observatory Stability", AJ, Vol 157, Issue 1 (2005).

[21] Moore D., Redding D. "Picometer differential wavefront metrology by nonlinear Zernike wavefront sensing for LUVOIR", Proc. SPIE 10698 (2018).

Segment Errors		Global Errors	
Mode	pm	Mode	pm
Segment Piston	7	Global Bend about Y	209
Segment Tilt	13	Global Bend about X	224
Segment Power	23	Global Spherical	624
Segment Astigmatism	32	Global Hexafoil	778
Segment Trefoil	87	Global Zernike Coma	1049
Segment Hexafoil	314	Global Trefoil	2322
		Global Seidel Coma	2872
		Global Power	5798

Figure 13: Allowable RMS wavefront stability error for various aberrations in the OTA to maintain 10^{-10} contrast.[6] The tightest allocations are for segment piston, tip and tilt.

4.4 Top-Level Wavefront Stability Budget

To create the top-level wavefront stability budget, the allocations in **Table 5** were scaled down such that the root sum square of all bins was equal to the allocation of 9.5e-11 from **Figure 7**. The resulting numbers were further scaled by ~0.85 to allow for wavefront error in the coronagraph instrument. A system-level decision was made to reduce the bins unevenly to ease the tightest allocations. These allocations can be rebalanced as needed during future iterations of the full analysis cycle. The resulting wavefront stability budget in picometers RMS for the OTA is shown in **Table 6**.

Table 6: **Wavefront stability budget for the OTA in picometers RMS, broken out by spatial and temporal frequency. These allocations are post-active sensing and control. Excluding the "hi" allocations, which need additional evaluation, the tightest requirements are on segment level, quasi static and faster errors (LF3/MF/HF for mid).**

pm	OTE Stability			
RMS	tot	lo	mid	hi
Alloc	158.0	153.2	38.1	6.1
LF1	91.2	87.3	26.2	0.4
LF2	91.2	87.3	26.2	0.4
LF3	87.5	87.3	5.2	3.5
MF	18.6	17.5	5.2	3.5
HF	18.6	17.5	5.2	3.5

There are several takeways from **Table 6** of note:

- The total wavefront stability allocation is 158 pm RMS, not 10 pm RMS (of "10 picometers per 10 minutes"); it is known that the coronagraph is more tolerant to certain spatial and temporal modes
- For lo/mid spatial frequency errors, requirements for LF temporal bands are looser than the MF/HF bands thanks to HOWFS with the DMs.
- These numbers only include WFSC inside the coronagraph (HOWFS/LOWFS). Allowable errors will be larger if there are active systems to correct in the rest of the OTA.
  - Ex. Mid-MF corresponds to active sensing and control at the PMSAs in the 1-10 Hz regime; The current allocation is 5 pm RMS, which means segments can move more than that if segment motions are within the sensing capture range and the sensing/control residuals are less than 5 pm RMS at that bandwidth.

- The tightest requirements are at high spatial scales and low temporal scales; however, the high spatial scale requirements were derived using pure sine waves errors which show up as concentrated peaks in the dark hole.
  - Pure sine waves are pessimistic since they aren't physically realizable in a real telescope. Real modes will have some decorrelation, which lowers the peak energy and increases the allocation.

As mentioned in Section 4.1, some analysis was performed using an interim version of the stability budget, shown in **Table 7**. The ratio of the updated allocations to these interim allocations is shown in **Table 8**, which will be used for scaling results of the detailed analysis, if needed. The largest difference is in the LF1 band – it still has the loosest requirement for the lo/mid spatial scales, but is tighter than previously budgeted. All other allocations are within an order of magnitude, which is likely comparable to the uncertainty in the stability budget terms given the early level of maturity.

Table 7: Interim stability budget used for some of the detailed analysis.

pm	OTE Stability			
RMS	tot	lo	mid	hi
Alloc	155.7	891.4	650.1	344.0
LF1	1155.3	891.1	649.9	343.9
LF2	15.1	11.0	9.2	4.6
LF3	15.1	11.0	9.2	4.6
MF	13.0	9.2	9.2	0.4
HF	10.3	9.2	4.6	0.4

Table 8: Stability budget ratios. Green shading = looser, yellow shading = comparable, orange shading = tighter

RATIO	OTE Stability			
	tot	lo	mid	hi
Alloc				
LF1		0.10	0.04	0.001
LF2		7.94	2.85	0.09
LF3		7.94	0.57	0.76
MF		1.90	0.57	8.75
HF		1.90	1.13	8.75

4.5 Sub-System Wavefront Stability Budget Allocations

The top-level OTA allocations in **Table 6** can be broken out by disturbance phenomenon (dimensional or dynamic) then by optical subsystem (PM/SM/TM/FSM/AOS). The resulting subsystem structure is shown in **Figure 14**. Most of the optical subsystems have two terms "Align" and "Figure" – Align refers to the 6 DOF positioning in space (low spatial frequencies) and Figure refers to change at mid- and high spatial frequencies.

These values are "post-active-control" allocations and only the RSS of the frequency allocations for each band are shown since the budget allocations at these lower levels are still in the active trade space. At this early stage in the systems engineering process, it should be remembered that the stability budget is a living document, rather than a rigid set of flight-like requirements, and given the number of open questions, we are aiming for order of magnitude levels of accuracy to assess technology gaps. As the design and analysis methods mature, these allocations can be assessed with greater precision.

OTE Stability

pm rms	tot	lo	mid	hi
Alloc	158.0	153.2	38.1	6.1

OTE Dynamic Stability

pm rms	tot	lo	mid	hi
Alloc	99.8	97.0	22.8	5.5

OTE Dimensional Stability

pm rms	tot	lo	mid	hi
Alloc	122.5	118.6	30.6	2.5

Dynamic Stability subsystems:

	tot	lo	mid	hi
PM Figure	41.6	36.4	19.7	4.8
PM Global Align	72.8	72.8	0.0	0.0
SM Figure	14.6	12.1	7.9	1.9
SM Align	24.3	24.3	0.0	0.0
TM Figure	13.6	12.1	5.9	1.4
TM Align	24.3	24.3	0.0	0.0
FSM Figure	13.6	12.1	5.9	1.4
FSM Align (despace)	24.3	24.3	0.0	0.0
AOS Align	24.3	24.3	0.0	0.0

Dimensional Stability subsystems:

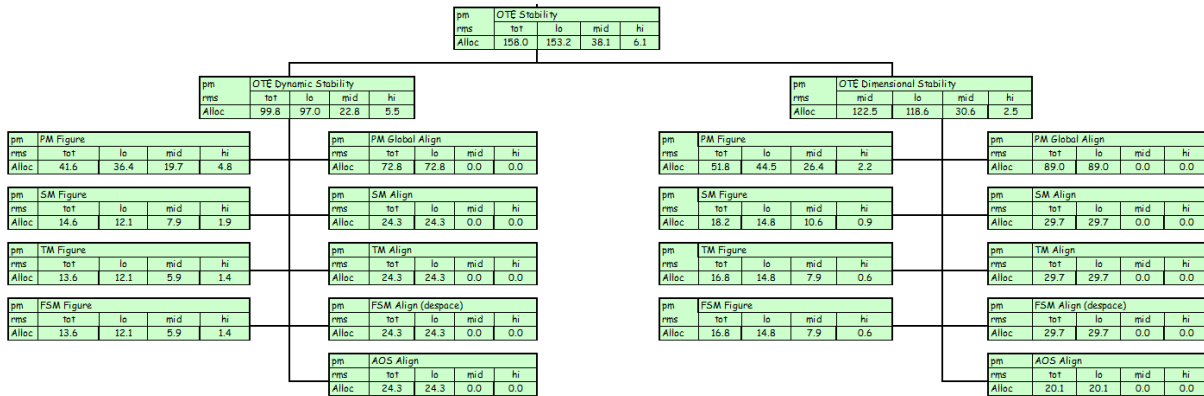|	tot	lo	mid	hi
PM Figure	51.8	44.5	26.4	2.2
PM Global Align	89.0	89.0	0.0	0.0
SM Figure	18.2	14.8	10.6	0.9
SM Align	29.7	29.7	0.0	0.0
TM Figure	16.8	14.8	7.9	0.6
TM Align	29.7	29.7	0.0	0.0
FSM Figure	16.8	14.8	7.9	0.6
FSM Align (despace)	29.7	29.7	0.0	0.0
AOS Align	20.1	20.1	0.0	0.0

Figure 14: The top-level wavefront stability budget is allocation to the OTA subsystems by disturbance phenomena. Only the top level spatial frequency allocations are shown as the individual temporal band allocations are still in an active trade space. Each optical sub-system has an "Align" (6 DOF position/low order spatial frequency) and "Figure" (mid/high order spatial frequency) allocation.

4.6   PSD based approach

While the traditional error budget approach works well for many optical systems, just breaking the spatial content into bins may still prove overly conservative for a coronagraph instrument. A different approach is Power Spectral Density (PSD) based budget. The point spread function (PSF) of a wavefront and the PSD of a surface are both related to each other by a squared Fourier transform relationship. If these quantities are calculated in two dimensions, the PSD of a surface can be used to predict where energy is likely to end up in the coronagraph dark hole. This approach allows us to decouple the analysis from the complexities of the coronagraph for a first order sensitivity assessment, then perform an end-to-end simulation on perturbations that match the stability budget allocations. An example of the pure sine wave error used for the analysis in Section 4.3 is shown in **Figure 15.**
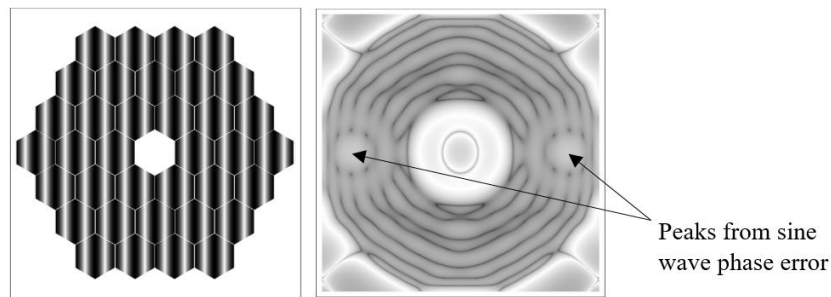
Peaks from sine wave phase error

Figure 15: Sine wave error in the pupil (left) corresponds to distinct peaks in the coronagraph dark hole (right). The PSD of a sine wave will also produce two lobes. Note: this analysis was performed for the LUVOIR B pupil.

The sine wave phase error creates two distinct peaks in the coronagraph dark hole. The allowable magnitude of the sine wave error is driven by the magnitude of those peaks, which cannot raise the background level above the required 10^{-10} detection contrast at any point in the image plane. However, if the sine wave error had random phase shifts on each segment or was otherwise decorrelated, the peaks would blur and decrease the magnitude in the image plane. This would

allow the phase errors to increase to match the original magnitude, providing relief for perturbations that produce that signature. This same analytical approach can also be applied to more typical wavefront error forms (like segment piston).

The peak of the sine wave PSD can be used to set a limit on the maximum energy in the dark hole, which will vary in the different temporal regimes based on the coronagraph sensitivity. Then additional terms can be budgeted using their PSDs and ensuring the combined PSD does not exceed the limit set by the sine wave. The important result is that <u>errors that put energy into different parts of the dark hole do not need to share allocations</u> – they can each have the full amount, providing maximum relief to the system. Examples of PSDs for various error types are shown in **Figure 16**, **Figure 17**, and **Figure 18**. An example of a combined PSD that would be used for stability budgeting is shown in **Figure 19.** The PSD includes the effects of random segment piston, random segment tilt, and a bulk temperature change of the mirror substrates, which manifests primarily as segment-level trefoil. Each PSD can be scaled such that the sum is below the normalization limit (allowable wavefront error ~ sqrt(PSD ratio)). If the PSDs do not spatially overlap, each perturbation can consume the full allocation. This effect is lost when the spatial bands are too coarse, such as the "low", "mid", and "high" bands described in the previous sections.
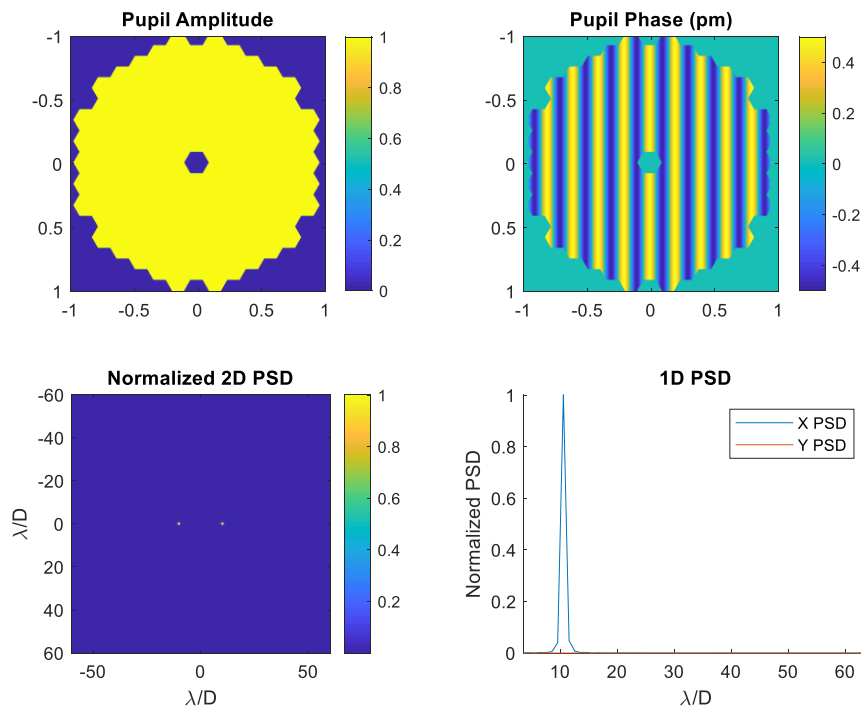
Figure 16: A sine wave with 1 pm amplitude in wavefront and 10 cycles/diameter causes a contrast degradation of 10^{-10}. Calculating the PSD of the error and the corresponding peak amplitude provides a normalization factor for the allowable energy density in the dark hole. Current normalization values are a draft allocation.

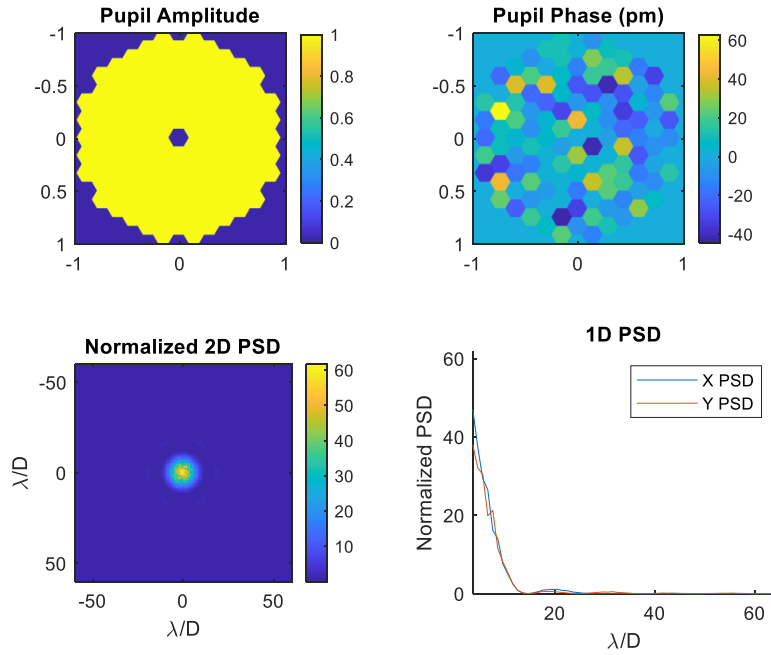**Figure 17: 10 pm RMS of segment piston produces a peak near the the IWA. Curves are the average of 100 Monte Carlo Trials. (Draft normaliation factor)**

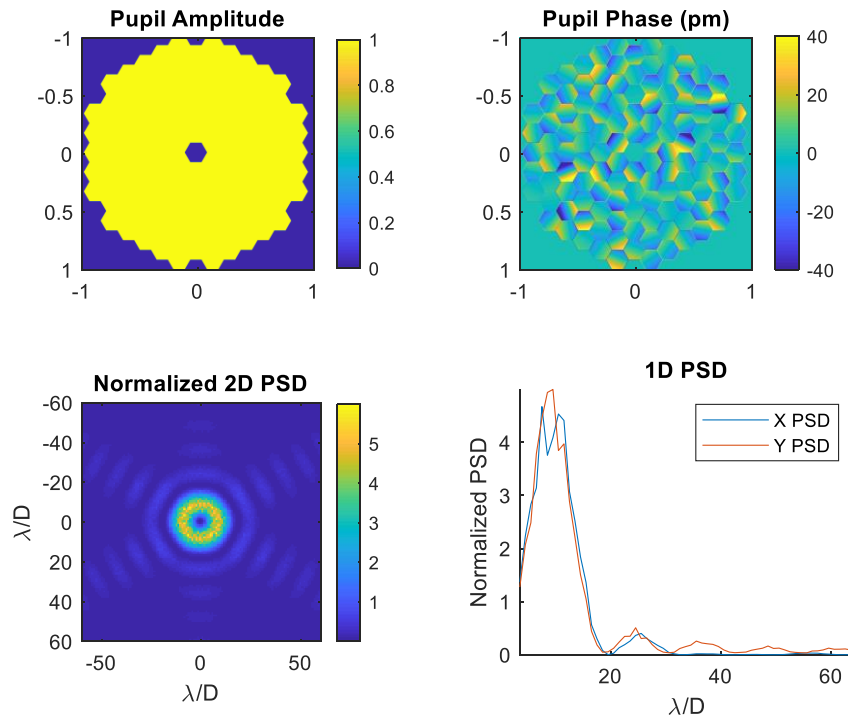**Figure 18: 10 pm RMS of segment tilt produces a peak near 5 cycles/diameter. Curves are the average of 100 Monte Carlo Trials. (Draft normaliation factor)**

It is important to note that while there is overlap between the PSD for random segment piston and segment tilt, the peaks are shifted slightly, which means there is some relief in budgeting those terms. For the example shown in **Figure 19**, each term gets ~80% of the allocation, whereas in a RSS WFE approach, each term would get 58% of the allocation (1/sqrt(3)). In addition, terms that create high spatial frequency errors, like trefoil from mounting effects, will not have significant overlap with piston/tip/tilt and can consume much of the allocation. Based on these results, parts of the system architecture (such as mirror mounting) may be adjusted to put energy into regions of the dark hole that do not have other sources, providing additional relief on the allowable perturbations or performance of the active control systems.
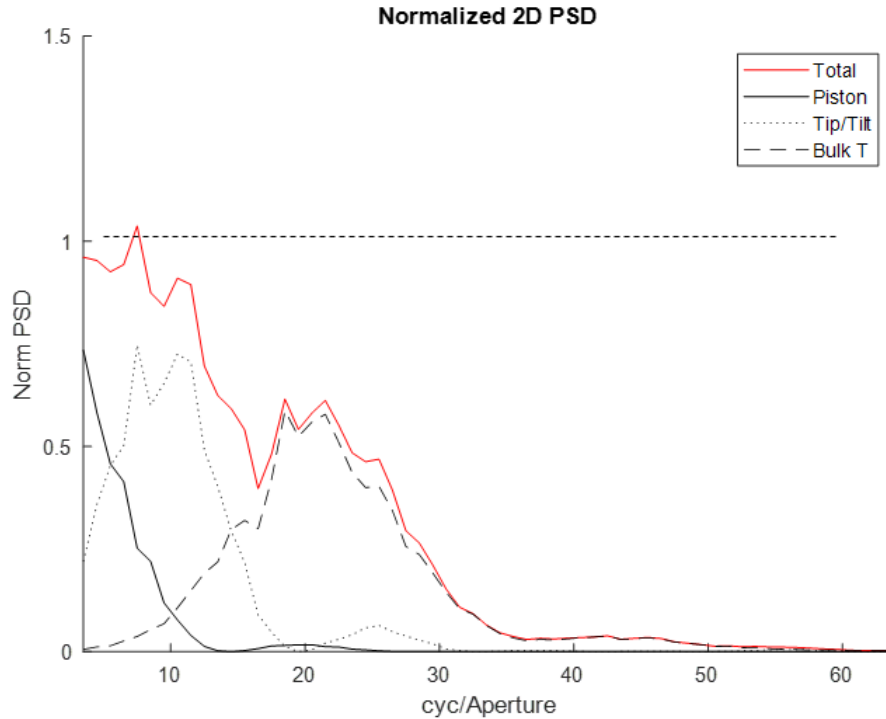
Figure 19: Example of a PSD-based stability budget for PSMA random piston, tilt and bulk temperature change (trefoil at the segment level). While there is overlap in the PSD, the peaks are shifted slightly, which means there is some relief in budgeting those terms. In this example, each term gets ~80% of the allocation, whereas in a RSS WFE approach, each term would get 58% of the allocation (1/sqrt(3)).

The path forward for maturation of the stability budget will use this PSD based approach – various errors can be modeled for their "PSD sensitivities" and the normalization factor for each temporal bin can weighted by the relative allocations in **Table 6**. While the PSD based approach does not include the impact of the coronagraph beyond the normalization factor, it is an appropriate starting point for determining the rough allowance for perturbations and control system performance. We still rely on end-to-end time domain simulations to provide the fidelity to understand interactions of the errors with each other and with the coronagraph.

The development of the PSD approach occurred late in the study. The work presented in this report uses the binned allocations from **Table 6,** which provides a solid starting point and can be refined by the PSD-based approach in future work.

5   *Expected Disturbances*

Now that we have a method to calculate sensitivities, the expected disturbances must be quantified to predict the impact on the system, which can then be compared to the budget allocations to identify gaps. Decades of systems engineering for space telescopes has revealed which types of perturbations will impact an optical system at the nanometer level. However, moving to the realm of picometers means historically ignored sources may no longer be negligible. The list of sources considered in this study that will harm wavefront stability is listed in **Table 9**. For the "new" sources, a first order calculation is performed to determine whether the effect is still negligible (< 0.01 pm), needs to be budgeted (~ 1 pm) or is potentially impactful on technology needs (> 10 pm).

Table 9: List of noise sources considered in this study. Sources are classified by environmentally/system induced and by classical (nanometer regime) and new (potentially picometer regime).

	Environmentally Induced	**System Induced**
Classical Sources	• Thermal distortion from solar flux (function of telescope orientation/slew)	• Thermal distortion from on-board sources • Moisture Desorption • S/C Dynamics: CMGs, propellant slosh • Payload Dynamics: hinges, latches, mechanisms
New Sources	• Gravitational Forces (Sun/Earth/Moon) • Charging – Coulomb Forces (electrostatics) and Lorentz Forces (electrodynamics) • Radiation Induced Compaction • Micrometeoroid impacts (dynamics)	• Gravitational Forces (Self-interaction) • Inertial Forces from station keeping

5.1   Classical Noise Sources

Analysis for classical noise sources in **Table 9** is addressed in the following sections on low disturbance architectures (Section 8), stable structures (Section 9),and stable mirrors (Section 10). These include thermal (low frequency) and dynamic (mid-to-high frequency) sources and their impact on wavefront stability. Given the demanding stability requirements for LUVOIR, these common sources may require additional mitigation strategies, which are discussed in the relevant sections.

5.2   New Noise Sources

A bounding, first order analysis is performed for typically neglected noise sources to estimate their impact on the system stability and evaluate whether new technologies will be needed.

5.2.1   Gravitational Sources

Objects in proximity to the observatory will exert a gravitational pull that could potentially affect the positions of the optics and thus the wavefront. A first order calculation of the force exerted by

the earth, sun, and moon on LUVOIR at Lagrange Point 2 (L2) showed the expected deformations were well below 1 pm due to the very large separation distances. A similar analysis for Near Earth Objects (NEOs) also proved the forces are negligible, except for exceptionally large NEOs/close approaches which are highly unlikely and could be considered transient events that require a break in observation until stability is restored.

The impact of moving masses on board the observatory was also studied – though the masses are much smaller, they are also much closer to the optics. A "moving moment" was defined as the product of the component's mass and expected displacement, which is assumed to be constant for a given source (i.e. propellant slosh). In **Figure 20,** the curves represent the change moment required to move an optic by 1 picometer at various separation distances. The multiple curves represent the various system stiffnesses (forces) which couple the moving moments to the optics. As the separation distance increases for a given change moment, a larger force is required to move the optics by 1 pm. Thus, if the change moment for the LUVOIR component is below the curves at the expected separation distance, a larger-than-expected stiffness/force is required to create 1 pm motion.
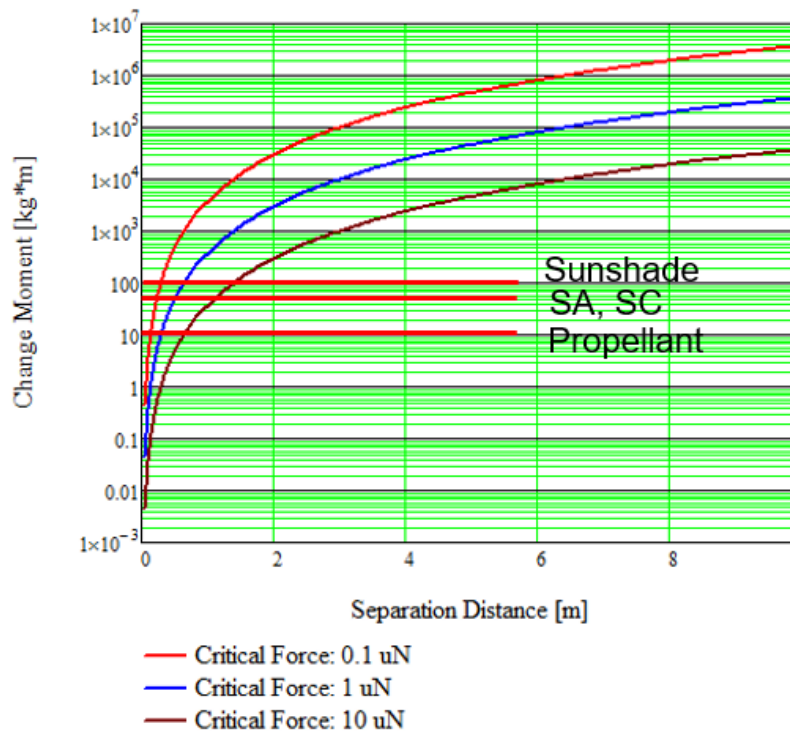
Figure 20: Allowable moving moments vs. separation distance, critical force exerted (curves). The expected moments from moving masses for LUVOIR are also shown (horizontal lines). If the moment for the LUVOIR component is below the curves at the expected separation distance, the resulting optic motion due to changing gravitational forces will be < 1 pm.

The likely LUVOIR moving moments are:

- Sunshade fundamental mode (1000 kg, 10 cm=100 kg·m)
- Propellant slosh, Mitigated (1000 kg, 1 cm=10 kg·m)
- Solar Array (700 kg, 10 cm=70 kg·m)
- Entire SC (7000 kg, 1 cm= 70 kg·m)

Since most of these elements are > 2 meters away from the PMSAs, the moving mass and expected coupling stiffness is well below the threshold to cause 1 pm motion. Thus, changing gravitational forces within the observatory do not need to be budgeted.

While we have yet to perform analysis of inertial forces due to observatory station keeping, we expect the disturbance will be similar motions of large on-board masses resulting in comparable forces. This effect can be modeled in future efforts.

5.2.2 Charging

Charged particles, like protons and electrons, lose energy as they propagate through matter and eventually become embedded. If the matter is a perfect insulator, this charge distribution will be "frozen" on the surface. If it is a conductor, the charges can be drained off, leaving the object electrically neutral. Most materials are somewhere in between, and since the charged particles can have a range of energies, they will propagate different distances in the material before becoming embedded. [22] For example, the propagation distance of electrons in aluminum is larger than protons (**Figure 21**). This leads to a spatial separation of charge, which results in a small electrostatic force.
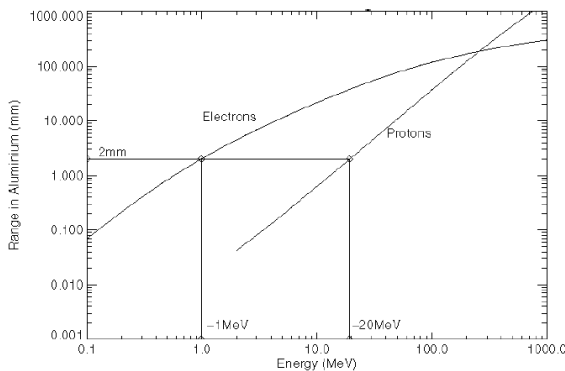
Figure 21: Propagation distance of charged particles in Aluminum.[22]
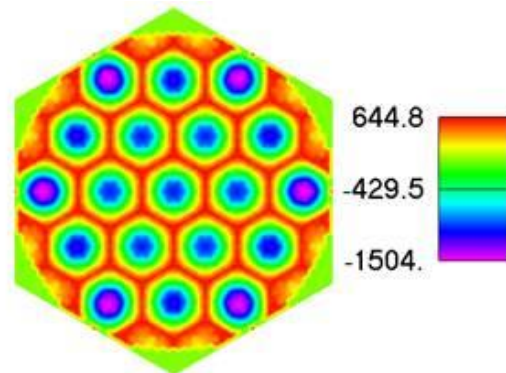
Figure 22: Segment-level surface deformation due to electrostatic forces from 1 year of charge accumulation (perfect conductor assumed). Resulting stress is ~ 1 Pa and deformation is 568 pm RMS.

For LUVOIR, charged particles from the space environment will collide with the PMSAs, which are insulators since they are modeled as low CTE glass. While charges colliding with the front face should be evenly distributed over the surface, charges colliding with the rear surface will have their spatial distribution impacted by the lightweighting ribs. The expected surface deformation from one year of accumulation of charged particles (assuming a perfect insulator) is shown in **Figure 22**. Assuming a steady rate of charge accumulation, 568 pm RMS of surface deformation over 1 year corresponds to 1.5 pm RMS per day and 0.01 pm RMS over a 10-minute integration period. This effect is negligible over a single coronagraph observation but will impact the static wavefront error. Regardless, the high spatial frequency content of the error (~60 cycles/D) will

---

[22] E.J. Daly, A. Hilgers, G. Drolshagen, H.D.R. Evans, "Space Environment Analysis: Experience and Trends," ESA 1996 Symposium on Environment Modeling for Space-based Applications, ESA SP-392, (1996).

likely put energy outside the coronagraph dark hole (beyond the outer working angle), where much higher deformations are allowed.

Embedded charges not only produce electrostatic fields, they also interact with changing magnetic fields to create dynamic Lorentz forces. To estimate this effect, the change in force ($F = qvB$) was calculated as a function of mission lifetime – the force will increase over time as more charge accumulates, producing a stronger interacting with the magnetic field. For a magnetic field of magnitude 10 nT, a relative velocity of 20 km/s and a charge accumulation of ~10^{-11} C/s/PSMA, the resulting force as a function of mission lifetime is plotted in **Figure 23**. The buildup of charge results in a force that is not negligible, but the calculation includes several worst-case assumptions including a rapidly changing B field and a perfect insulator. While further refinement is needed to prove this effect is small, this is a slow effect that may impact static wavefront, rather than wavefront stability during coronagraph observations, if it is not addressed by design.
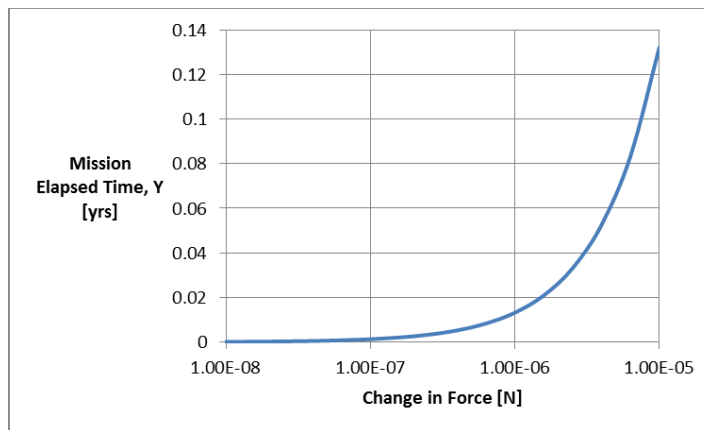
Figure 23: The expected force from interaction between embedded charges and external magnetic fields. The resulting force is not negligible, possibly due to worst-case assumptions. This very slow effect will have a greater impact on static wavefront (the ability to dig the dark hole) than on stability during coronagraph observations (the ability to maintain the dark hole for 48 hours).

5.2.3   Micrometeoroid Impacts

Previous missions have analyzed the impact of micrometroids for permanent surface deformation or loss of reflecting area. While these impacts will also be relevant for LUVOIR, they do not play a significant role in the stability problem over the course of a coronagraph observation. However, micrometeoroid collisions that cause a dynamic response in the optics may be of concern. During a collision, the kinetic energy of the particle is transferred to the telescope, typically creating plasma, fracturing the structure or mirror, creating heat and transferring an impulse to the system. As a bounding case, we will consider that all the particle's kinetic energy is transferred to the telescope and this energy then disturbs the telescope. For this initial analysis it is assumed that the sunshield is planar (exposed telescope) and that it is isolated from the telescope, so none of the impacts on it are transferred to the telescope.

The cumulative flux of micrometeoroids used in this analysis is from the Grun model.[23] A plot of this model is shown in **Figure 24**. Flux, $\phi(m)$, is the number of collisions at the particle mass (m) or higher, per square meter per year.
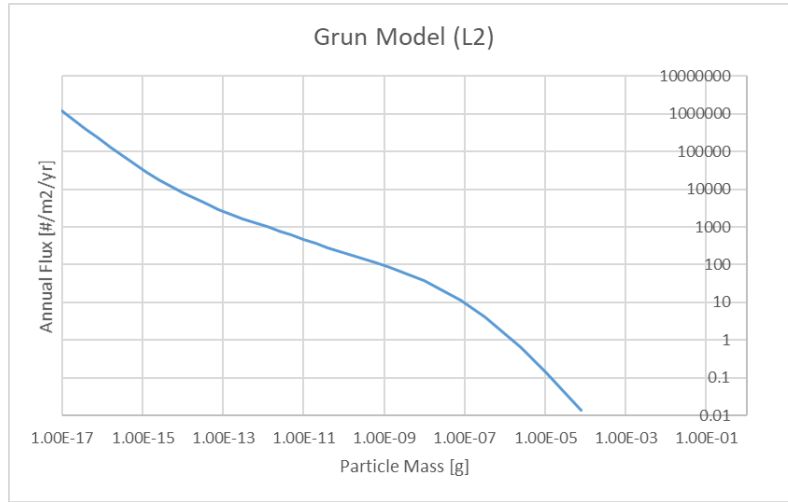
Figure 24: Grun Model of expected micrometeriod flux at L2.[23] Flux decreases as particle size increases.

The number of collisions of micro-meteors and the telescope is a function of area, considering impacts on both sides of the mirror the effective collisional area, A is

$$A = \frac{\pi D_T^2}{2} \qquad [4]$$

where D_T is the diameter of the telescope. In this case, the PMSAs will react independently if a micrometeoroid strikes one of them, so the PMSA diameter is used instead of the full telescope diameter. The number of collisions per year (annual rate) as function of particle mass is given by

$$C = \varphi(m)\frac{\pi D_T^2}{2}. \qquad [5]$$

The period P(m) between collisions is then simply the reciprocal of Equation 5. Expressed in units of minutes rather than years, this becomes:

$$P(m) = \frac{1}{C} = \frac{10^6}{\varphi(m)\pi D_T^2} \qquad [6]$$

If a typical coronagraph exposure is of order 10 minutes, the interval between disturbances causing loss of data will need to be much longer, so choose a factor of 20 (5% frame loss). Equation 6 can be solved for flux giving:

---

[23] Grün, E., H. A. Zook, H. Fechtig, and R. H. Giese, "Collisional Balance of the Meteoritic Complex," *Icarus, 62*, 244-272 (1985).

$$\varphi(m) = \frac{10^6}{200\pi D_T^2} = \frac{1591}{D_T^2} \qquad [7]$$

For a 1.5-m diameter PMSA, the flux is ~ 707. Using **Figure 24**, the particle mass that corresponds to a flux of 707 is ~1e-11 grams. The distribution of micrometeoroid velocity is bimodal, with approximately 2/3 of the flux having a velocity of 22 km/sec and the remainder a velocity of approximately 55 km/sec. The kinetic energy of the average particle is calculated from these velocities and the mass is 5.4 µJ. The mirrors can be modeled as masses on stiff springs (the actuators). If the kinetic energy of the particle is transferred to the mirror, the mirror will be displaced by an amount proportional to the particle energy and the spring constant of the actuators. The results for various actuator stiffnesses is shown in **Table 10**.

Table 10: Displacement of mirror for expected particle kinetic energy (divided among the 6 actuators) as a function of actuator stiffness. The displacement is much larger than 1 picometer, but very conservative assumptions are used (i.e. perfectly elastic, head-on collision)

Particle KE per actuator (J)	Actuator Stiffness (N/um)	Actuator Displacement (pm)
9.075E-07	10	4.26E+05
9.075E-07	100	1.35E+05
9.075E-07	1000	4.26E+04

The displacements listed in **Table 10** are much larger than 1 picometer (50-500 nm) even for very stiff actuators. However, the first order analysis used is very conservative – it assumes a head-on, perfectly elastic collision with no compensation of the mirror motion from the active sensing and control system. More work is needed to refine the transferred energy, the temporal nature of the collisions and the potential mitigation from the active control systems. However, LISA pathfinder, another picometer-sensitive mission, is able to detect and localize micrometeoroid strikes that move the spacecraft by 50 nm, [24] which is on the order of displacement values in **Table 10.** So it is likely this effect will need to be budgeted and controlled for LUVOIR. The number of impacts could be mitigated using shielding around the telescope itself, though the architectural impacts could be significant.

5.2.4   Other Effects

A number of other potential sources were considered, with the results listed in **Table 11**.

---

[24] J.I. Thorpe et. al., "LISA Pathfinder as a Micrometeoroid Instrument," J. Phys.: Conf. Ser. **840** (2017).

Table 11: Expected impact of other "new" noise sources.

Effect	Assessment	Rationale
Momentum Imbalance	No issue expected	Radiation pressure difference on sunshield from change in solar constant is ~ 2e-7 μN, much less than radiation pressure average of 9000 μN. Any statistically induced imbalance is swamped by other effects.
Sunshade attenuation of transients	No issue expected	Analysis of blanket
Propellant slosh	No issue expected	SOTA can deliver small moving moments, but there is a mass penalty. Work is ongoing to develop rough parameters for LUVOIR class tanks.

5.2.5 Summary

The majority of the "new" noise sources listed can be retired. They have been shown by conservative, limiting analysis to be far below thresholds of concern. However, the effects that cannot be shown small are related to micrometeoroid strikes and bulk charging of the mirror substrates (though the charging effects are negligible over a 48-hour period for coronagraph observations). The micrometeriod strikes use a set of very conservative assumptions that must be re-visited to gain an accurate understanding of the energy transfer. Mitigation through shielding could also be implemented. The electrostatic induced figure change implies a trade between conducting substrates and insulator with figure control. The Lorentz force analysis will require better estimates of the field strengths and charge accumulation before a determination can be made. As the environment at L2 is better understood, this analysis may need to be revisited or new sources added to the budget.

6   Beam Walk/Line of Sight

"Beam walk" or a shift in the location of the beam footprint on each optic due to misalignment or a change in the line of sight (LOS), will have three impacts on the system wavefront:

1. Shear on the optical surface will expose the beam to a different part of the ideal surface shape, which will add a slightly different wavefront error.
2. Shear on the optical surface will expose the beam to spatially varying manufacturing residuals, which will add a slightly different wavefront error.
3. Shear on a deformable mirror will cause the wavefront correction produced by the DM to no longer line up properly.

The first impact is the typical "optical sensitivity" that is used for the analysis in Section 10 (Stable Mirrors). The analysis here will focus on the 2nd effect, as the 3rd is more suited to future end-to-end simulations. The amount of additional wavefront error from manufacturing residuals depends on the spatial frequency content of the surfaces and the amount of beam shear. Thus, PSD analysis can be used to quantify the expected change in phase error from beam walk. The PSD of an optical surface is proportional to the magnitude squared of the Fourier transform of phase profile:

$$G(k_x, k_y) = \left|\emptyset(k_x, k_y)\right|^2 \tag{8}$$

The PSD of the sheared beam on optical surface is proportional to the spatial frequency of the surface error k_x and shear distance δx (only valid if k*δx << 1)[25]

$$\delta G(k_x, k_y) = (2\pi k_x \delta x)^2 G(k_x, k_y) \tag{9}$$

The PSD of an optical surface can be modeled analytically via the following equation:

$$G(k) = \frac{A}{1+\left(\frac{k}{k_0}\right)^N} \tag{10}$$

The PSDs of the LUVOIR PM, SM, TM and FSM are modeled using parameters (A, k0, N) from the Terrestrial Planet Finder (TPF) study shown in **Figure 25**, which takes the size and shape of the optics into account when estimating typical manufacturing performance.[26]

Table 2: PSD specifications for optics modeled in the CEB.

	Primary	Secondary	Fold	Super Fold	OAP	Super OAP	Anamorphic 1	Anamorphic 2	DM
D (m)	8.02	0.83	0.1	0.1	0.1	0.1	0.23	0.10	0.10
k0 (cy/m)	4	4	10	10	10	10	10	10	320
A (m^4)	9.60E-19	9.60E-19	1.25E-20	7.58E-21	1.25E-20	1.09E-20	5E-20	7.5E-20	8.52E-22
n	3	3	3	3	3	3	3	3	3
RMS WF	8.51E-09	9.55E-09	2.15E-09	1.67E-09	2.15E-09	2.00E-09	5.24E-09	5.27E-09	1.62E-08

Figure 25: PSD Parameters for TPF optical surfaces.

---

[25] Charley Noecker, "TPF coronagraph wavefront changes due to beam walk," Proc. SPIE 5905, Techniques and Instrumentation for Detection of Exoplanets II, 59050F (14 September 2005).

[26] Stuart B. Shaklan, Luis Marchen, Joseph J. Green, Oliver P. Lay, "The Terrestrial Planet Finder Coronagraph dynamics error budget," Proc. SPIE 5905, Techniques and Instrumentation for Detection of Exoplanets II, 59050D (14 September 2005).

Integrating under the square root of the PSD curves gives the expected RMS wavefront error in the beam. The curves are binned into three spatial bands: low = 0-5 cycles/D, mid = 5 – 30 cycles/D, high = > 30 cycles/D. The starting surface error in each band and the total surface error for each optic are listed in **Table 12**.

Table 12: Calculated RMS surface error for LUVOIR OTA optics using modeled PSDs with TPF parameters.

	TOT (nm RMS)	Low (nm RMS)	Mid (nm RMS)	High (nm RMS)
PM	8.50	2.20	4.91	6.58
SM	9.50	8.56	4.06	0.73
TM	5.25	4.83	2.03	0.35
FSM	1.70	1.67	0.30	0.05

To calculate the sheared wavefront error, the amount of beam walk on each of the LUVOIR A optics is calculated using an optical model provided by the LUVOIR STDT. It is assumed that the PM is the system stop so the beam does not walk on that optic.

6.1   Optic Misalignment

Misalignment of the individual optical surfaces will cause beam walk on the downstream optics. Starting with a simplified, monolithic PM optical model of LUVOIR A, each optic was perturbed in 5 rigid body DOFs (all except clocking) and the resulting beam shear was divided by the perturbation magnitude to yield a sensitivity, as listed in **Table 13**. Sensitivities dX and dY account for lateral shears and dR accounts for radial shears.

Table 13: Beam walk sensitivity (dX/dY/dR) for optic misalignment in 5 DOF (ADE/BDE/ZDE/YDE/ ZDE) on downstream optics (PM/SM/TM). Since the PM is the stop, the beam walk on that optic is zero and is not listed.

PM Perturbation

	ADE dX (nm/nrad)	ADE dY (nm/nrad)	ADE dR (nm/nrad)	BDE dX (nm/nrad)	BDE dY (nm/nrad)	BDE dR (nm/nrad)	XDE dX (nm/nm)	XDE dy (nm/nm)	XDE dR (nm/nm)	YDE dX (nm/nm)	YDE dy (nm/nm)	YDE dR (nm/nm)	ZDE dX (nm/nm)	ZDE dy (nm/nm)	ZDE dR (nm/nm)
SM	0.0	-36.7	0.0	36.7	0.0	0.0	1.0	0.0	0.0	0.0	1.0	0.0	0.0	0.0	0.0
TM	0.0	-712.8	0.0	711.8	0.0	0.0	17.8	0.0	0.0	0.0	17.8	0.0	0.0	0.0	0.0
FSM	0.0	4.7	0.0	-4.8	0.0	0.0	-0.1	0.0	0.0	0.0	-0.1	0.0	0.0	0.0	0.0

SM Perturbation

	ADE dX (nm/nrad)	ADE dY (nm/nrad)	ADE dR (ratio)	BDE dX (nm/nrad)	BDE dY (nm/nrad)	BDE dR (ratio)	XDE dX (nm/nm)	XDE dy (nm/nm)	XDE dR (nm/nm)	YDE dX (nm/nm)	YDE dy (nm/nm)	YDE dR (nm/nm)	ZDE dX (nm/nm)	ZDE dy (nm/nm)	ZDE dR (nm/nm)
SM	0.0	0.0	0.0	0.0	0.0	0.0	-1.0	0.0	0.0	0.0	-1.0	0.0	0.0	0.0	0.0
TM	0.0	41.6	0.0	-41.5	0.0	0.0	-16.8	0.0	0.0	0.0	-16.8	0.0	0.0	-0.1	0.0
FSM	0.0	0.1	0.0	-0.1	0.0	0.0	0.0	0.0	0.0	0.0	0.0	0.0	0.0	0.0	0.0

TM Perturbation

	ADE dX (nm/nrad)	ADE dY (nm/nrad)	ADE dR (ratio)	BDE dX (nm/nrad)	BDE dY (nm/nrad)	BDE dR (ratio)	XDE dX (nm/nm)	XDE dy (nm/nm)	XDE dR (nm/nm)	YDE dX (nm/nm)	YDE dy (nm/nm)	YDE dR (nm/nm)	ZDE dX (nm/nm)	ZDE dy (nm/nm)	ZDE dR (nm/nm)
SM	0.0	0.0	0.0	0.0	0.0	0.0	0.0	0.0	0.0	0.0	0.0	0.0	0.0	0.0	0.0
TM	0.0	0.0	0.0	0.0	0.0	0.0	-1.0	0.0	0.0	0.0	-1.0	0.0	0.0	-0.1	0.0
FSM	0.0	-7.1	0.0	7.0	0.0	0.0	1.2	0.0	0.0	0.0	1.2	0.0	0.0	0.0	0.0

The largest sensitivities for beam walk on the SM/TM are from tilt of the PM ([37,713] nm/nrad respectively) and the largest sensitivity for the FSM is tilt of the TM (7 nm/nrad). There is no meaningful change in radial shear for any of the perturbations shown. The PSDs for the maximum beam walk sensitivities are shown in **Figure 26** and the resulting wavefront errors are listed in **Table 14.** Low spatial frequencies contribute less error since they change very slowly over the

small shear distances. Thus, the mid and high spatial frequencies have the peak contributions in the sheared footprint.

Figure 26: Original and Sheared PSDs on the SM/TM/FSM for the maximum beam walk sensitivities of [37,713,7] nm for 1 nrad of PM Tilt (SM/TM) and 1 nrad of TM tilt (FSM).
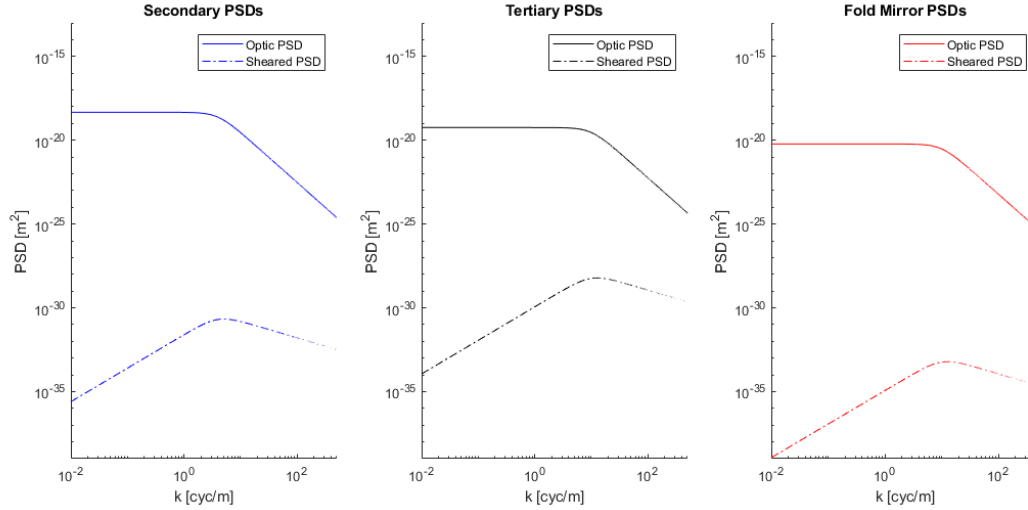
Table 14: Wavefront error from maximum beam walk sensitivities of [37,713,7] nm for 1 nrad of PM Tilt (SM/TM) and 1 nrad of TM tilt (FSM).

	TOT (pm RMS)	Low (pm RMS)	Mid (pm RMS)	High (pm RMS)
SM	0.018	0.005	0.010	0.013
TM	0.423	0.155	0.280	0.277
FSM	0.001	0.001	0.001	0.001

While these values approach the ~ 1 pm threshold of concern, they should be compared to the aberrations that result from the beam reflecting off a different part of the ideal surface shape (rather than a different part of the manufacturing residual). For PM tilt of 1 nrad, the added total wavefront error is ~30 pm RMS (primarily low order Zernikes like coma and astigmatism), two orders of magnitude larger. Thus, the impact of spatially varying manufacturing residuals at the levels shown in **Table 13** is negligible if the aberrations from the shear on the ideal surfaces shapes from optic misalignments are well controlled.

6.2   Line of Sight

Controlling the LOS due to instability in the observatory pointing is achieved by measuring the beam location at the image plane and driving it to a set pixel position using two tilt degrees of freedom on the FSM. However, the LOS wander is uncorrected on the upstream optics where there will be some beam walk proportional to the magnitude of the observatory pointing stability. In general, the amount of beam walk will be large for optics near image planes and small for optics near pupil planes. Additionally, the correction is only applied in two degrees of freedom to fix position in the image plane but not incident angle, so there will also be some beam walk on the downstream optics (coronagraph and other instruments). The focus of this work is on the OTA

budgets, but this effect will also need to be budgeted in the instrument allocations. The beam walk sensitivity for each optic in the OTA is listed in **Table 15**. The same optical model is used as the previous analysis.

Table 15: Beam walk sensitivity on upstream optics for LOS instability. The PM is the system stop so there is no beam walk on that optic (not listed).

Optic	LOS – Beam Walk Sensitivity (nm/mas)
SM	89
TM	1778
FSM	12

Figure 27 shows the original and sheared PSDs for 1 and 10 milliarcseconds of LOS deviation and **Table 16** lists the expected wavefront error from 1 millarcsecond (mas) of LOS deviation. At this level of LOS stability, the total error is ~ 1.1 pm (driven by the TM). The WFE contribution from walk on the ideal surface shape is 0.03 pm – so this effect will not be mitigated by another part of the budget like the optic misalignment beam walk. Thus, wavefront error from LOS stability will need to be budgeted, assuming 1 mas of pointing control is achievable by the observatory.

Figure 27: Original and Sheared PSDs on the SM/TM/FSM for LOS stability.
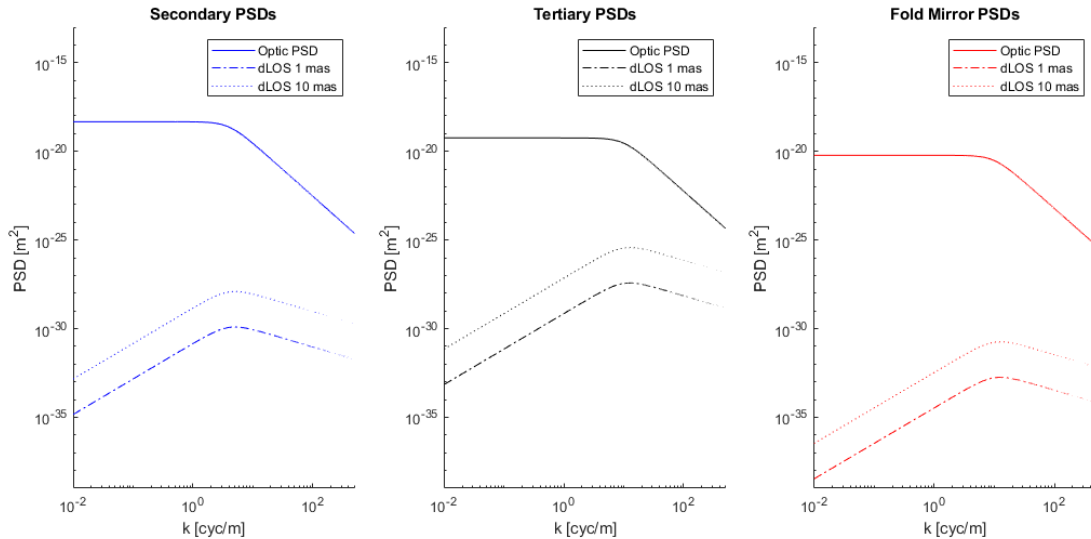
Table 16: Wavefront error on the SM/TM/FSM for LOS stability.

	TOT (pm RMS)	Low (pm RMS)	Mid (pm RMS)	High (pm RMS)
SM	0.042	0.013	0.025	0.032
TM	1.055	0.386	0.698	0.690
FSM	0.002	0.001	0.002	0.001

Since the term cannot be neglected, the temporal nature of the LOS stability must be understood to determine whether improved stability is needed to meet the budget allocations. The contrast stability allocation to LOS/beam walk is approximately one third of the allocation to wavefront stability (**Figure 7**). If the allocations in **Table 6** (top-level wavefront stability budget) are divided by three, the tightest allocation at any temporal frequency for low spatial frequency is 5.8 pm RMS (MF/HF), for mid is 1.7 pm RMS (LF2/MF/HF) and for high is 0.13 pm RMS (LF1/LF2). The expected WFE for 1 mas LOS stability is well below the low/mid allocations, but ~5x larger than the high allocation. However, as explained in Section 4.3, the high spatial frequency allocations may be too restrictive. In addition, if the LOS error is predominantly in the LF3/MF/HF temporal bands (which is likely given the expected noise is dominated by broadband jitter from the FSM servo and structural dynamics above the LOS control bandwidth), the allocation increases to 1.1 pm RMS, right at the expected wavefront error. Higher fidelity simulations will be needed to refine the LOS temporal nature and attenuation from isolators and controls, but initial temporal analysis suggests no significant improvements are needed. However, achieving this 1 mas LOS stability will be challenging and technologies like low-disturbance attitude control or payload isolation will likely be required (see Section 8 for more detail).

Alternatively, this effect could be mitigated with improvements to the high spatial frequency errors in the TM surface finish.

6.3   Beam Walk Technology Gap Assessment

Analysis in this section has shown that the expected wavefront error from individual optics misalignment due to manufacturing residuals is two orders of magnitude smaller than due to the ideal surface shape. However, LOS instability will cause picometer-level contributions to the WFE due to manufacturing residuals but almost no wavefront error from the ideal surface shape, so it must be budgeted. Taking the temporal aspect of the LOS stability into account, the expected WFE is likely to meet the budgeted allocations if 1 mas LOS control can be achieved by the observatory. However, 1 mas LOS stability is challenging, so this is considered a low-TRL gap.

| Beam Walk Gap	Classification	Rationale
1 mas Line of Sight Stability	Low TRL	o If 1 mas LOS stability can be achieved, the contributions to wavefront instability can likely meet allocations. o Achieving 1 mas LOS stability is challenging. Mitigating technologies like low-disturbance attitude control or payload isolation will likely be required (see Section 8 for more detail).

7 *Active Sensing and Control*

The inclusion of active sensing and control loops with the appropriate bandwidths can relax the requirements on the structural and thermal stability of the telescope during a coronagraph observation (see **Figure 9**). This control can be implemented in a number of ways. For one, disturbances can be detected at the primary mirror and the PMSAs can be individually controlled to correct them ("local control"). Another option is to measure the local modes but mitigate the error with an active, potentially deformable, secondary mirror or further downstream at the coronagraph deformable mirrors ("distributed control"). These control schemes can be used individually or in combination to achieve the desired performance. Control of the PMSAs can also be combined with metrology for global motions of the PM and SM (likely needed for both segmented and monolithic PMs), and corrected either locally or with a distributed approach.

A key requirement for the inclusion of active sensing and control systems is that there are available sensors and actuators capable of performing at the picometer level. The sensors need to meet the required specifications for resolution, accuracy and sensing bandwidth. Similarly, the actuators must meet specifications for resolution, accuracy, and control bandwidth; must supply sufficient force/torque to create desired motions; and must have acceptable natural stiffness and damping. This section discusses both the sensing and actuator trades as well as general considerations for designing active sensing and control architectures capable of performing in the picometer regime.

7.1   Analysis Summary

The work documented in this section supports specific elements in the WFE budget. These elements, described in **Figure 28**, are under the major category of OTA Stability. A second tier distinguishes between dynamic effects and dimensional effects. Dynamic effects are generally mechanical or inertial based deformation. These can arise from on-board vibration sources, micro-shock from mechanical actuators, changes in inertial state, etc. Dimensional effects are generally those effects that are driven by a thermodynamic state change in the structure that causes an associated change in the volume or dimensional characteristics of the structures. Such changes can be temperature, loss of mass or density, accumulated radiation damage, internal stress relaxation, etc. Under each second-tier category is a third-tier comprising of the optical subsystems. While wavefront error allocations have been given to all optical subsystems, this analysis focuses on the segmented PM, which is the most complex and is expected to have the tightest requirements. PM Align addresses the positional stability of the collective PMSA segments as a cohesive PM to create a misalignment in the telescope PM optic. PM Figure considers how the PMSA segments move and change relative to each other, creating a figure change in the quality of the PM collective surface. PM Figure can be further broken down into backplane deformations that cause correlated rigid body motions of the PMSAs (Backplane), uncorrelated rigid body motion of the PMSAs (PMSA Align), and higher order surface deformation of the PMSAs (PMSA Figure).
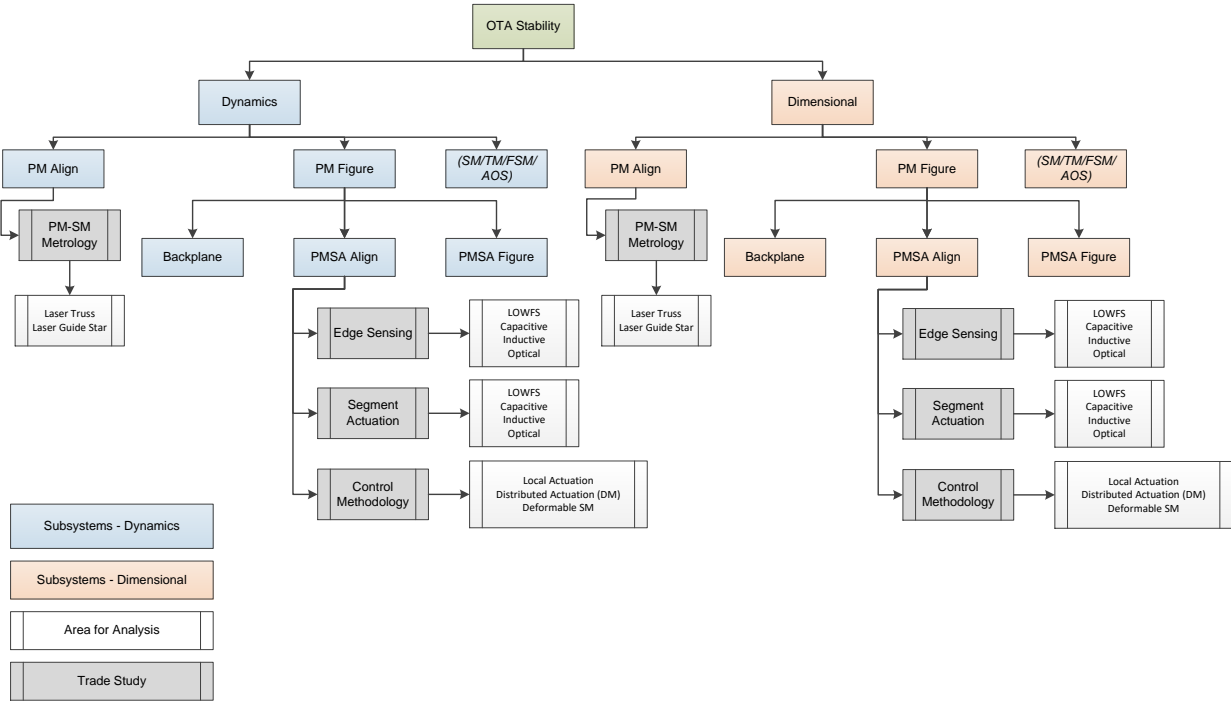
Figure 28: Active Sensing and Control Analysis Summary – defines areas where analysis/trade studies were performed and maps them to the wavefront stability budget structure.

7.2   Sensing

A key piece of the control architecture is sensing of the optic rigid body motions. This includes relative sensing between PMSAs as well global sensing of the monolithic PM and the SM. A trade study matrix of the current capability (COTS/SOTA as appropriate) and system impact of various technologies is listed in **Table 17**. [20,27,28,29,30] It is important to consider the system implications of a particular technology so it does not place a large burden on another system or make the stability problem worse in another regime. A nested control architecture with sensing and control loops running at various sensitivities and bandwidths addresses this concern by targeting specific regimes with appropriate technologies to minimize ripple effects and take advantage of looser requirements to reduce complexity.

---

[27] Fang Shi et. al., "WFIRST low order wavefront sensing and control dynamic testbed performance under the flight like photon flux," Proc. SPIE 10698, Space Telescopes and Instrumentation 2018: Optical, Infrared, and Millimeter Wave, 106982O (30 July 2018).

[28] Martin Wasmeier, Josef Hackl, Samuel Leveque, "Inductive sensors based on embedded coil technology for nanometric inter-segment position sensing of the E-ELT", Proc. SPIE 9145, Ground-based and Airborne Telescopes V, 91451R (22 July 2014).

[29] Klaus Thurner, Francesca Paola Quacquarelli, Pierre-François Braun, Claudio Dal Savio, and Khaled Karrai, "Fiber-based distance sensing interferometry," Appl. Opt. **54**, 3051-3063 (2015)

[30] D. A. H. Buckley, et. al., "A novel optical sensor for mirror edge sensing," Proc. SPIE 7739, Modern Technologies in Space- and Ground-based Telescopes and Instrumentation, 773912 (19 July 2010).

Table 17: Trade Space Matrix for Optics Sensing. Stoplight shading indicates current capability (COTS/SOTA as appropriate) for key metrics.[20,27,28,29,30]

	PMSA Technology need: 4 pm sensitivity at 50-100 Hz (Sensing at 10x expected 5-10 Hz control)					
	PM/SM Technology need: 100 pm sensitivity at 10 Hz (Sensing at 10x expected 1 Hz control)					
Criteria	**1. Segment Level LOWFS/Out of Band WFS**	**2. Capacitive Edge Sensor**	**3. Inductive Edge Sensor**	**4. Optical Edge Sensor (DMI)**	**5. Optical Edge Sensor (Encoder)**	**5. Laser Guide Star**
Performance						
Measurement Sensitivity	12 picometers RMS (Low Order Zernikes)	5 picometers RMS (0-60 Hz integrated, closed loop) in gap	1 nm/sqrt(Hz) for 1-100 Hz in shear; 100 nm/sqrt(Hz) for 1-10 Hz in gap; Could scale for increased sensitivity at mass penalty.	COTS Attocube: 20 pm/sqrt(Hz) up to 100 Hz	15 pm RMS (unknown PSD)	Tunable, can achieve <10 pm RMS control
Measurement Bandwidth	0.01 Hz (~2 min int for Mag 10 stars); Could run faster with less sensitivity?	60 Hz - could adjust/increase with optimized electronics	2 Hz	100 Hz (attocube)	> 1 KHz	Tunable, based on laser power. Can be 100s of Hz for 5 W laser
Measurement Dynamic Range	Needs residual WFE < 0.25 nm RMS (~125 pm segment piston, 500 pr segment tilt)	Set by electronics (A/D) - need factor of 10,000 for 10 nm capture range - 14-bit (achievable)	Microns	mm to m (depends on laser geometry)	> 50 nm	1 nm (postulated)
Propagation from Segment to Full-Aperture	None (independent measurement for each segment)	Edge sensors can't sense full aperture, low order modes well (i.e. focus)	Edge sensors can't sense full aperture, low order modes well (i.e. focus)	Edge sensors can't sense full aperture, low order modes well (i.e. focus)	Edge sensors can't sense full aperture, low order modes well (i.e. focus)	None (independent measurement for each segment)
System Considerations						
Sensor Head SWAP	Nothing local to mirrors; Requires bench for LOWFS optical train (~4 ft x 4 ft x 1 ft for WFIRST)	Large plates needed: 150 mm x 150 mm plates with 0.25 mm gap (paddle configuration)	75 x 75 mm for 4.5 mm gap (estimate from hardware photo)	Small head on mirror edges; Make laser return integrated into mirror substrate?	25 x 25 x 50 mm; Mount side by side on back of mirror	Nothing local to mirrors; Requires sensing camera
Sensor Electronics SWAP	Dominated by needs of sensing camera	Boards needed for all sensors	Electronics needed for all sensors; can have long cables (10 m)	Electronics needed to control laser/sense return	Electronics needed to control laser/sense return	Dominated by needs of sensing camera
Thermal Impact to OTE	Local heating near camera on LOWFS bench - removed from mirrors; Minimal Impact	Electronics will cause some heating - should be slow and correctable. Move away from mirrors if possible	Electronics will cause some heating - should be slow and correctable. Move away from mirrors if possible	Electronics and laser will cause some heating. Can't completely move away from mirrors.	Electronics and laser will cause some heating. Can't completely move away from mirrors.	Local heating near camera on LOWFS bench - removed from mirrors; Minimal Impact
Dynamic Impact to OTE	Minimal impact - no additional moving parts	May have some impact if PMSAs are locally corrected - adds to mass	May have some impact if PMSAs are locally corrected - adds to mass	May have some impact if PMSAs are locally corrected - adds to mass	May have some impact if PMSAs are locally corrected - adds to mass	Minimal impact - no additional moving parts
TRL/risk	Proven performance with WFIRST Testbeds (Shi et al); Low Risk	Electronics proven at Ball for different plate geometry, target bandwidth; Potential to optimize for this application without losing performance; Some risk	Development for E-ELT; Laboratory testing completed; Some risk for space mission	Attocube is COTS system and has been tested in ambient vacuum; Some risk for space mission	In development for SALT; Some risk for space mission	High TRL components (LaserCom Hertiage); Low risk for space mission
Other Complexity	Another optical system to include in coronagraph instrument.	Lots of wiring; How to implement paddle configuration with deployable mirrors.	Lots of wiring; Inductive sensor degradation from temperature instability	Lots of wiring; power for lasers could add up; Stray light. Dynamic range limited to maintain return.	Must be light tight/requires flexible boot - how to implement with mirror deployment? Small dihedral angle range (~1 mrad)	Requires additional spacecraft with formation flying; Potential to introduce non-common path errors.

The key path to maturation for many of the sensing technologies listed in **Table 17** is to develop a sensing head that can accommodate the LUVOIR segment geometry and to develop readout electrics with sufficiently low noise to enable picometer-level precision.

In addition to sensing technologies trades, there are also trades in the sensing architecture that can be made. For example, out of plane rigid body PMSA motions (particularly PTT) have a greater impact on stability than in-plane motions (decenter/clocking).[6] This fact should be considered when specifying edge sensors, if included, whose design should be optimized to detect those DOFs. If the sensitivities are small enough, it may also be possible to meet allocations with sensing (and correcting) the PMSA motion in 3 DOFs rather than 6 – which would save mass, power and algorithm complexity. On the other hand, implementation of a sensing system capable of detecting segment figure deformations (like a LOWFS or Laser Guide Star) might allow for local radius of curvature or higher order figure corrections, would could take some burden of downstream deformable mirrors.

7.3   Actuators

If the control architecture involves moving either the primary mirror segments or the secondary mirror, the actuators that are the most applicable are piezoelectric or voice coil actuators.[31] These actuators allow for high precision and high frequency actuation but only over small distances. Given this limitation, these actuators would be used only for the active wavefront error disturbance rejection control during a coronagraph observation (or other science instrument observation requiring similar stability). Other actuators would need be used in conjunction with these to align and phase the optical system. The two-stage nanometer-class actuator used on Webb could be a potential base for a new three stage "ultra-fine" actuator if proven stable enough.

The main difference between piezoelectric and voice coil actuators are the natural stiffnesses associated with the actuators. Piezoelectrics are considered "hard" actuators and voice coils are considered "soft". The preferred actuator depends on the system, its natural dynamics and frequency characteristics of both the system and the control.[32] For example, voice coil actuators provide more damping to the system which can be desirable for mitigating high frequency disturbances. However, piezoelectric actuators enable a more a stable coupling between the structure and the mirrors. As the stability budget matures and provides better understanding for which regime is limiting (or which regime isn't mitigated by structural damping/isolation), there can be down-select to a preferred actuator type. In the meantime, work is ongoing to develop integrated modeling tools that would incorporate the structure, actuation, and control interaction to quantify the difference between voice coil and piezoelectric actuators.

7.4   Control Methodology

One obvious control solution is to sense perturbations at the PMSAs and apply an equal and opposite correction to the same segment ("local control"). This control strategy is advantageous

---

[31] Thompsona, Peter M. et al. "Servo design and analysis for the Thirty Meter Telescope primary mirror actuators." (2010).

[32] M. Dimmler, P. Barriga, M. Cayrel, F. Derie, A. Foerster, F. Gonte, J. C. Gonzalez, L. Jochum, N. Kornweibel, S. Leveque, C. Lucuix, L. Pettazzi, "Getting ready for serial production of the segmented 39-meter ELT primary: status, challenges and strategies," Proc. SPIE 10700, Ground-based and Airborne Telescopes VII, 1070043 (6 July 2018).

because it uses a simple control design and would isolate the control solution to the individual segments. A drawback to this control strategy is that it does not leverage the full knowledge of the system to find a globally optimal solution. In addition, actuation of the segments will put reaction forces and torques into the mirrors and structure, potentially deforming the mirrors further and making the control interaction more difficult to regulate. The magnitude of the forces and torques depend on many factors including the control design, the structural natural frequencies and damping and actuator control frequencies. An example of the reaction forces acting on a mirror due to the control actuators as a function of frequency can be seen in **Figure 29**, where the reaction force is normalized by the input disturbance magnitude. The left plot has 2 system natural frequencies at 0.1 Hz and 2 Hz (arbitrarily chosen) and the right plot has two natural frequencies at 4 Hz and 15 Hz – these resonances can be tuned with mirror/structural design. This type of analysis is essential when designing the control system; there must be a balance between mitigating forces that must be actively controlled to meet performance requirements (i.e. not controlled by passive or active damping outside the actuators) and imposing limits on corrections that would result in too high of forces into the mirrors or structure – potentially causing more deformations than the control system is attempting to fix.
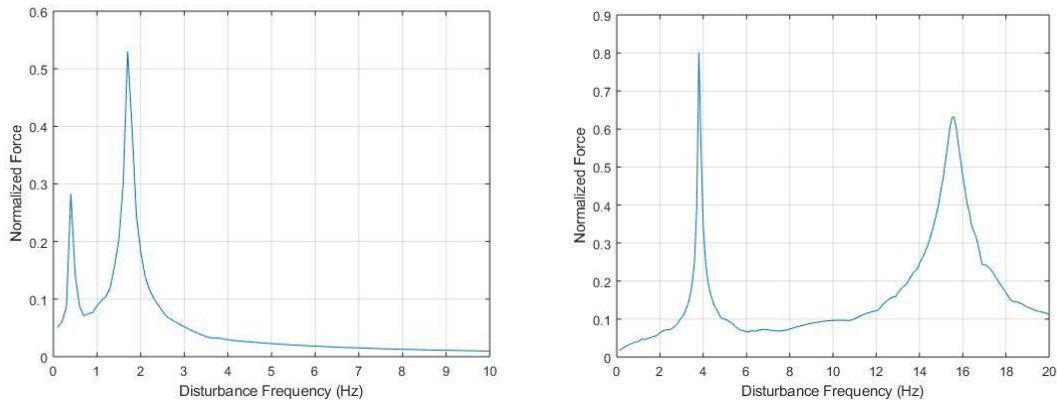
Figure 29: Normalized reaction force with respect to disturbance frequency. System 1 (left) has two natural frequencies at 0.1 and 2 Hz. System 2 (right) has two natural frequencies at 4 and 15 Hz. The structural design can be tuned to shift these responses (while balancing other considerations). Near these frequencies, the performance of the control system degrades.

A more complex solution to this problem is using "distributed control" to mitigate disturbances in the primary mirror.[33] This control technique is promising because it considers all the sensing information available and can find a solution to minimize the structure-control interaction. A drawback to this control strategy is that it is a much more complicated control architecture.

Either control solution will require system simulation to characterize the performance and interaction dynamics of the actuator, mirrors, and structure as well as the control methodology chosen. The tools to model these interactions are currently in development.

---

[33] Baris Ulutas, Daniel Kerley, Jennifer Dunn, Afzal Suleman, Edward J. Park, "Distributed H∞ control of dynamically coupled segmented telescope mirrors: Design and simulation", Mechatronics, Volume 22, Issue 1, (2012).
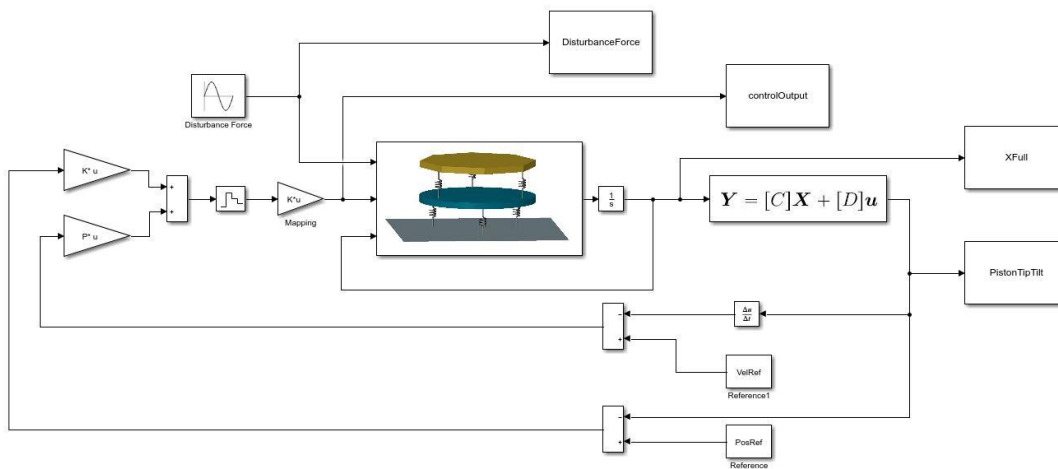
7.5 Control Simulations – Disturbance Rejection

Preliminary analysis has been completed on disturbance rejection control, first focusing on the local control problem. A simplified diagram showing a schematic of this analysis can be seen in **Figure 30**. This is a six degree of freedom dynamical system where the goal is to reject an input disturbance force being placed into the platform and control the inertial piston, tip, and tilt of the PMSA.

A closed loop control system was developed and a high-level schematic can be seen in **Figure 31**. The initial control design is a proportional derivative (PD) controller where the feedback states are the piston, tip and tilt of the mirror. Although a PD controller is not the optimum solution, [34] it is still capable of rejecting a disturbance and is a good initial approach to understand the details and driving parameters of this problem.
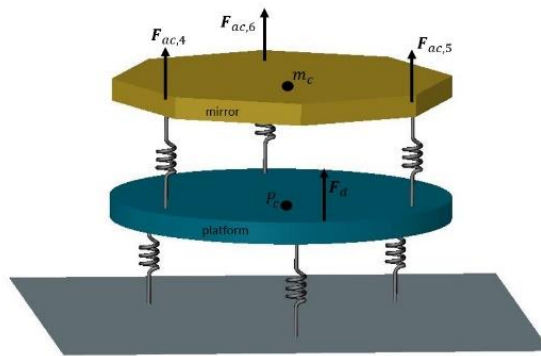

Figure 30: Schematic of primary mirror system used for local disturbance rejection control. PMSA and structure are modeled as masses coupled by springs and dampers, where the masses and spring constants can be parameterized to find an optimal solution.

Figure 31: Block diagram for analyzing closed loop disturbance rejection control of a single PMSA.

---

[34] J. Han, "From PID to Active Disturbance Rejection Control," in IEEE Transactions on Industrial Electronics, vol. 56, no. 3, pp. 900-906, March 2009. doi: 10.1109/TIE.2008.2011621

Results from one run of the simulation can be seen in **Figure 32**. The control gains were tuned for the natural system frequencies and the input frequency to be rejected. As discussed previously, the simplicity of this local control is desirable but it ignores the structure control interaction. To fully understand the feasibility of this control scheme, future work will utilize integrated modeling techniques and determine the structural and performance constraints associated with using local primary mirror control.
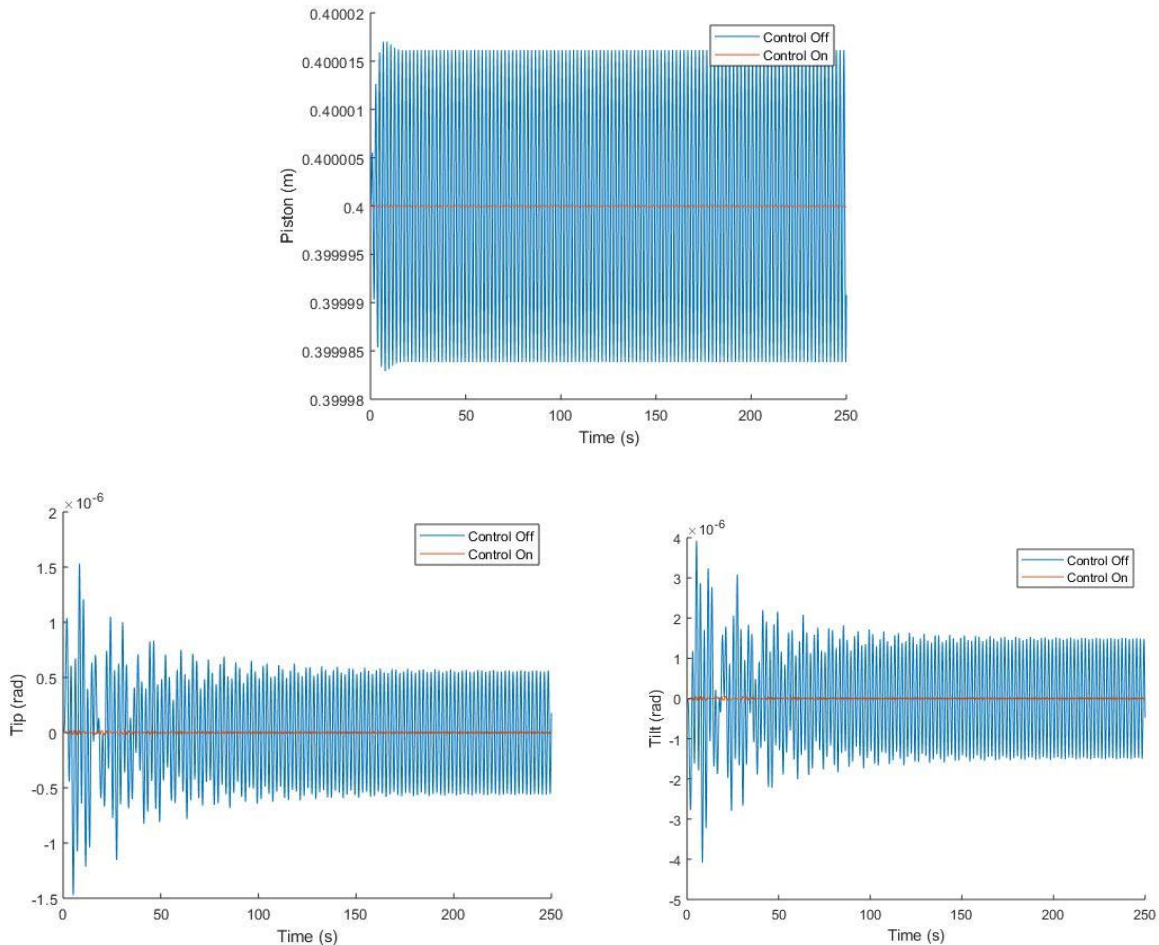
Figure 32: Simulation results of disturbance rejection of local segment piston (top), tip (bottom left) and tilt (bottom right) using a PD controller. As expected, the controller is able to significantly reduce input disturbances.

Additional simulations were performed to probe the controller response. One metric used to define the performance of a disturbance rejection controller is the percentage of the disturbance that is rejected. Using the same system as the analysis shown in the left plot of **Figure 29**, the disturbance rejection performance for an input force with constant magnitude but varying frequency is shown in **Figure 33**. This shows that near the system natural frequencies not only are the reaction forces the highest, but the controller performance is the worst. Thus, the natural frequency of the system is an important parameter both for reaction forces/torques and for controller performance. Future work using integrated modeling can quantify the system performance using representative structures and optics, as well and input dynamic disturbances from the spacecraft and payload.

42
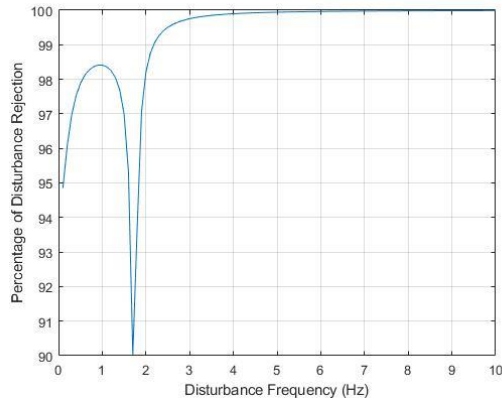
Figure 33: Disturbance rejection with respect to input disturbance frequency for a system with natural frequencies at 0.1 and 2 Hz

Additionally, **Figure 33** shows that as the disturbance frequency increases, the disturbance rejection performance increases. This can be attributed to the passive disturbance rejection of the system due to natural damping. **Figure 34** shows the relationship between the natural damping of a system and the corresponding passive-only disturbance rejection. These results demonstrate that a combination of passive damping and active disturbance rejection may be the best solution to minimize disturbances while keeping the active systems as simple as possible.
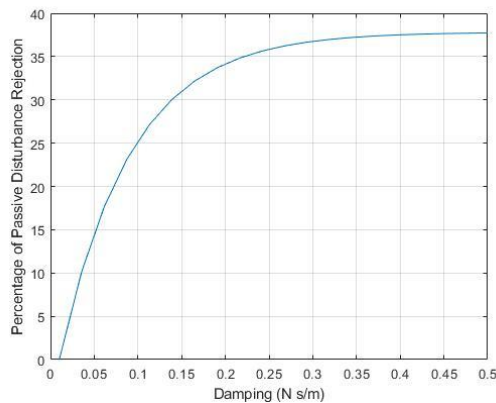
Figure 34: Passive disturbance rejection with respect to damping coefficient

All of these results assume that the bandwidth of the controller has been properly selected, which is also a function of disturbance frequency. As the input disturbance frequency increases, the required bandwidth of the controller increases in order to adequately sample the disturbance, calculate a response, and apply that response, as in **Figure 35**.
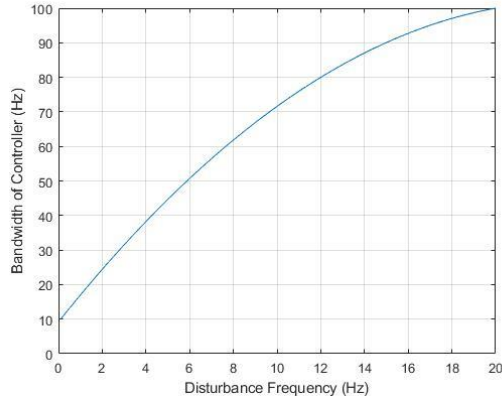
Figure 35: Effect of input disturbance frequency on the selected control bandwidth

7.6   Actuation Impact on PMSA Figure

In addition to creating reaction forces and torques into the mirrors and structures, actuation of the PMSAs will distort their surface figure at some level. To evaluate the rough order of magnitude of this effect, assume a PMSA is corrected in piston over a ± 1 nm range at 10 Hz. The motion is given by:

$$x(t) = (1\ nm) \cdot \sin(10 Hz \cdot t) \tag{11}$$

The acceleration is the second derivative of the equation of motion, with a maximum value of 100 nm/s^2 or ~0.01 µg. The sensitivity of the PMSA surface figure to 1 µg of axial acceleration is a change of 0.3 pm RMS, most of which is trefoil (see **Figure 66** in Section 10.2). At the expected 0.01 µg acceleration, this error is negligible. If the actuation profile is more like a square wave than a sine wave, the maximum acceleration will increase. However, it is unlikely this effect will be a driving factor in the error budget and it can be further evaluated in the control simulations described in this section.

7.7   Thermal Control

Given the tight requirements on stability, the LUVOIR STDT is baselining a thermal control system that will keep all parts of the observatory at 270 ± 0.001 K at bandwidths below a few Hz.[35] The study has evaluated thermal impacts as sensitivities and assumes 1 mK temperature stability to compare expected perturbations to allocations. The thermal sensing and control system is a mid-TRL gap and is an important aspect to be demonstrated on a large, complex system.

---

[35] Sang C. Park, Michael J. Eisenhower, Marcel Bluth, Matthew R. Bolcar, Lee D. Feinberg, J. Scott Knight, David C. Redding, "LUVOIR backplane thermal architecture development through the composite CTE sensitivity study," Proc. SPIE 10398, UV/Optical/IR Space Telescopes and Instruments: Innovative Technologies and Concepts VIII, 103980D (5 September 2017).

7.8   Active Control Technology Gap Assessment

The following list presents a summary of the analysis areas studied and the technology gap classification. There are multiple low and mid TRL gaps in the area of active sensing and control that are high priority for near-term development.

Active Control Gap	Classification	Rationale
Segment Dynamic Sensing and Control	Low TRL	o There are several candidate technologies for sensing and actuation of PMSAs that approach the required picometer sensitivity, but have not been proven in a LUVOIR-like geometry.
System Control Methodology	Low TRL	o Need simulations of nested control loops to refine performance requirements for each (avoid overly restrictive requirements when multiple loops are present). o Need simulations of local vs. distributed control to evaluate best system-level solution. o Need hardware demonstrations of system-level active sensing and control.
Thermal Sensing and Control	Mid-TRL	o Systems have been simulated; Need demonstration of mK-level thermal sensing and control over large structures and lightweighted optics.

8 *Low Disturbance Architectures*

Another method to provide relief on the telescope structure and optics is to minimize the input disturbances, rather than sense and correct them. This area was not a focus of the ULTRA study, but potential mitigation strategies are discussed below. They may be particularly relevant to achieving the 1 mas LOS stability discussed in Section 6.

8.1   Quiet Spacecraft

Spacecraft attitude control, station keeping, and momentum management are major contributors to dynamic perturbations in the observatory. Like the active sensing and control strategies discussed in Section 7, spacecraft control is often a tiered architecture consisting of a coarse pointing mode (star trackers and thrusters) and a fine pointing mode, plus additional LOS control in the payload itself via the FSM and LOWFS. Precision spacecraft pointing technologies like reaction wheel assemblies (RWAs), control moment gyroscopes (CMGs), and microthrusters can be traded to meet mission needs by considering how their disturbance PSDs will couple into payload dynamics, especially excitation of appendage modes and other structural resonances. Microthrusters are a newer technology and have undergone significant development in recent years to achieve very low output disturbances.[36] HabEx will employ microthursters to leverage these low levels, but the force is insufficient to point LUVOIR at the required rates, so that mission will use a combination of CMGs and payload isolation to achieve the necessary performance.[37,38] The LUVOIR STDT may also investigate a hybrid approach, where CMGs are used to point the telescope, then microthrusters maintain pointing during science observations.

8.2   Payload Isolation

If the spacecraft disturbances require additional mitigation, the payload can be isolated from the spacecraft using passive or active methods. Passive methods rely on damping in the structure, which cannot achieve broadband suppression and must be balanced with the stiffness needed to maintain alignment of the optics. Active methods rely on sensing and actuation of the payload to cancel the input disturbances. Possible candidates for active systems include the Vibration Isolation and Precision Pointing System (VIPPS) from Lockheed Martin, based on its Disturbance Free Payload (DFP) technology, which is included in the LUVOIR baseline architecture.[39,40,41]

---

[36] Chapman, P., Colegrove, T., Ecale, E., & Girouart, B. "Gaia Attitude Control Design: Milli-Arcsecond Relative Pointing Performance using Micro-Thrusters and Instrument in the Loop," 8th Int Conf Guid Navig Control Syst (2011).

[37] "The LUVOIR Mission Concept Study Interim Report" arXiv:1809.09668 (2018).

[38] Milan Mandić, Oscar Alvarez-Salazar, Alina A. Kiessling, "HabEx: A high-precision pointing architecture using microthrusters and a fine steering mirror," Proc. SPIE 10698, Space Telescopes and Instrumentation 2018: Optical, Infrared, and Millimeter Wave, 106980U (6 July 2018).

[39] Gonzales, M. et al, "Unprecedented vibration isolation demonstration using the Disturbance-Free Payload Architecture," AIAA Guidance, Navigation and Controls Conference (2004).

[40] Lia W. Sacks, et. al., "Preliminary jitter stability results for the large UV/optical/infrared (LUVOIR) surveyor concept using a non-contact vibration isolation and precision pointing system," Proc. SPIE 10698 (16 July 2018).

[41] Dewell, L. et al, "Dynamic Stability with the Disturbance-Free Payload Architecture as Applied to the Large UV/Optical/Infrared (LUVOIR) Mission," Proc. SPIE 10398 (2017).

Published transmissibility curves can be used to estimate attenuation of spacecraft disturbances on the optical payload in various temporal bands, as in **Figure 36**.
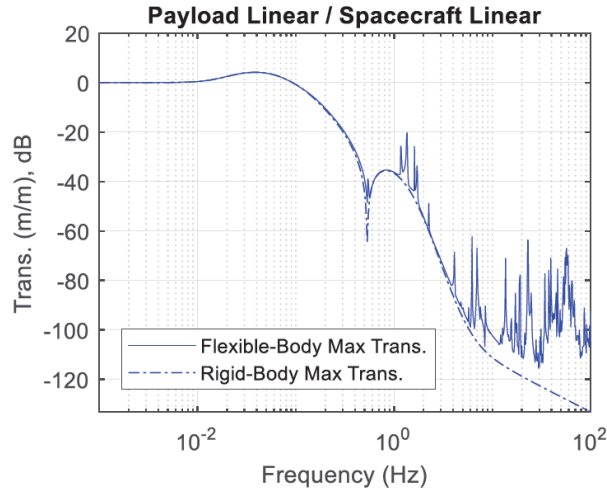
Figure 36: Transmissibility curve for VIPPS on the LUVOIR architecture (integrated modeling results). There is significant attenuation at frequencies above 1 Hz.

8.3 Low Disturbance Mechanisms

Even if the payload can be perfectly isolated from the spacecraft, mechanisms in the telescope and science instruments will also cause dynamic disturbances. Potential sources include the FSM actuation for LOS control and filter/pupil wheels that rotate into beam for various science observations. Dynamic actuation residuals in these optical elements with have a direct impact on the wavefront stability. Future work should characterize these potential disturbances, especially through end-to-end simulations.

## 8.4 Low Disturbance Architectures Technology Gap Assessment

The following list presents a summary of the technology gap classification. There are currently no low or mid-TRL technology gaps, but the knowledge gap for low disturbance mechanisms may become one as more analysis is performed.

Gap	Classification	Rationale
Payload Isolation	Engineering Gap	o Preliminary analysis of VIPPS has shown expected performance can meet LUVOIR LOS stability and agility requirements. o VIPPS is based on demonstrated DFP technology, but likely requires engineering work to realize.
Low Disturbance Mechanisms	Knowledge Gap	o Need integrated modeling to determine stability impact.

9 Stable Structures

9.1 Analysis Summary

The work documented in this section supports the mirror and mirror mounting elements in the WFE budget. While wavefront error allocations have been given to all optical subsystems, this analysis focuses on the segmented primary mirror, which is the most complex and is expected to have the tightest requirements. The key areas of analysis and trade studies covered in this section are represented graphically in **Figure 37**. It is assumed that these structures will be used in conjunction of the active, optical sensing and control described in the previous section, so they must provide stability that is within the capture range of those systems.
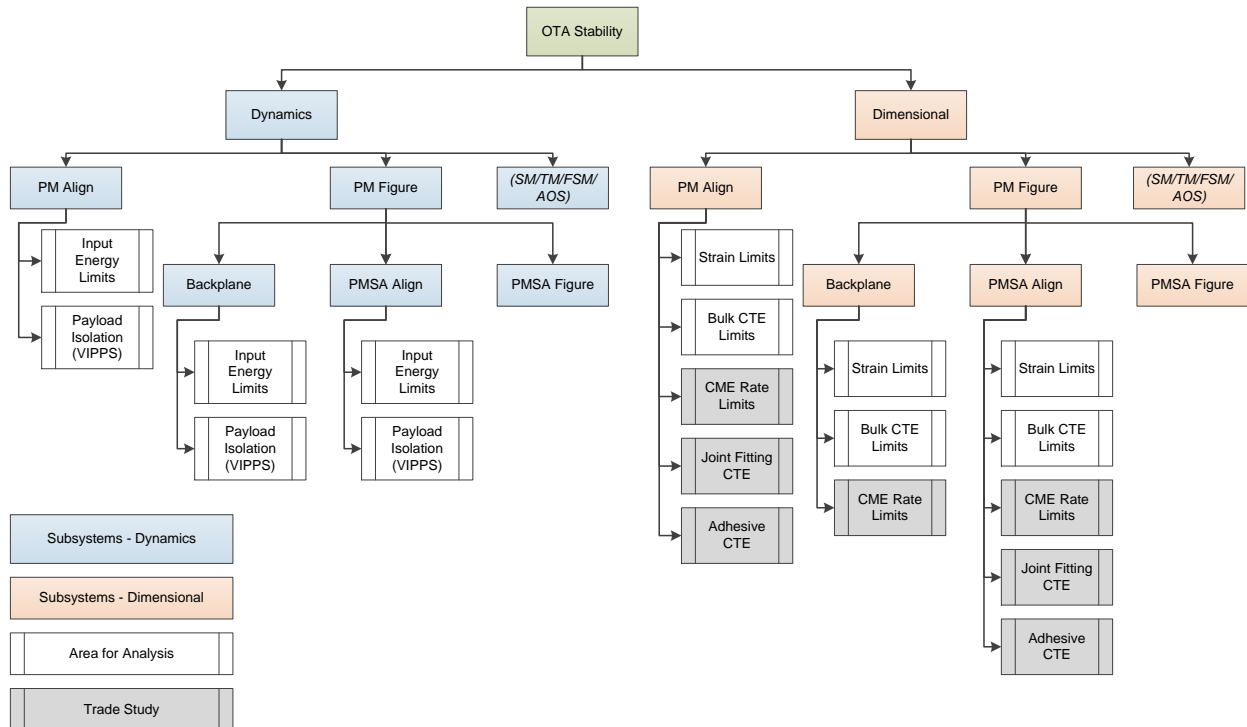
Figure 37: Stable Structures Analysis Summary – defines areas where analysis/trade studies were performed and maps them to the wavefront stability budget structure.

9.2 Modeling Summary

The analyses performed in the following sections are the result of a compilation of several models and methods. In some cases, the analysis is direct engineering calculations to estimate order of magnitude characteristics. The other cases used finite element models to explore response characteristics.

9.2.1 Models for Sections 9.3.1 – 9.3.4, 9.4.1 – 9.4.6

An architecture for the LUVOIR Primary Mirror Backplane (PMBP) was derived from the Webb manufacturing and performance lessons learned. The details of the architecture are described in **Figure 38**. The architecture also used available material engineering methods to arrive at a design that was ~50% less mass than the current baseline architecture. The analysis model is comprised

of a single wing segment. The size and configuration were based on the LUVOIR Architecture B, which is the off-axis arrangement. This model supported assessment of thermal transients, hinge line influences, bulk and component material CTE sensitivities and some dynamics.
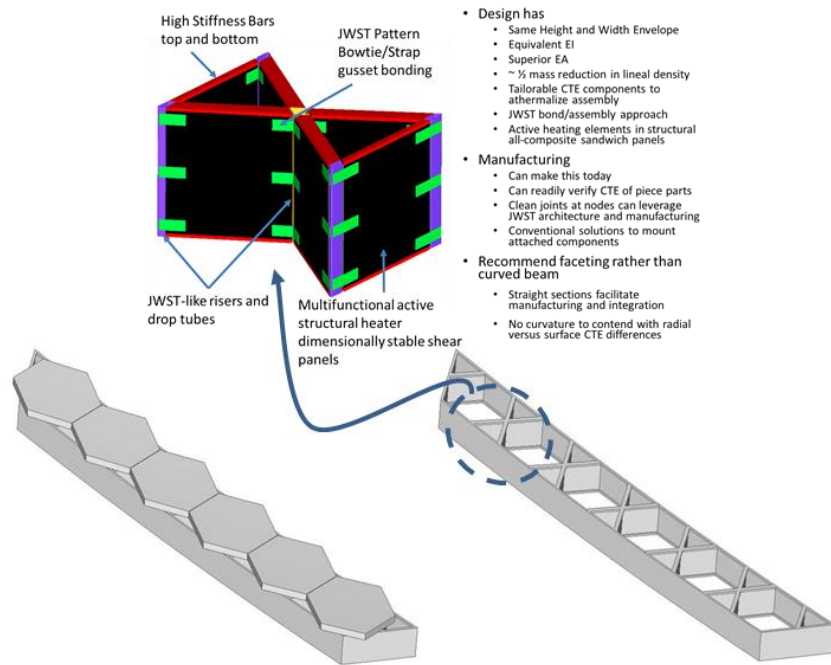
Figure 38: An architecture for a single wing of the LUVOIR PMBP was developed. The model was converted to a finite element model and used to evaluate thermal transient sensitivities, material CTE sensitivity and to assess some initial temperature control characteristics.

9.2.2 Models for Sections 9.3.5 – 9.3.6, 9.4.7, 9.5.1

The 1409 Primary Mirror Backplane Support Stucture (PMBSS) model is the latest model used to evaluate the alignment and stability requirements for the Webb backplane. This model primarily consists of 3-dimensional brick elements representing NGIS-provided hardware. This model also contains representations of the mirrors, electronics, sensors, and radiators. These models come in different form, with some represented as DMIGs, shell and beam models, and some representative interface forces.

9.3 Thermal Effects

The analysis of performance sensitivity to temperature fluctuations for a LUVOIR type system is novel in the sense that the system is being configured with active controls. This brings in a temporal aspect that hasn't warranted consideration explicitly for structures on previous systems. Initial studies performed by SAO indicate that controlling the structure to a level of ±0.5 mK over time scales in the mid-temporal frequency domain (~1 Hz) is a reasonable assumption for our present purposes.[35] This study will investigate the degree of coupling between thermal control authority and CTE control obligations.

The analysis is arranged in blocks that mimic the wavefront stability budget matrix. The following sections cover evaluations of the degrees of freedom in PM Alignment and PM Figure for dimensional stability that can be substantively addressed in these early stages. For example, the level of analysis that is afforded in this phase permits only analyzing PM Align in despace – the shears, tilts and clocking are more complex and require more rigor in assumptions about the structural architecture and will need to be addressed in a future phase. PM Figure – PMSA Align is evaluated for all six degrees of freedom in the PMSA 6 DOF motion allocations.

9.3.1 PM Align – Despace

The analysis for this WFE budget element was assessed with an engineering calculation. The temporal domains of the budget allocation are considered by evaluating a strain rate and relating this to a temperature rate of change and PMBP bulk average CTE. Equation [12] shows this relationship:

$$\dot{\epsilon} = \frac{Allocation}{LP} = \frac{Allocation\ F}{L} = \alpha \Delta \dot{T} \qquad [12]$$

The elements in [12] are defined as follows: $\dot{\epsilon}$ is the maximum strain rate limit; Allocation is the maximum PM piston allocated in the budget; L is the effect length of the PMBP structure that affects piston and is assumed to be 0.5 m for this study; F in Hz and P in seconds are the telescope update cycle Frequency and Time interval respectively (note that F = 1/P); α is the PMBP bulk CTE in the V1 direction; $\Delta \dot{T}$ is the temperature drift rate.

The equation in [12] can be rearranged to relate α and $\Delta \dot{T}$. The results of this are shown in **Figure 39** for each of the temporal domains. Another perspective is to couch the maximum permitted temperature change against bulk CTE. This result is shown in **Figure 40**. Both figures are the same data, just presented in a different perspective.

The allocations used here are derived from in the top-level OTA Stability Budget in **Table 6** flowed down the OTA Dimensional Stability branch to the PM Align box. These allocations further assume a control system (like the laser truss) is compensating for PM Align motions below 1 Hz (LF1-LF3 bands) with 1% residuals (100 pm / 10 nm). Thus the LF bands have additional relaxation compared to the MF/HF bands.
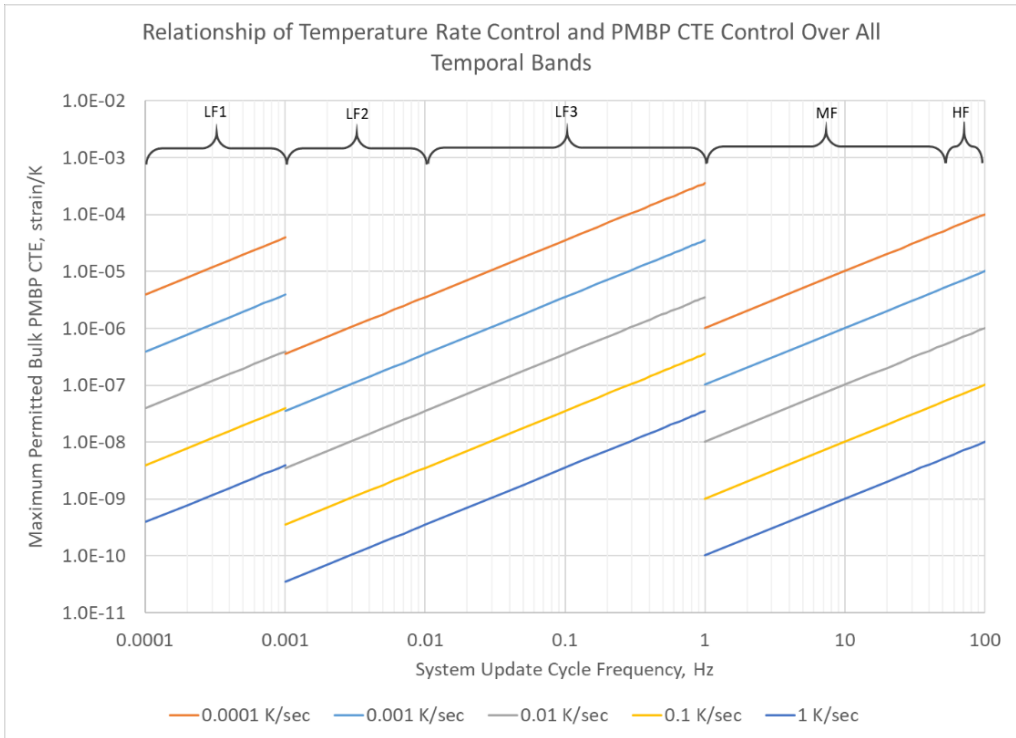
Figure 39: Maximum permitted CTE for PM Align - despace allocation over all temporal domains for several thermal control system temperature rate levels.
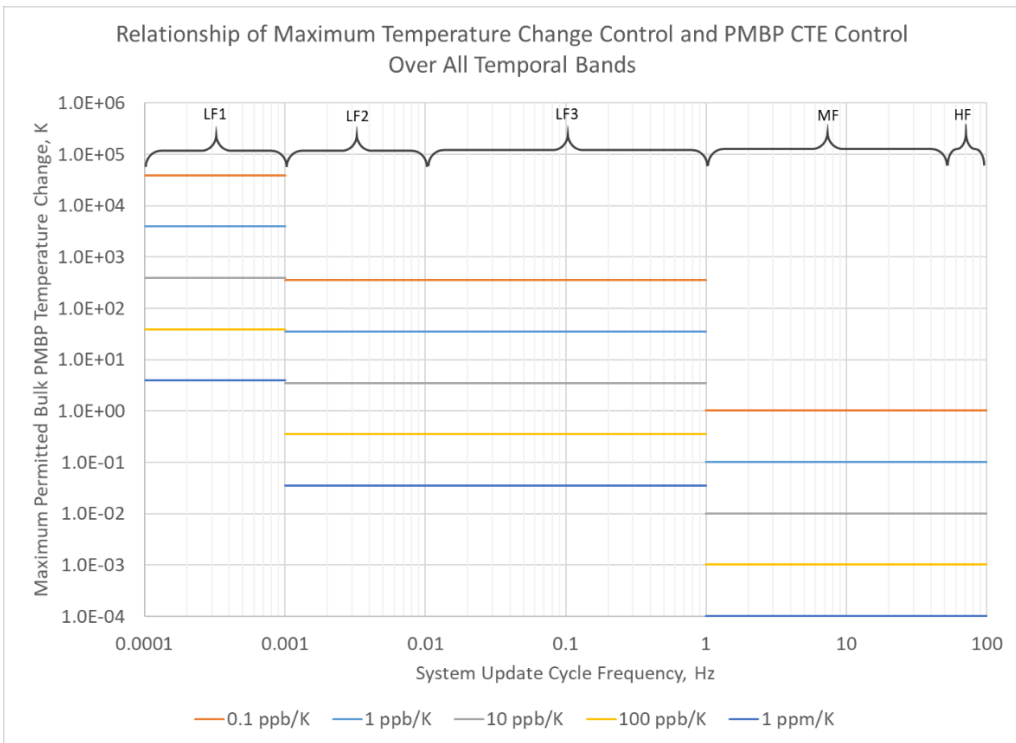
Figure 40: Maximum permitted Bulk Temperature change for PM Align - despace allocation over all temporal domains for several PMBP bulk CTE magnitudes.

A practical lower limit for CTE control is on order 1 ppb/K. Given that limit as a constraint, **Figure 39** suggests a thermal control system temperature rate change between 0.01 K/sec and 0.1 K/sec will be acceptable and is driven by allocations in the LF2 and MF temporal domains. Similarly, **Figure 40** suggests that a maximum temperature drift of up to 5 K is acceptable in the LF2 and LF3 domains and 0.1K in the MF and HF domains. Better thermal control than this will alleviate pressure on the material CTE requirements.

Correction for Updated Stability Budget: The updated LF1-lo allocation is 10x tighter (all others are looser). If the **Figure 39** and **Figure 40** LF1 curves also get 10x tighter, none of the previous conclusions change and there may be additional relief at other temporal bands.

9.3.2 PM Figure – PMSA Align

The PMBP influence on the PMSA pose dimensional stability resulting from temperature changes was evaluated using the LUVOIR Wing Model described in Section 9.2. The analysis consisted of applying a temperature change of ±0.5 mK at a 4 Hz cycle rate to the model with baseline material properties. The analysis was repeated with all CTE values offset by 1 ppm/K. The rigid body or common motion of the 6 mirror segments is removed from each case and the residual is then evaluated as PMSA pose displacement. This method afforded estimates of sensitivity for V1 and V3 displacements and V2 and V3 Tilts. V2 displacement and V1 clocking were not sufficiently determinant with the limited model.

The results of the analysis are summarized in **Table 18**. The sensitivities are constant across all temporal bands. The allocations are applied to the sensitivities to estimate maximum permitted temperature changes in each temporal band for several CTE magnitudes. The results are color coded according to the guidelines in **Figure 41** to illustrate operational zones and balance the shared burden between temperature control authority and material CTE tailoring and control.
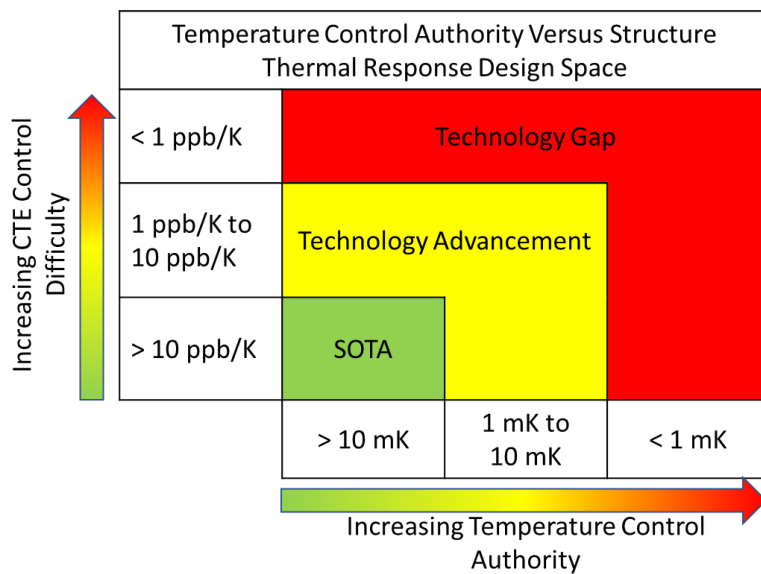
Figure 41: Guidelines for evaluating the level of technical difficulty for Material CTE Producibility and PMBP Temperature Control Authority

Table 18: Sensitivities for PMSA Pose Stability Budget Terms and an assessment of level of difficulty for CTE and Temperature control authorities across temporal categories.

PMSA Pose V1 DESPACE					
Allocation (m or rad)	3.84E-08	3.42E-10	3.42E-10	9.24E-11	6.93E-13
Sensitivity (m/K/(ppm/K))	1.32E-01	1.32E-01	1.32E-01	1.32E-01	1.32E-01
Temporal Zone	LF 1	LF 2	LF 3	MF	HF
Bulk CTE (strain/K)	Calculating Temperature Change Permitted				
1E-06	3E-01	3E-03	3E-03	7E-04	5E-06
1E-07	3E+00	3E-02	3E-02	7E-03	5E-05
1E-08	3E+01	3E-01	3E-01	7E-02	5E-04
1E-09	3E+02	3E+00	3E+00	7E-01	5E-03
1E-10	3E+03	3E+01	3E+01	7E+00	5E-02
PMSA Pose V2 Tilt					
Allocation (m or rad)	2.05E-07	1.82E-09	1.82E-09	3.37E-11	3.64E-12
Sensitivity (rad/K/(ppm/K))	1.88E-01	1.88E-01	1.88E-01	1.88E-01	1.88E-01
Temporal Zone	LF 1	LF 2	LF 3	MF	HF
Bulk CTE (strain/K)	Calculating Temperature Change Permitted				
1E-06	1E+00	1E-02	1E-02	2E-04	2E-05
1E-07	1E+01	1E-01	1E-01	2E-03	2E-04
1E-08	1E+02	1E+00	1E+00	2E-02	2E-03
1E-09	1E+03	1E+01	1E+01	2E-01	2E-02
1E-10	1E+04	1E+02	1E+02	2E+00	2E-01
PMSA Pose V3 Tilt					
Allocation (m or rad)	2.05E-07	1.82E-09	1.82E-09	3.37E-11	3.64E-12
Sensitivity (rad/K/(ppm/K))	8.83E-02	8.83E-02	8.83E-02	8.83E-02	8.83E-02
Temporal Zone	LF 1	LF 2	LF 3	MF	HF
Bulk CTE (strain/K)	Calculating Temperature Change Permitted				
1E-06	2E+00	2E-02	2E-02	4E-04	4E-05
1E-07	2E+01	2E-01	2E-01	4E-03	4E-04
1E-08	2E+02	2E+00	2E+00	4E-02	4E-03
1E-09	2E+03	2E+01	2E+01	4E-01	4E-02
1E-10	2E+04	2E+02	2E+02	4E+00	4E-01

| PMSA Pose V3 Decenter					
Allocation (m or rad)	1.61E-06	1.44E-08	1.44E-08	3.87E-10	2.85E-11
Sensitivity (m/K/(ppm/K))	4.65E+00	4.65E+00	4.65E+00	4.65E+00	4.65E+00
Temporal Zone	LF 1	LF 2	LF 3	MF	HF
Bulk CTE (strain/K)	Calculating Temperature Change Permitted				
1E-06	3E-01	3E-03	3E-03	8E-05	6E-06
1E-07	3E+00	3E-02	3E-02	8E-04	6E-05
1E-08	3E+01	3E-01	3E-01	8E-03	6E-04
1E-09	3E+02	3E+00	3E+00	8E-02	6E-03
1E-10	3E+03	3E+01	3E+01	8E-01	6E-02

Correction for Updated Stability Budget: The updated LF1-mid allocation is 20x tighter (all others are within 2x of original or looser). However, the allowable temperature changes at LF1 are much larger than SOTA capability, so none of the previous conclusions change.

9.3.3 Thermal Control – Spatial Distribution

Temperature control methods under consideration include the control or management of the PMBP temperature by monitoring and controlling each bay under each PMSA. If these are controlled independently of each other, then they can be at random phase with each other as they oscillate over a small range of ±0.5 mK. This effect was evaluated using the LUVOIR wing model and applying temperature transients to each bay that are phased randomly relative to each other. The analysis included four groups that include 10 set of temperature cases, each with a different random phase map. The groups include sets that allowed for 0.25 π, 0.50 π, 0.75 π and 1.00 π range of relative phasing. **Figure 42** shows examples of two temperature distribution cases for the 1.00 π bandwidth random cases.

The results of this analysis are gathered in **Table 19** and can be compared to the uniform temperature results previously discussed in **Table 18**. The results show the system will be better served by a coherent spatial control approach across the full PMBP aperture rather than localized control zones that operate independent of each other.
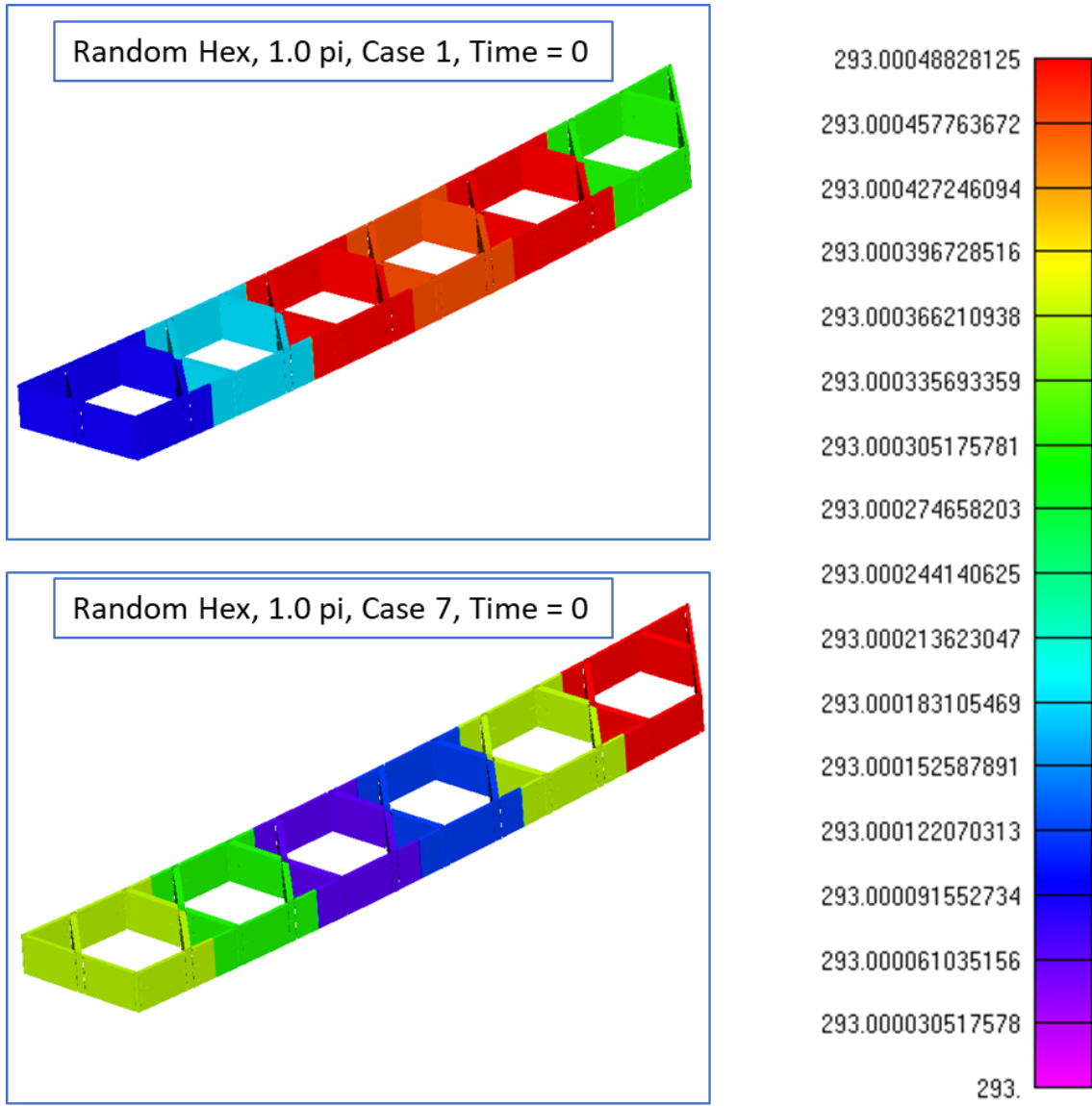
Figure 42: Two samples of random temperature phasing between mirror segment bays in the LUVOIR Wing Model. Each bay oscillates ±0.5 mK at 4 Hz with random phase assignments to each bay (maximum phasing range =1.00 π) .

Table 19: Variation in PMSA Pose Stability Sensitivities associated with PMBP Temperature Control Approach.

| Case	Statistic	Apparent Bulk Temperature Change (mK)	Despace Sensitivity (m/ppm strain)	V3 Shear Sensitivity (m/ppm strain)	R2 Tilt Sensitivity (rad/ppm strain)	R3 Tilt Sensitivity (rad/ppm strain)
1/4 Pi	Max	0.99	2.79	19.60	6.95	2.05
	Mean	0.98	1.20	8.64	2.18	0.81
	Min	0.96	0.29	6.17	0.71	0.39
1/2 Pi	Max	0.95	84.45	262.44	104.88	35.60
	Mean	0.90	19.02	61.70	20.05	7.73
	Min	0.81	1.53	12.53	2.61	0.80
3/4 Pi	Max	0.96	68.81	362.80	76.94	59.93
	Mean	0.84	16.84	69.26	16.00	9.90
	Min	0.69	0.64	7.24	1.47	0.75
Pi	Max	0.88	40.85	109.89	36.49	16.44
	Mean	0.71	10.11	44.56	12.13	5.51
	Min	0.40	1.90	12.99	2.53	1.30

Note: Unit strain is interpreted as $\epsilon = \alpha \Delta T$. The temperature refers to bulk change of the PMBP and the CTE is the bulk average CTE in ppm/K of the PMBP. Applying these sensitivities can use any values of choice.

9.3.4 Composite Design and Manufacturing to Meet Desired CTE

The material design for the PMBP is driven by two primary effects. Dynamic stability urges for higher structural stiffness and leads to the need for high elastic modulus and low structural areal density. The PMBP also provides dimensional stability while thermal environment fluctuates within the temporal control limits. This needed passive resistance or accommodation of the environment drives the need for a low CTE structure.

Balancing stiffness and thermal stability are a common endeavor on space telescopes. A truly zero CTE must be associated with a level of precision. The Webb Telescope dealt with the same challenge, though on a different scale, and can serve as an informing reference point. The allocation to PM Figure – Backplane in the MF temporal band is 10 pm-rms and the nominal PMBP temperature control in that temporal domain is targeted at 1 mK. The ratio of these two leads to a sensitivity of 10 nm-rms/K. The Webb PMBP sensitivity per the error budget and environmental design space was 127 nm-rms/K. This suggests that LUVOIR may need material property controls that are on order of 10x tighter than Webb (without active WFSC).

The Webb PMBP component manufacturing data shown in **Figure 43** suggests that material CTE controls on order of $\pm10^{-9}$ strain/K will be required for LUVOIR. The data also shows that some of the manufactured elements from Webb would have been acceptable for LUVOIR, but a clear majority would have been rejected. Furthermore, the ability to measure with enough confidence that an element is actually "inside" the acceptance space cannot be accomplished with the same methods used for Webb.
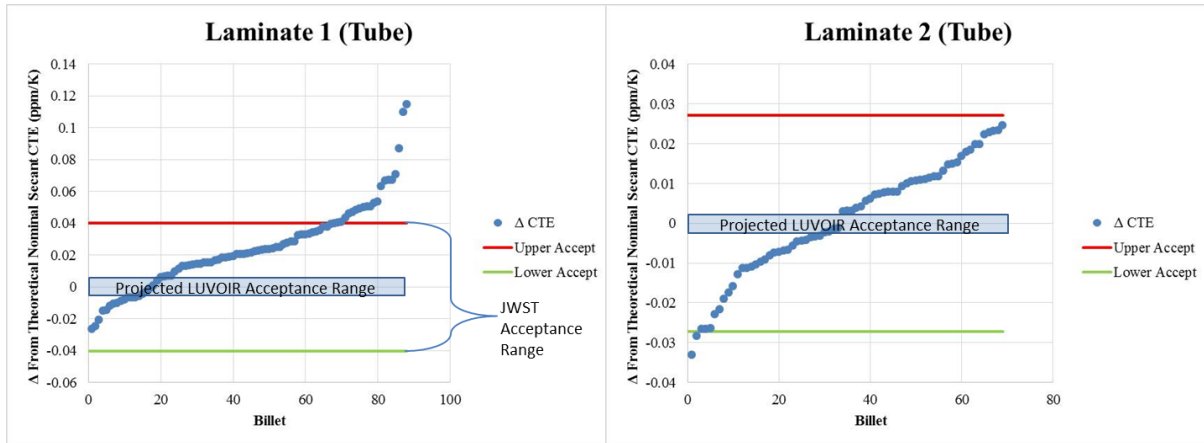
Figure 43: Data from Webb shows that parts can be produced to the required controls for LUVOIR. Manufacturing initiatives to reduce the scrap rate is recommended.

9.3.5 Joint Fitting CTE

On the PMBSS, the components with a significant impact on overall CTE stability are the fittings. For some fittings, such as the spacecraft interface, the high CTE does not significantly impact the performance of the structure. However, the Invar fittings closer to or at the optical interface do have a significant impact on the performance. One possibility to reduce the influence of fitting CTE is to remove Invar from the design completely and use molded composite fittings. Given the 3-dimensional nature of these structures, it is likely that they would be made from a quasi-isotropic type layup.

To evaluate the impact of the fitting CTE on performance, two models were run at both 270K and 270.001K: the first with standard Invar fittings which have temperature dependent CTEs and the second with all the backplane center section fittings converted to a temperature dependent quasi-isotropic CTE. The influence of the fitting CTEs was calculated by taking the difference in the performance predictions between the two models at the two temperatures. The final output of the models is a change in the PM Global and PMSA rigid body degrees of freedom (PM Align and PM Figure – PMSA Align terms in the stability budget). For the materials and conditions described above, the resulting rigid body motions are compared to stability budget-derived rigid body allocations in **Figure 44**.

Frequency Band	Source	PM Global Alignment Expectations						PM Figure (PMSA) Alignment Expectations					
		V1 (nm)	V2 (nm)	V3 (nm)	Clocking rV1	TiltrV2	TiltrV3	V1 (nm)	V2 (nm)	V3 (nm)	Clocking rV1	TiltrV2	TiltrV3
LF1	Allocation	2E+03	8E+03	8E+03	3E+05	1E+03	1E+03	9E+02	7E+02	2E+02	9E+05	4E+02	4E+02
	CS Joint Fitting CTE	4E+03	6E+01	1E+03	1E+02	2E+03	6E+01	1E+04	7E+04	8E+04	3E+03	2E+04	1E+04
MF	Allocation	5E-02	2E-01	2E-01	7E+00	3E-02	3E-02	2E-01	2E+00	5E-02	2E+02	9E-02	9E-02
	CS Joint Fitting CTE	1E-01	3E-03	7E-03	1E-03	3E-02	8E-03	2E-01	7E-02	9E-02	4E-02	1E-01	1E-01

LEGEND

(red)	System definition and/or technology advancement needed to achieve order of magnitude reduction of expected performance influence.
(yellow)	Significantly more and new engineering challenges than JWST to achieve affordability within error budget
(green)	Manageable within error budget with JWST SOTA technology and engineering methods.
(white)	Relatively inconsequential influence to afford in error budget.

Figure 44: Top: Comparison of expected and allocated rigid body motion of PM components due to fitting CTE. Bottom: Color code legend.

Given the non-compliance in some DOFs, there will need to be some engineering improvement beyond the current SOTA. Composite molded fittings are one option, with examples available across the composites industry. However, their use in stable optical structures has been limited. Some development effort will need to be spent to ensure that these components can produce predictable and repeatable stability performance over the thermal environment of LUVOIR.

Correction for Updated Stability Budget: The LF1-PM Align and LF1-PMSA Align allocations are reduced by an order of magnitude in the updated stability budget, thus increasing the non-compliance for fitting CTE in that row. The MF-PM Align and MF-PMSA Align allocations are on the same order of magnitude in the updated stability budget, so the compliance of that row is unchanged.

9.3.6 Adhesive CTE

The influence of the adhesive CTEs was assessed in a similar manner to the fitting CTE – two models were run, one with the as-built adhesive CTEs in the PMBSS and a second with the CTEs set to zero, and the results were subtracted. Once again, the stability requirements were evaluated between 270K and 270.001K. The final output of the models is a change in the PM Global and PMSA rigid body degrees of freedom (PM Align and PM Figure – PMSA Align terms in the stability budget). For the materials and conditions described above, the resulting rigid body motions are compared to stability budget-derived rigid body allocations in **Figure 45**.

Frequency Band	Source	PM Global Alignment Expectations						PM Figure (PMSA) Alignment Expectations					
		V1 (nm)	V2 (nm)	V3 (nm)	Clocking rV1	TiltrV2	TiltrV3	V1 (nm)	V2 (nm)	V3 (nm)	Clocking rV1	TiltrV2	TiltrV3
LF1	Allocation	2E+03	8E+03	8E+03	3E+05	1E+03	1E+03	9E+02	7E+02	2E+02	9E+05	4E+02	4E+02
	Adhesive CTE Influence	2E+03	1E+02	2E+03	1E+02	1E+03	1E+02	1E+04	2E+04	2E+04	6E+03	2E+04	2E+04
MF	Allocation	5E-02	2E-01	2E-01	7E+00	3E-02	3E-02	2E-01	2E+00	5E-02	2E+02	9E-02	9E-02
	Adhesive CTE Influence	4E-02	2E-03	3E-03	4E-03	8E-03	1E-03	3E-02	6E-02	7E-02	1E-02	4E-02	7E-02

Figure 45: Comparison of expected and allocated rigid body motion of PM components due to adhesive CTE. Same color legend as Figure 44.

While there is no adhesive with low enough CTE to match laminates, there are adhesives that have lower CTEs than those that were used on heritage programs to build space structures. Stated properties from the manufacturers indicate that they are capable of low outgassing for space environments, and they appear to have a reasonable ability to carry loads. Development testing would need to be carried out to ensure that the stiffness, strength, and CTE properties are understood well enough, as well as the techniques for using the adhesive during the manufacturing process. Because the adhesive is likely to still have a relatively high CTE when compared to the desired CTE levels, it will also be desirable to remove as much of the adhesive from the alignments path as possible. To do this, it is important to involve the structures team early in the design process to get the optimum alignment of interfaces and envelopes to minimize adhesives. It will also be important to have all interfaces defined early, along with their loads, so that the structure can be designed to accommodate those while not impacting the stability of the structure.

Using molded composite fittings can also help remove adhesive from the structure, or place it in less sensitive areas, by combining multiple structures that typically are created by bonding several components together and making a one-piece low CTE structure. Because of the development time and effort associated with these more complex structures, it would make sense to build a structure that is modular and allows the reuse of joints as often as possible.

Correction for Updated Stability Budget: The LF1-PM Align and LF1-PMSA Align allocations are reduced by an order of magnitude in the updated stability budget, thus increasing the non-compliance for fitting CTE in that row. The MF-PM Align and MF-PMSA Align allocations are on the same order of magnitude in the updated stability budget, so the compliance of that row is unchanged.

9.4   Moisture Desorption

A stable PMBP constructed of today's best composite options will have moisture dry-out effect. The moisture dry-out will cause the body to strain and change shape. The strain rate will decay exponentially according to a time dependent function during desorption. The 1-D solution for the temporal effect is estimated as follows:

$$\dot{\varepsilon}_m(t) = \beta_c D_{c,z} \frac{800 C_0}{\rho_c h^2} \sum_{n=1}^{\infty} -(2n+1)^2 \exp(-2n+1)^2 \frac{\pi^2}{h^2} D_{c,z} t) \qquad [13]$$

Where β_c is the laminate CME (strain/Δ%Moisture content); $D_{c,z}$ is the moisture diffusion coefficient in the composite in the thickness direction (cm^2/hr); C_0 is the initial uniform moisture concentration in the laminate (gm/cm^3); ρ_c is the composite dry density (gm/cm^3); h is the laminate thickness (cm); t is the dry out time after exposure to the vacuum of space (hours).

The moisture diffusion coefficient is also temperature dependent. The following model, which was suitably validated on Webb, is a reasonable estimate of the thermal dependency.

$$D_{c,z}(T) = 56.7 \exp\left(\frac{-4680.83}{T}\right) cm^2/hr \qquad [14]$$

The moisture effect must share budget with the temperature effect in the budget allocations for dimensional stability. It would be beneficial if the moisture effect could be small enough to consume 1% or less of the budget allocation. Then, the effect of moisture can be practically ignored during the initial phases of system architecture study and all budget can be allocated to temperature effects.

The stability under thermal perturbation already discussed suggests that CTE control on the order of 5 ppb/K and temperature control on the order of 2 mK will be a reasonable balance of challenge between material and system design spaces. This result is largely driven by the MF temporal domain (1-50 Hz). This suggests a bulk rate strain level on the order of 1×10^{-11} to 5×10^{-10} strain/sec over the bandwidth of the MF domain. Expansion rates of composites due to moisture concentration change are typically reported in hourly or daily rates. Converting the previous rates to hourly we get rates that range from 3.6×10^{-8} to 1.8×10^{-6} strain/hr. The precision in these calculations is beyond justification, but the order of magnitude is informative. This suggests that strain rates on order of 10^{-8}/hr are significant consumers of WFE budget allocation and strain rates of order of 10^{-10}/hr can be considered insignificant to the accounting. Furthermore, if a combination of design and operational concept can be struck that suggests the lower strain rate is achievable by practical and available means, then moisture can be removed or substantially reduced in the level of risk moving forward. **Figure 46** is a graphical depiction of this design space.
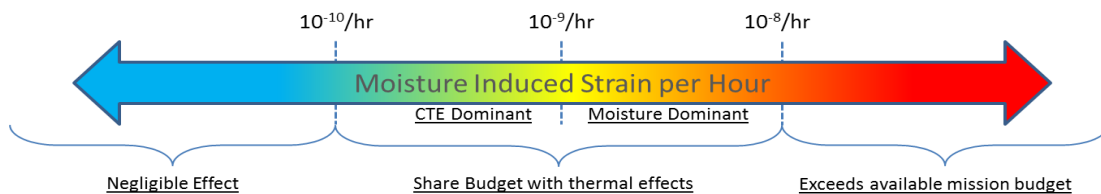
Figure 46: Seeking a design and operational solution that has strain rates less than 10^{-10}/hr can remove moisture effects from consideration as a significant consumer of WFE budget.

There are generally accepted methods for manipulating the moisture induced strains. This include manipulating the variables in the previous equations that move the strain rate in a desirable direction. The range of parametric evaluations and trade cases are listed in **Table 20**.

Table 20: Moisture mitigation trade cases

Trade Case	β_c (ppm/%ΔM_c)	Temperature (K)	Initial %M_c (%)	Thickness (mm)
Baseline[1]	130	293	0.2	
1	130	293	0.1	
2	65	293	0.1	0.1 to >4.0
3	Reduce $M_c\beta$ product by 10x at 293 K			
4	130	100 to 283	0.2	
5	Elevated Temperature Bake Out Effects			
[1.]Typical values for a quasi-isotropic M55J/cyanate ester laminate.				

9.4.1 Baseline Case

The mathematical model described previously was used to map the space of strain rate versus part thickness and dry out time. **Figure 47** shows the design space over practical part thicknesses. The results will be presented in similar fashion for each trade case. Note the header on each figure has the parameters that apply to the analysis (ex. T = 293K). Also, note the iso-lines are the $\log_{10}$ of strain rate.

Recall we are interested in iso-lines that are 10^{-8} and 10^{-10}. There exists some period of dry out time that will make all composites for all thicknesses dry enough that the moisture effect will fit within the stability budget allocation (-8 contour), but it will consume substantial budget until it approaches the -10 contour. In this analysis, it is assumed the LUVOIR mission can accommodate 100 days of dry out as the system on-orbit readiness and commissioning activities are underway.

The baseline results in **Figure 47** show that if all composite structures that have direct influence on PMBP dimensional stability can be constructed with thickness less than 1.6 mm, then moisture strain effects can be considered negligible. The Webb PMBP as mostly compliant with this metric, though not for this reason.
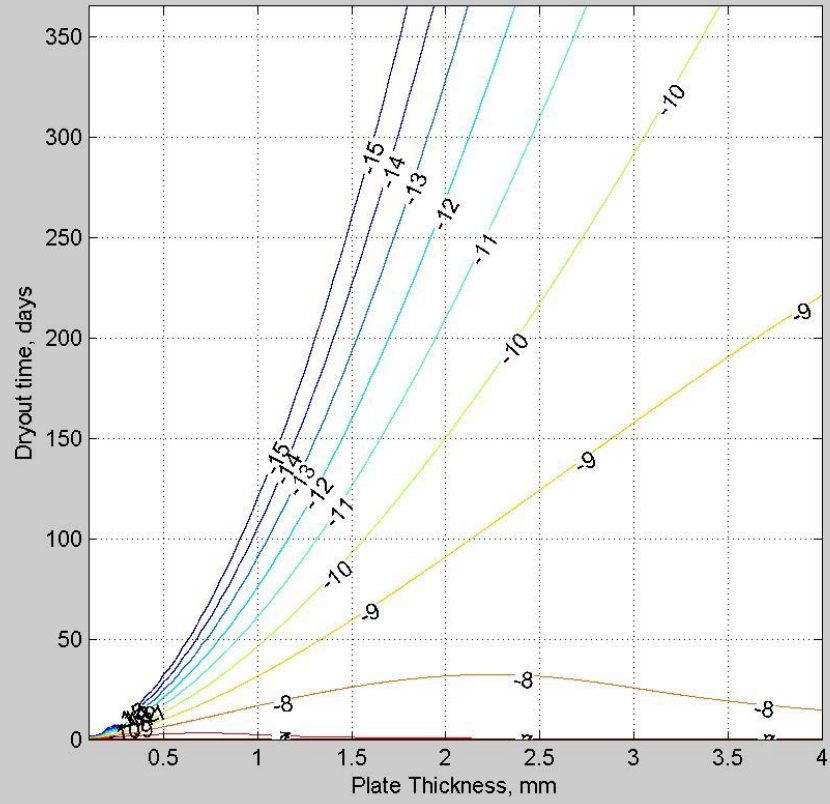
Figure 47: Baseline strain rate space.

9.4.2 Case 1 – Reduced initial moisture concentration

This case considers a reduction in initial moisture content. The intent here is to consider changing the matrix by using a different formulation like a cyanate siloxane or by adding fillers to the resin to reduce the moisture content, or even drying out the composite on the ground before launch. The assumed reduction is 50% and the results are shown in **Figure 48**.
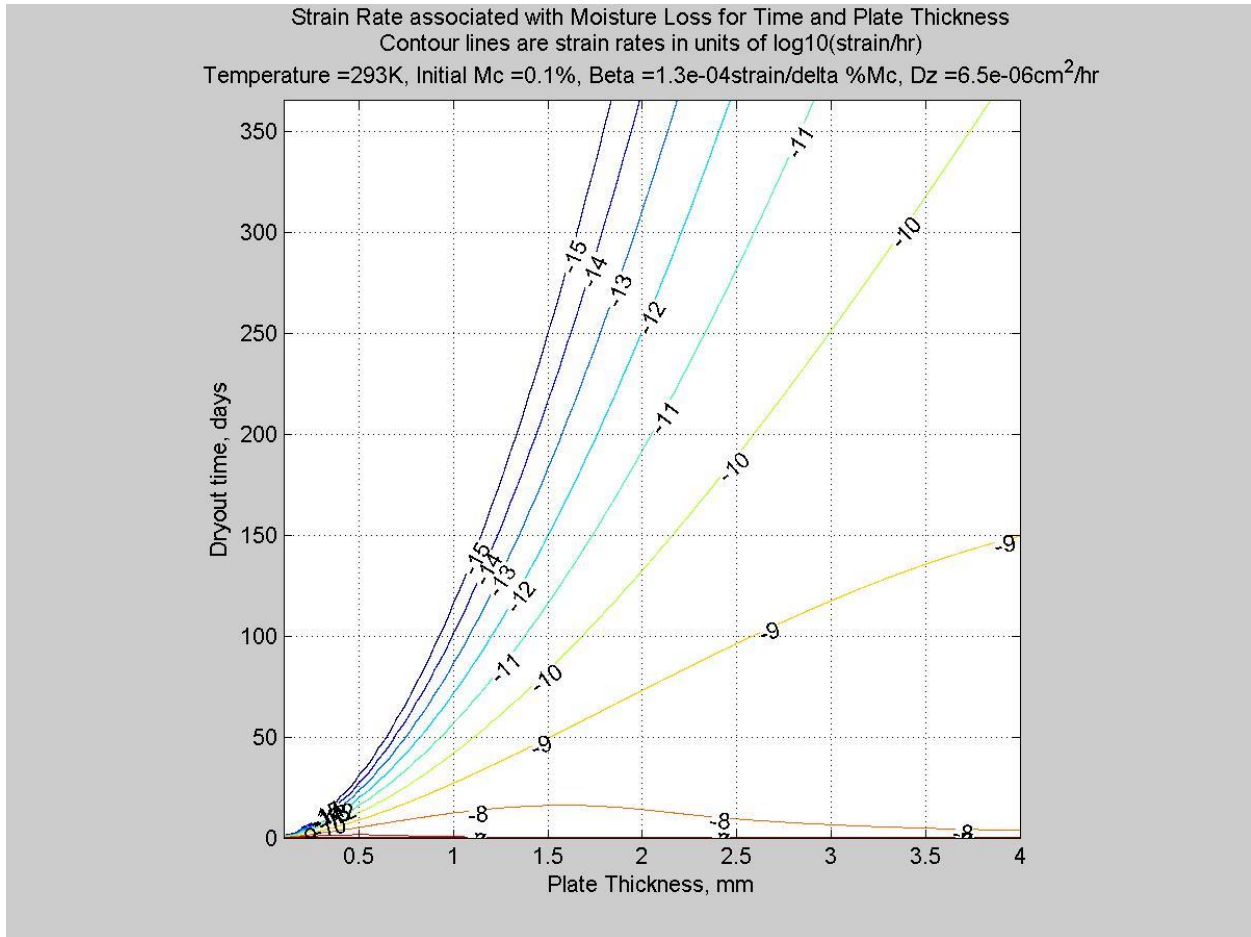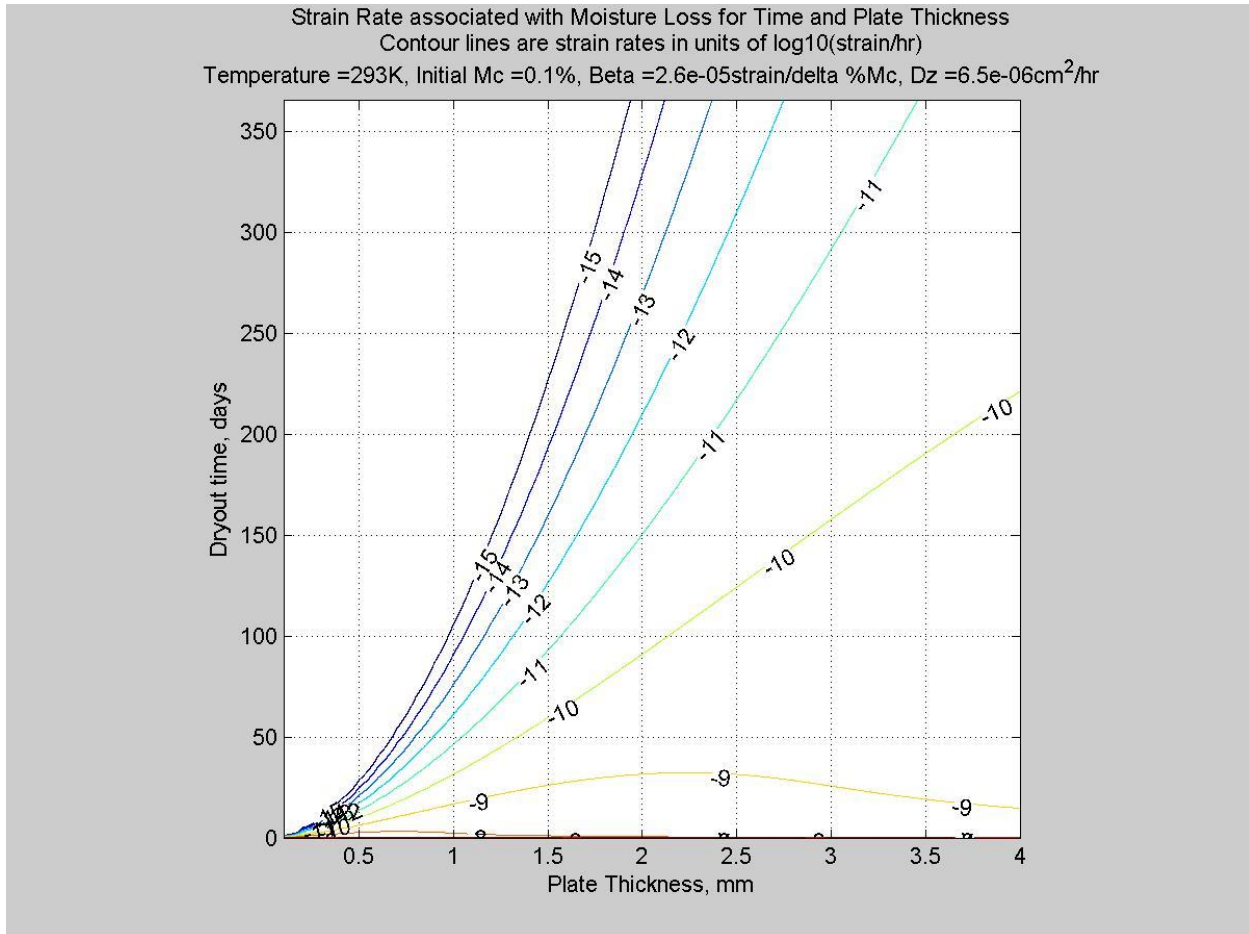

Figure 48: Case 1 evaluates the effects of reduced initial moisture content.

This result is interesting and not intuitive. The reduced initial condition does not substantially affect the strain rates at near dry conditions. The maximum target thickness, as identified by finding the intersection of the -10-contour line and the 100 day horizontal gridline, is increased to 1.7 mm compared to 1.6 mm in the baseline. This suggests the challenges and burdens of working to reduce initial moisture content have little return value.

9.4.3 Case 2 – Reduced Coefficient of Moisture Expansion (CME)

This study considers a 50% reduction in the CME. This might be achieved by redesigning the laminate, incorporating a filler in the matrix that assists the fibers in reducing the expansion/contraction of the matrix, or perhaps by other means yet to be identified. **Figure 49** shows the results.
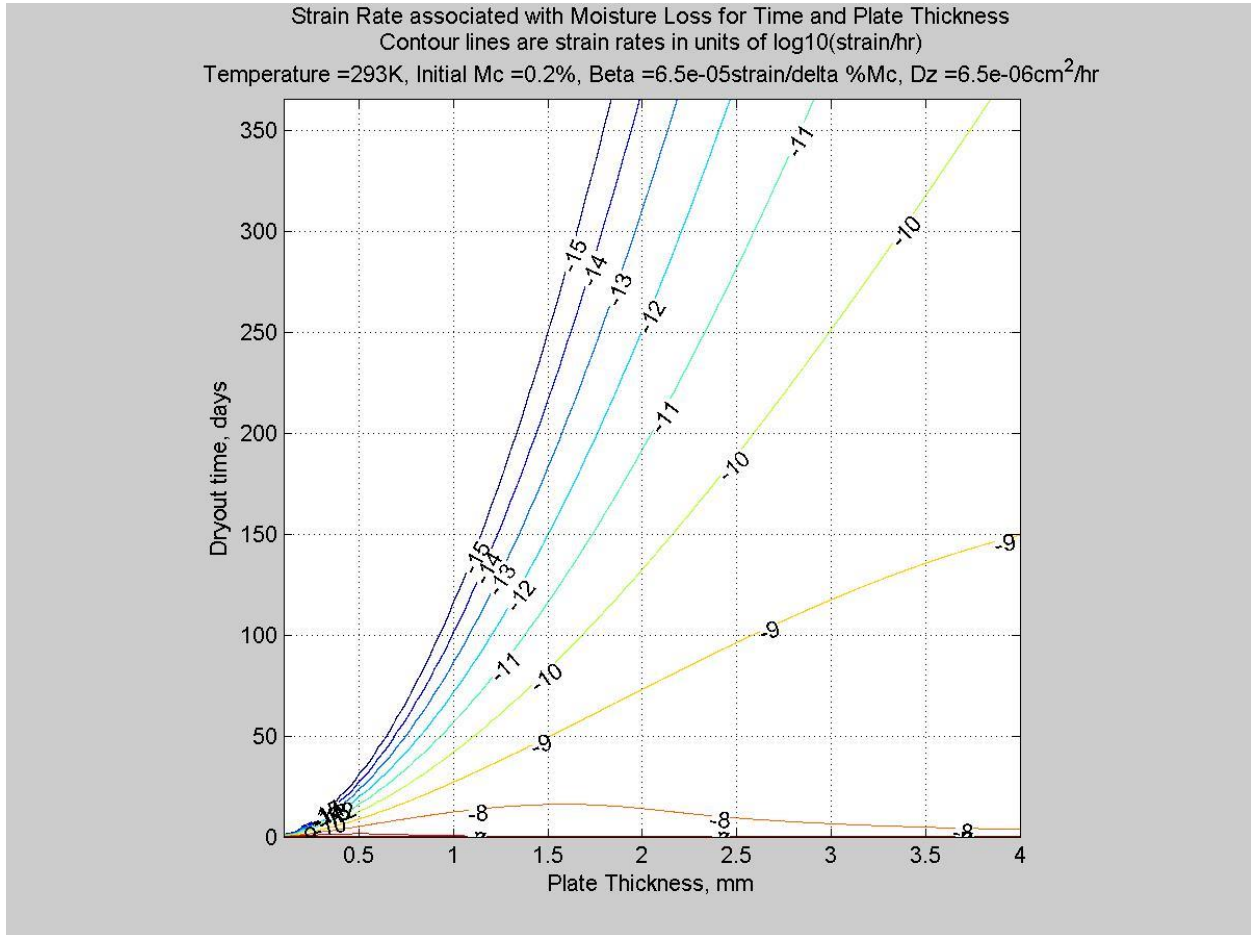

Figure 49: Case 2 evaluates the effects of reduced CME.

These results show an increase in the permitted wall thickness up to 2.2 mm. Gaining this capability could be a challenge as the competing needs of CTE, CME, stiffness and mass must be balanced in a manner that isn't necessarily available by example from previous programs. This could be an area of study in the future, but not necessarily an area that indicates a very high return on investment is available.

9.4.4 Case 3 – Reduce the product of initial moisture and CME by 10x

A method for accomplishing the material design isn't known at this time, but the exercise may prove informative. The results are shown in **Figure 50**.
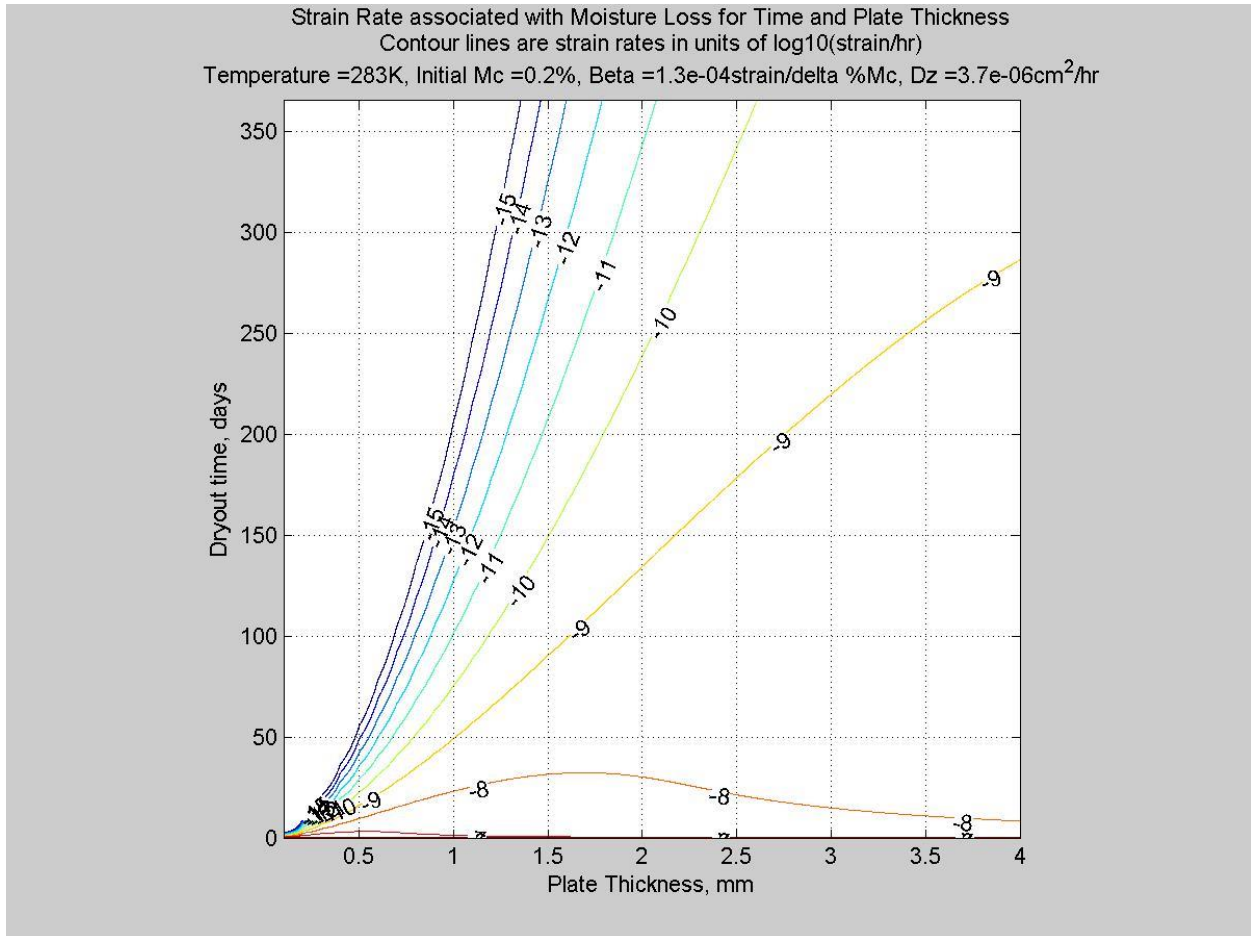

Figure 50: Case 3 evaluates the effects of a 10x reduction in the product of initial moisture concentration and CME.

The results show that a change of 10x in the product has minimal impact on the -10-contour line. This suggests that challenging the community to find very low CME articles is of limited value.

9.4.5 Case 4 – Operating temperatures down to 250 K

Mirror material choices motivate considering a colder operating temperature between 250 K and 283 K. The previous cases all considered an operating temperature of 293 K. This case evaluates the impact of colder temperatures on the strain rate change with time.

Figure 51 through **Figure 53** show results for operating temperatures of 283 K, 273K and 250 K respectively. These results show that the limiting thickness decreases with temperature over this range of consideration. The thickness at 283 K is 1.5 mm compared to 1.6 mm at 293 K. And thickness limits at 273 K and 250 K reduce to 0.8 mm and 0.5 mm respectively.

Figure 51: Case 4 evaluates the effects of a 283 K operating temperature.
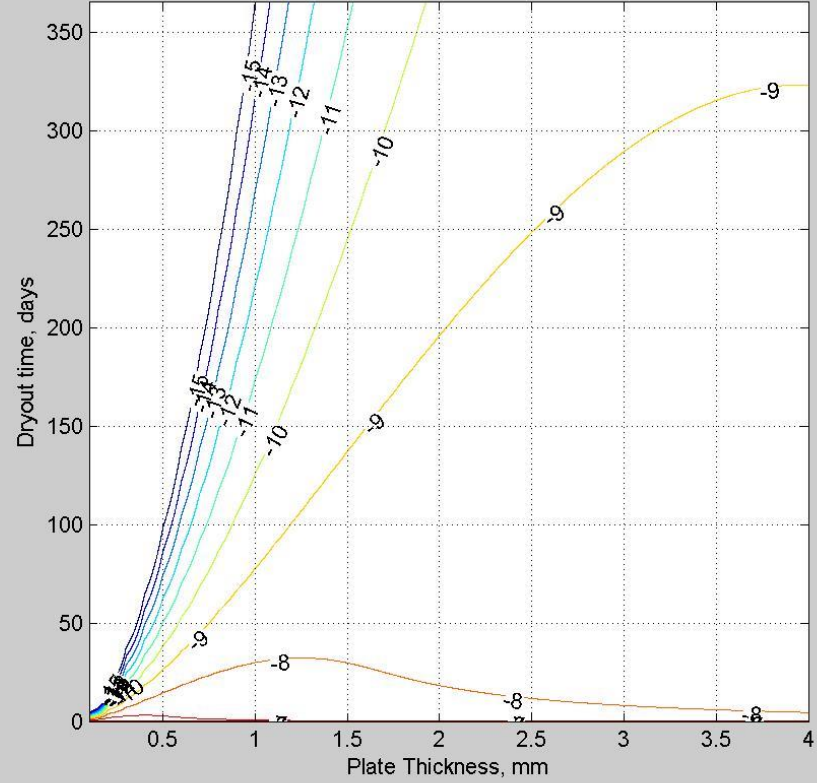
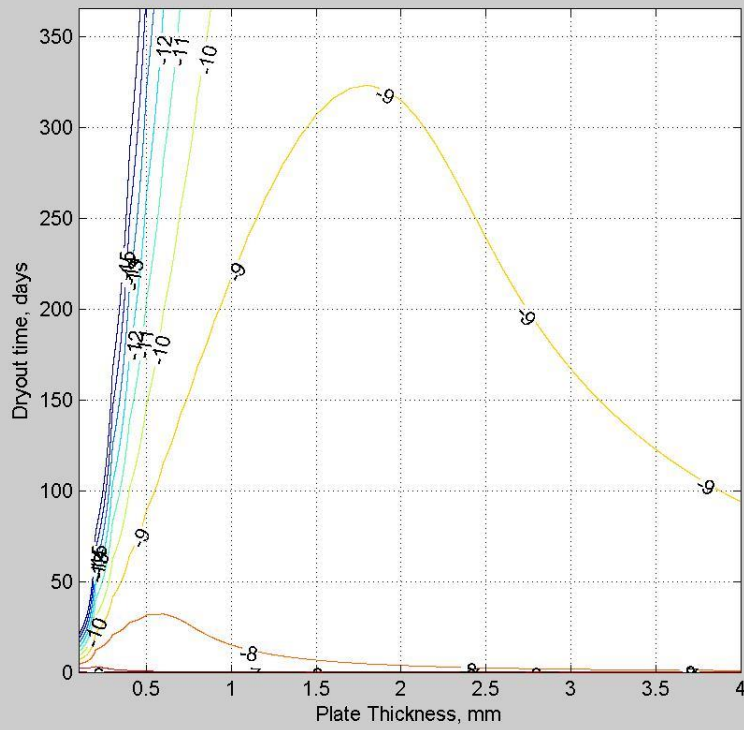**Figure 52: Case 4 evaluates the effects of a 273 K operating temperature.**

Figure 53: Case 4 evaluates the effects of a 250 K operating temperature.

9.4.6 Case 5 – On-orbit elevated temperature bake out

This study also considered performing an elevated temperature bake out on orbit during the 100 day dry out period to see if this affords a colder operating temperature without driving the design to very thin structural composites. The study considered dry out durations of 30, 60 and 90 days at 303 K and 313 K. The 30 day dry out at 303 K, shown in **Figure 54**, is enough to maintain a minimum thickness of 1.6 mm with an operating temperature to 250 K. Longer dry out times and/or higher dry out temperatures increase the permitted thickness.
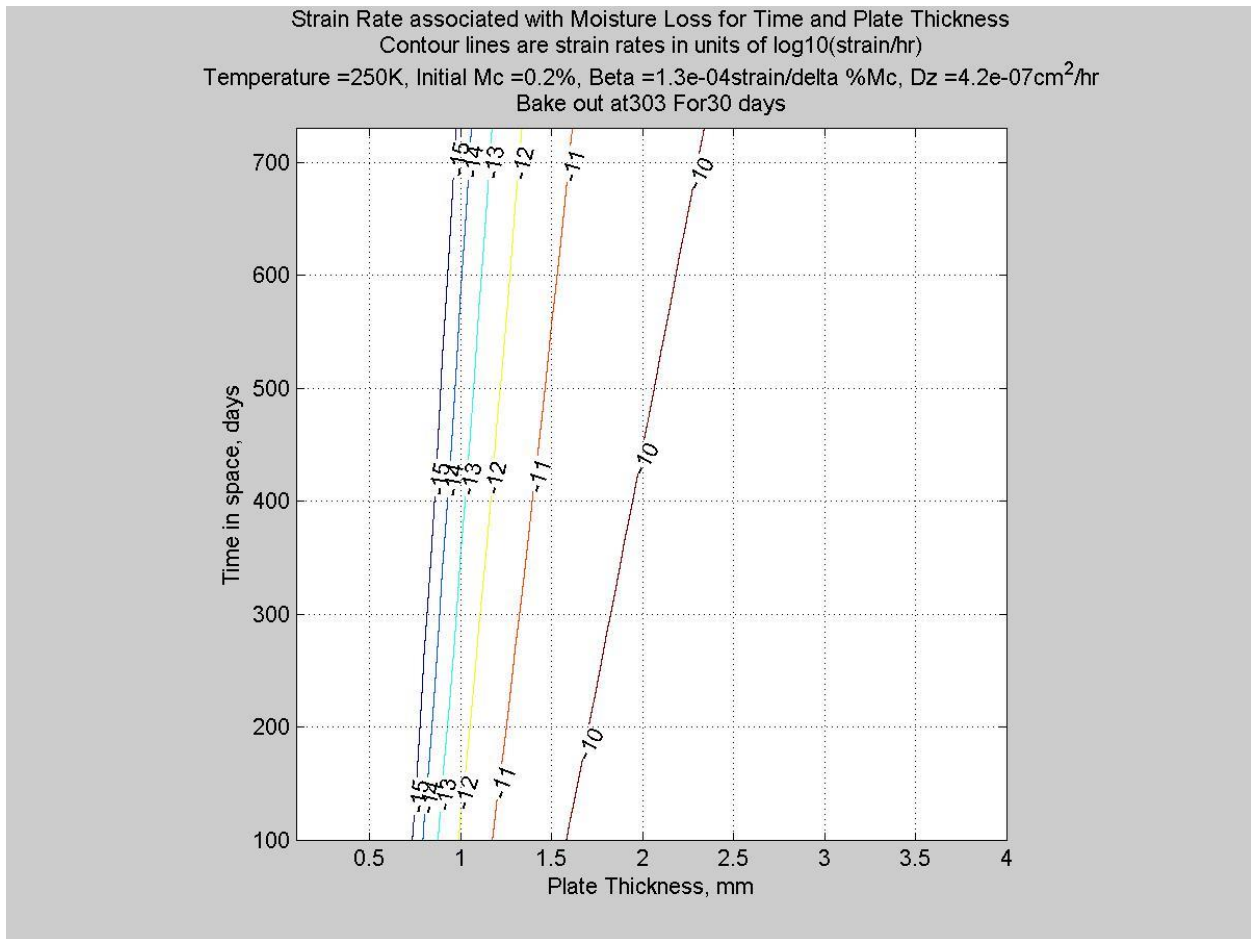
Figure 54: Case 5 evaluates 30 day dry out at 303 K and then operation at 250 K.

Correction for Updated Stability Budget: The allowable CME was chosen such that moisture desorption effects would be 1% or less of the thermal effects in the limiting MF band (see **Figure 46**). Since the MF allocation is slightly looser in the updated budget, the conclusions in this section do not change.

9.4.7 Additional Moisture Desorption Analysis

An independent moisture desorption analysis was performed using similar assumptions - an operating temperature of 270K and temperature control to within 1 mK up to the MF band. The timeline of operations from the manufacturing of the backplane to the end of life does not allow a definitive conclusion about exact moisture content at any point in its lifespan. However, it can be generally stated that moisture content will increase leading up to launch due to humidity in the air and lose moisture after launch due to the vacuum in space. Because the exact moisture loss cannot be quantified, the impact is bounded with conservative assumptions: that the part becomes fully saturated before launch, and loses all of the moisture by the end of its life span.

Given this assumption, the study team used classical lamination theory to develop the coefficient of moisture expansion for the laminates used in the Webb Primary Mirror Backplane Support Structure (PMBSS). Based on Tables 3.2-3 and 3.2-4 of EQ1-0158 Rev D, which describe the temperature and humidity of PMBSS during processing, transport, and encapsulation, and the assumption that a LUVOIR PMBSS could be in the worst humidity conditions for more than 6-8 weeks, testing data from Northrop Grumman shows that moisture content will reach a maximum of 0.18%. This value was added to a MAT9 card with the room temperature material properties, using a temperature change to model the moisture change. For reference, an example material card is shown below in **Figure 55**. This card is combined with a temperature change of -1 K to model the moisture loss.

MAT9* 5005000 667.511423E+07 280.408706E+07 280.408706E+07

* 121.834295E+09

* 384.355110E+08

* 121.834295E+09

* 284.413610E+07 416.993659E+08

* 284.413610E+07 1577.75 593.835953E-06

* 208.628852E-07 208.628852E-07

* 293.0

Figure 55: Example NASTRAN Material Card with CMEs replacing CTEs.

These material cards were then run in the Webb cooldown alignment thermal distortion model and scored using a verified scoring system. The output of the model is a change in the PM Global and PMSA rigid body degrees of freedom (PM Align and PM Figure – PMSA Align terms in the stability budget). For the materials and conditions described above, the resulting rigid body motions are compared to stability budget-derived rigid body allocations in **Figure 56**.

Frequency Band	Source	PM Global Alignment Expectations						PM Figure (PMSA) Alignment Expectations					
		V1 (nm)	V2 (nm)	V3 (nm)	Clocking rV1	TiltrV2	TiltrV3	V1 (nm)	V2 (nm)	V3 (nm)	Clocking rV1	TiltrV2	TiltrV3
LF1	Allocation	2E+03	8E+03	8E+03	3E+05	1E+03	1E+03	9E+02	7E+02	2E+02	9E+05	4E+02	4E+02
	Moisture Change (Dry Out)	1E+04	5E+02	2E+02	7E+02	3E+03	6E+01	2E+04	9E+04	1E+05	7E+03	4E+04	3E+04
MF	Allocation	5E-02	2E-01	2E-01	7E+00	3E-02	3E-02	2E-01	2E+00	5E-02	2E+02	9E-02	9E-02
	Moisture Change	Can be manageable at system level with sufficient wait time to reach a low enough rate of moisture content change.											

Figure 56: Comparison of expected and allocated rigid body motion of PM components due to moisture desorption. Red shading indicates effect exceeds allocation, green shading indicated effect can be controlled with SOTA techniques, no shading indicates a small effect on the stability budget.

This analysis shows there are some non-compliances due to the moisture desorption. At present, there are not any matrix systems with a lower absorption rate than the cyanate-ester assumed in this analysis. While metallic would fare better, they come with much higher CTEs that are detrimental to the overall performance of the structure.

One possible way around this issue is to keep everything dry until launch. Since this comes at the risk of ESD, methods for reducing that risk would need to be developed and implemented throughout the assembly process until launch. Another approach would be to predict the motion of the structure at each of the assembly steps, predict the motion of the interfaces due to the moisture content, and correct for that movement during the integration phases. This type of approach has been used in the past to correct for gravity sag, but the ability to predict deformations at any stage in the process to an acceptable level would need to be verified. A third option for resolving this non-compliance would be to increase the range of the actuators that can be used to align the optical components so that they are capable of correcting for this motion. Finally, an extended dry out period or on-orbit bakeout would result in lower moisture desorption rates early in the mission. Each one of these options has the possibility to overcome the moisture impacts on the structure, but each one will require some effort to develop with a sufficiently low risk to implement on this structure.

Correction for Updated Stability Budget: The LF1-PM Align and LF1-PMSA Align allocations are reduced by an order of magnitude in the updated stability budget, thus increasing the non-compliance for moisture desorption in that row. Mitigation strategies described can be used to regain compliance.

9.5 Dynamics

Dynamic inputs to the structure are primarily caused by on-board sources – spacecraft pointing, actuation of optical components, cooling and heating systems, etc. These occur at a variety of temporal frequencies and mitigation strategies exist at different bands. The impact of dynamics on the system stability is calculated using optical component motion and converting that to wavefront error.

One gap in this analysis is the impact of microdynamics or other nonlinear, impulse behaviors that are below the threshold of concern for nanometer wavefront stability but may become important for picometer wavefront stability (ex. micrometeoroid impacts, slip in bolted structures, etc.) These types of instability are inherently difficult to model as they are highly dependent on the exact surfaces, finishes, and forces under consideration. While investment in advanced modeling techniques may be warranted, measurements of structural stability at low strain magnitudes would be most useful in assessing the potential impacts.

9.5.1 Latch Force Variation

Because LUVOIR is expected to require a deployable backplane, there will need to be some type of latches present. The hardware involved in the latch plane interfaces on the Webb PMBSS had a significant impact on the alignment and stability predictions. Much of this impact had to do with the relatively high CTE items that were required to get the latch plane to function, including fittings and adhesive (discussed in Sections 9.3.5 and 9.3.6.)

For the dynamics assessment, an uncertainty in latch plane force retention force of ±80 N was used, which is derived from the expected Webb latch plane force variation over its lifetime. The assessment was made by running the model once with the nominal preload, and then running with preload variations over each of the latch plane interfaces. The RSS of the performance variations at all 8 latch locations was used to predict the final performance of the structure. A similar assessment was made for the short-term variations (MF band), with the latch force allowed to vary 0.25N at each location. The output of the model is a change in the PM Global and PMSA rigid body degrees of freedom (PM Align and PM Figure – PMSA Align terms in the stability budget). For the materials and conditions described above, the resulting rigid body motions are compared to stability budget-derived rigid body allocations in **Figure 57**.

Frequency Band	Source	PM Global Alignment Expectations						PM Figure (PMSA) Alignment Expectations					
		V1 (nm)	V2 (nm)	V3 (nm)	Clocking rV1	TiltrV2	TiltrV3	V1 (nm)	V2 (nm)	V3 (nm)	Clocking rV1	TiltrV2	TiltrV3
LF1	Allocation	2E+03	8E+03	8E+03	3E+05	1E+03	1E+03	9E+02	7E+02	2E+02	9E+05	4E+02	4E+02
	Latch Force Variability	4E+02	2E+02	1E+03	1E+04	5E+02	1E+03	7E+02	2E+03	9E+02	2E+03	1E+03	2E+03
MF	Allocation	5E-02	2E-01	2E-01	7E+00	3E-02	3E-02	2E-01	2E+00	5E-02	2E+02	9E-02	9E-02
	Latch Force Variability	2E-06	1E-06	2E-06	7E-07	7E-07	1E-06	4E-06	1E-06	2E-06	7E-07	3E-06	2E-06

Figure 57: Comparison of expected and allocated rigid body motion of PM components due to latch force variation. Green shading indicated effect can be controlled with SOTA techniques, no shading indicates a small effect on the stability budget.

The current design applies a force across the latch plane in between 2 sets of latch plane fittings. This introduces some moments into the structure that must be compensated for by stiffening the structure. Additionally, the structure is supported at 8 interface points across the latch plane, so any mismatch in the 2 planar surfaces must be overcome by increasing the latch force to close the gaps. This extra strain energy can lead to unwanted motion in the structure. The ideal approach

would be to develop a mechanism that requires no retention force across the latch plane. A low impact approach might be to apply the retention force directly through the interfacing structure so that they do not induce moment into the structure. Another area where performance could be improved here is to reduce the number of interface points to achieve a more kinematic interface. This should lead to less uncertainty about where the structure is, and the elimination of the need to close gaps should reduce the distortions induced in the structure.

Correction for Updated Stability Budget: The LF1-PM Align and LF1-PMSA Align allocations are reduced by an order of magnitude in the updated stability budget, so some DOFs may become non-compliant.

9.5.2 Dynamic Input Limits

The objective of this analysis is to estimate disturbance energy levels that will seem large relative to the WFE budget allocations to dynamic effects. This study addresses only the MF and HF temporal domains. Evaluation of the LF1, LF2 and LF3 domains requires some assumptions about the static stiffness of the PMBP and is beyond the scope of this evaluation currently. This study used a model of the Webb Optical Telescope Element (OTE). The Center of Curvature (CoC) dynamic test model of the OTE was used in this analysis. The end of this section will discuss scaling to LUVOIR from these results. The analysis path is outlined in the following steps:

- Use the Webb OTE model applied to the Center of Curvature Testing
- Apply controlled displacement disturbance in V1, V2 and V3 at DTA/BSF interface
- Generate relevant transfer functions
- Estimate maximum input energy levels
- Show how to scale from Webb to LUVOIR by system mass

The analysis method is a Modal Response Analysis with controlled input of 1 μm singularly in each of V1, V2 and V3 directions. Results were requested at 1 Hz to 100 Hz by 1 Hz increment. The requested data at each frequency included:

- Resisting force in direction of displacement at input – inertial effect of OTIS,
- DOF surface average motion of each PMSA
- 6 DOF PMBSS/PMSA interface plane average motion at each PMSA
- 6 DOF PM surface average motion
- 6 component PMSA Kinetic Energy

These results were then used to calculate transfer functions as shown in **Figure 58**. These are akin to sensitivities but are complex values. Sensitivities will be taken as the Gain or magnitude of these complex values. Setting the output to the budget allocation limit and going backwards through the control path estimates the maximum energy input the system can accept without exceeding the allocation.

Transfer functions of four types are calculated. PM surface motions refer to the PM global alignment budget and is the correlated motion of all 18 segments in the Webb model. Segment Total Motion is the observed motion of the segment which is the net effect of combined dynamic response of the PMSA and the BP. BP local motions are the part of the Segment total motion that

is attributable to the BP. Segment internal motion is the content associated with the PMSA dynamics.
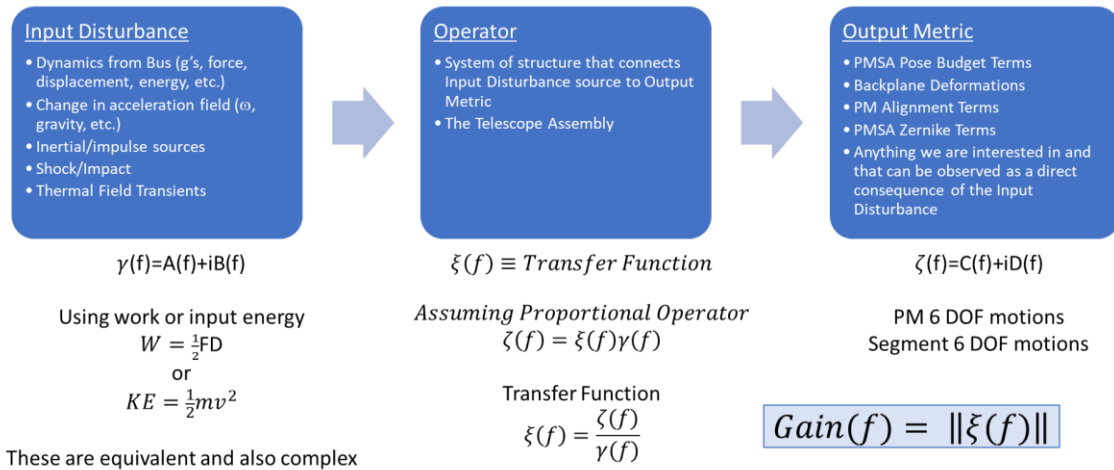

Figure 58: Definition of transfer function for dynamic energy bounding analysis.

The maximum energy limits for each of the three disturbance cases are shown in **Figure 59, Figure 60,** and **Figure 61**. The analysis calculated the energy level limit for each of the 18 PMSA across the frequency band of the analysis. Then, the minimum value in each frequency bin for each DOF was identified.
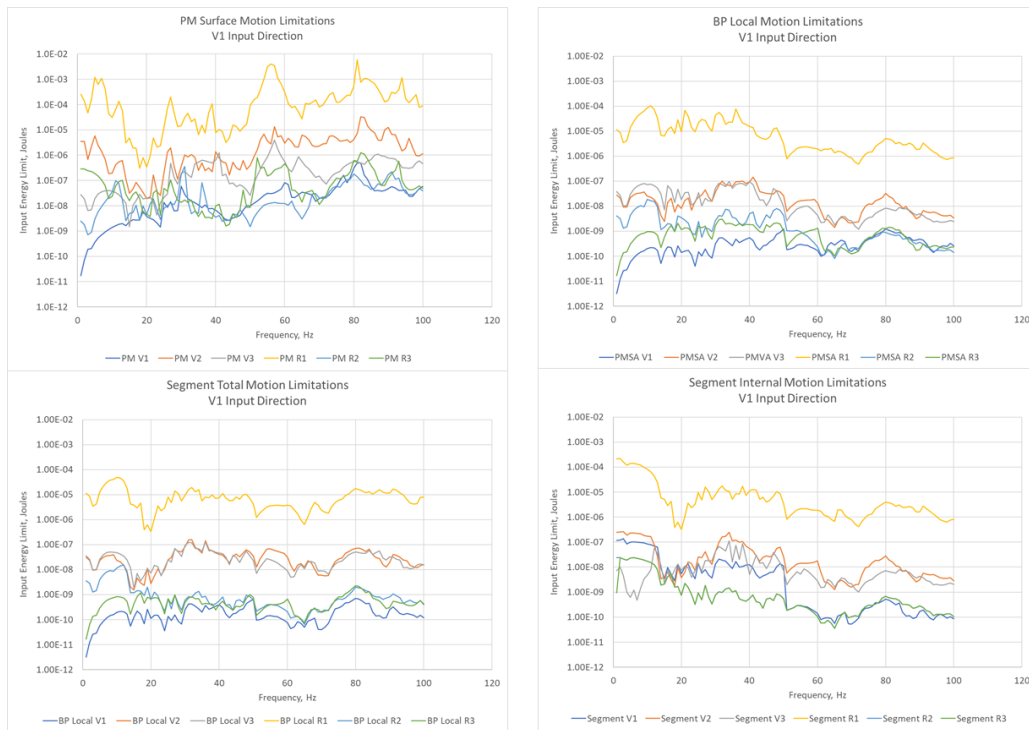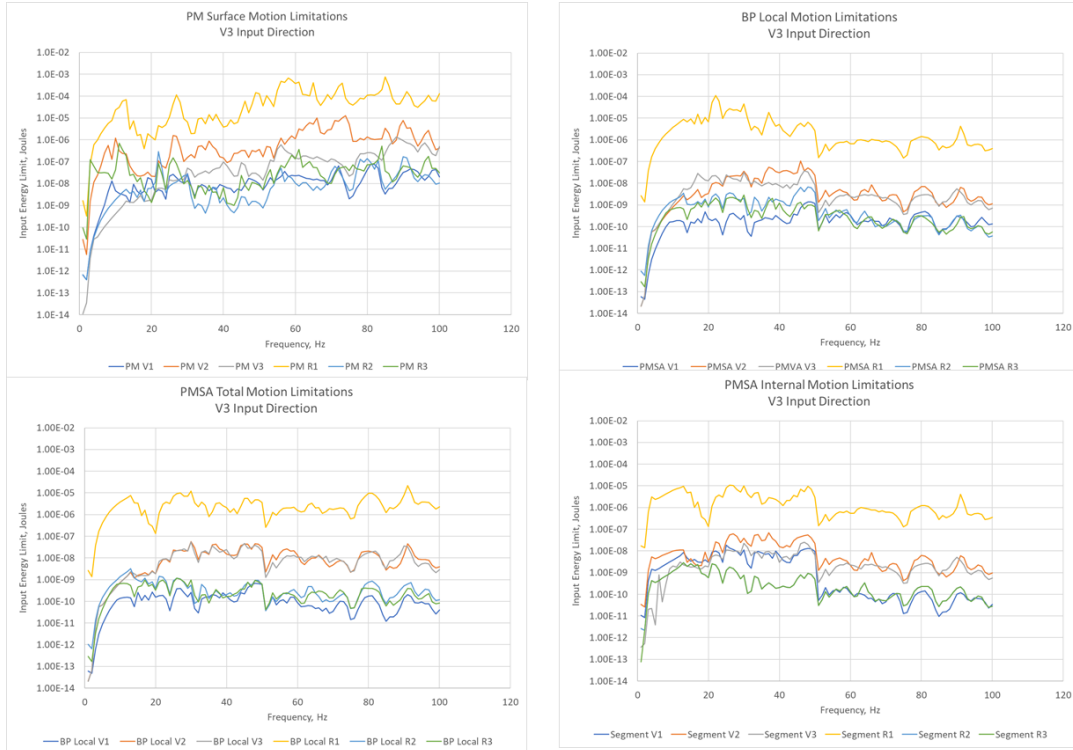

Figure 59: Maximum Energy Limits for V1 Disturbance.

**Figure 60: Maximum Energy Limits for V2 disturbance.**

Figure 61: Maximum Energy Limits for V3 disturbance.

The amount of information available here is tremendous. The main takeaways include:

- PM Global Alignment can accommodate nearly 100x more energy than PMSA Pose.
- PMSA Pose budget allocations can tolerate peak input energy on the order of 100 pJ and are usually limited by either despace or one of the two tilts.
- There is not a significant distinction between input directions suggesting that total energy is reasonable metric.

The results from this analysis can be scaled to LUVOIR or other systems that will have similarly arranged mirror segments on a large backplane. The recommended scaling method is by inertial mass. The inertial mass is the apparent or dynamic mass of the system that includes the inertial and other dynamic effects. **Figure 62** shows the ratio of inertial mass to static mass of the Webb model. The inertial mass for LUVOIR will depend on the architecture, but it will likely resemble the trends in **Figure 62**. Therefore, it is recommended the results be scaled according to the expected mass on the "quiet" side of the LUVOIR system.
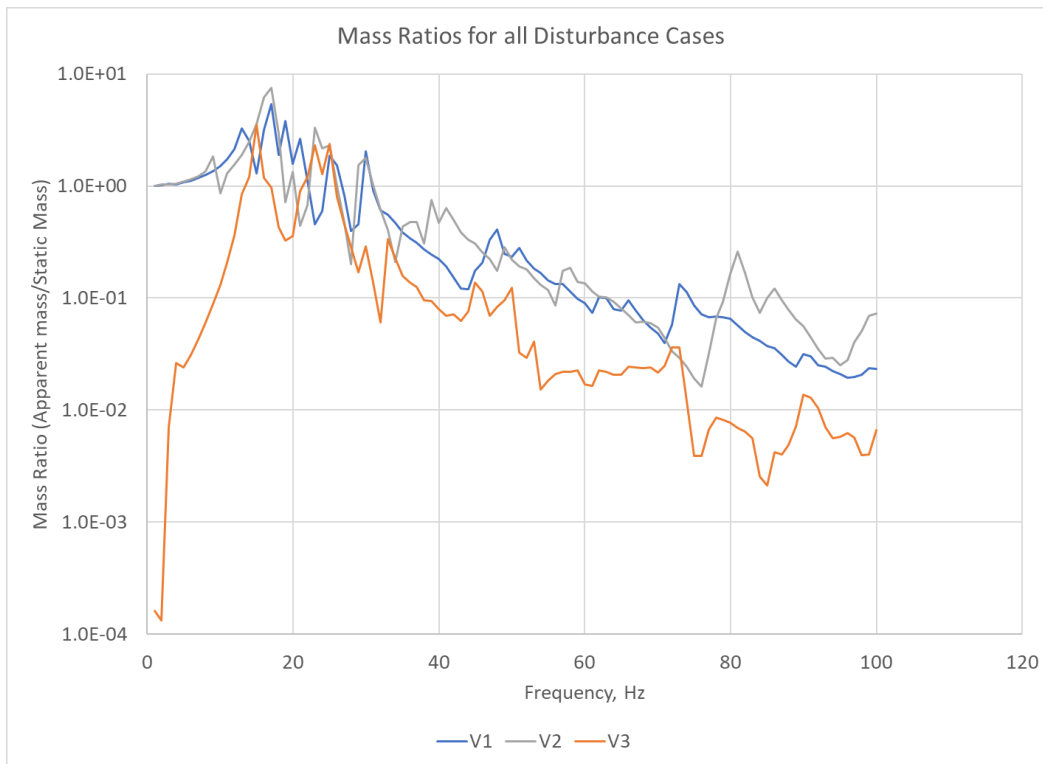
Figure 62: Mass Ratio of Webb analysis cases.

Correction for Updated Stability Budget: The LF1 allocations are reduced by an order of magnitude in the updated stability budget, so the allowable disturbances below 0.001 Hz will also be reduced. It is not expected that there is significant dynamics perturbation at that slow of timescale, but appendage modes may be affected.

9.6 Structural Sub-System Technology Gap Assessment

The following list presents a summary of the analysis areas studied and the technology gap classification. There are no low-TRL technology gaps identified in the area of Stable Structures, but there is a mid-TRL gap to evaluate the stability of hinges/latches to microdynamics. Also, significant engineering work will be required to meet the demanding structural performance in a timely and cost-effective manner.

| Structural Gap	Classification	Rationale
Stable Composite Structures - Manufacturing	No Gap	o Composite engineering, design and manufacturing technology level is of sufficient means to produce a credible PMBP design for LUVOIR. o Manufacturing methods for Webb-like precision composites need improvements to reduce scrap rates that would likely occur if LUVOIR were fabricated today. This is a cost savings measure and will require some engineering effort to accomplish.
Thermal Strain Measurement	Engineering Gap	o Required thermal strain measurement uncertainty $< 10^{-10}$ o Need systems that can evaluate thermal strains at part-per-trillion (ppt) resolution over mK disturbances at a pace that supports production rate needs.
Moisture Strain Measurement	Engineering Gap	o Required moisture strain measured uncertainty $< 10^{-11}$/hr o Need systems that can evaluate thermal strains at part-per-trillion (ppt) resolution in dry conditions after ~100 day bake out. o Moisture strain effects can be nullified in WFE budget allocations by paying attention to part thickness, allowing a dry out period on orbit and including a modest 10 K elevated temperature bake out for 30 days or more on orbit.
Temperature Control System Spatial Uniformity	Engineering Gap	o Analysis shows coordination of temperature control on backplane rather than isolated-PMSA control results in lower CTE requirements on structural materials.

Low CTE Joint Fittings and Adhesives	Engineering Gap	o Investigate replicated joint fitting designs, closed molded and/or additive manufactured composites. o Identify and qualify low CTE adhesive candidates.
Microdynamics and Low Energy Propagation	Knowledge Gap	o Need techniques for modeling and measuring low energy (<100pJ) disturbances to understand propagation through complex structures. o Need techniques for measuring the component response to microdynamics without altering the article dynamics with the sensing metrology – strongly recommend non-contact measurement techniques to keep uncertainty low.
Stable Hinges/Latches	Mid-TRL	o Characterize stability of hinges/latches or other structural joining techniques in microdynamics regime. o Study possible use of kinematic interfaces, low preload and variability, force through contact point centers to mitigate.
Material Creep from Aging	Knowledge Gap	o Need to verify that materials aged for several years have creep rates that are less than 10^{-13}/hr so that moisture is dominant over creep.
Material swelling due to radiation exposure	Knowledge Gap	o Need to verify that radiation induced dimensional changes develop at rates that are less than 10^{-13}/hr so that moisture is dominant over swelling.

10 Stable Mirrors and Mirror Mounting

10.1 Analysis Summary

The work documented in this section supports the mirror and mirror mounting elements in the WFE budget. While wavefront error allocations have been given to all optical subsystems, this analysis focuses on the segmented primary mirror, which is the most complex and is expected to have the tightest requirements. The key areas of analysis and trade studies covered in this section are represented graphically in **Figure 63**.

Sensitivity analysis and error budgets at the mirror level demonstrate that, with mK thermal control, the required picometer level stability for LUVOIR can be achieved with a ULE® PMSA design. Substrate CTE uniformity and mount induced WFE are critical effects that merit further investigation. Continued development of thermal transient models and control concepts along with hardware demonstrations form a comprehensive approach to demonstrate feasibility of a pico-stable mirror system.
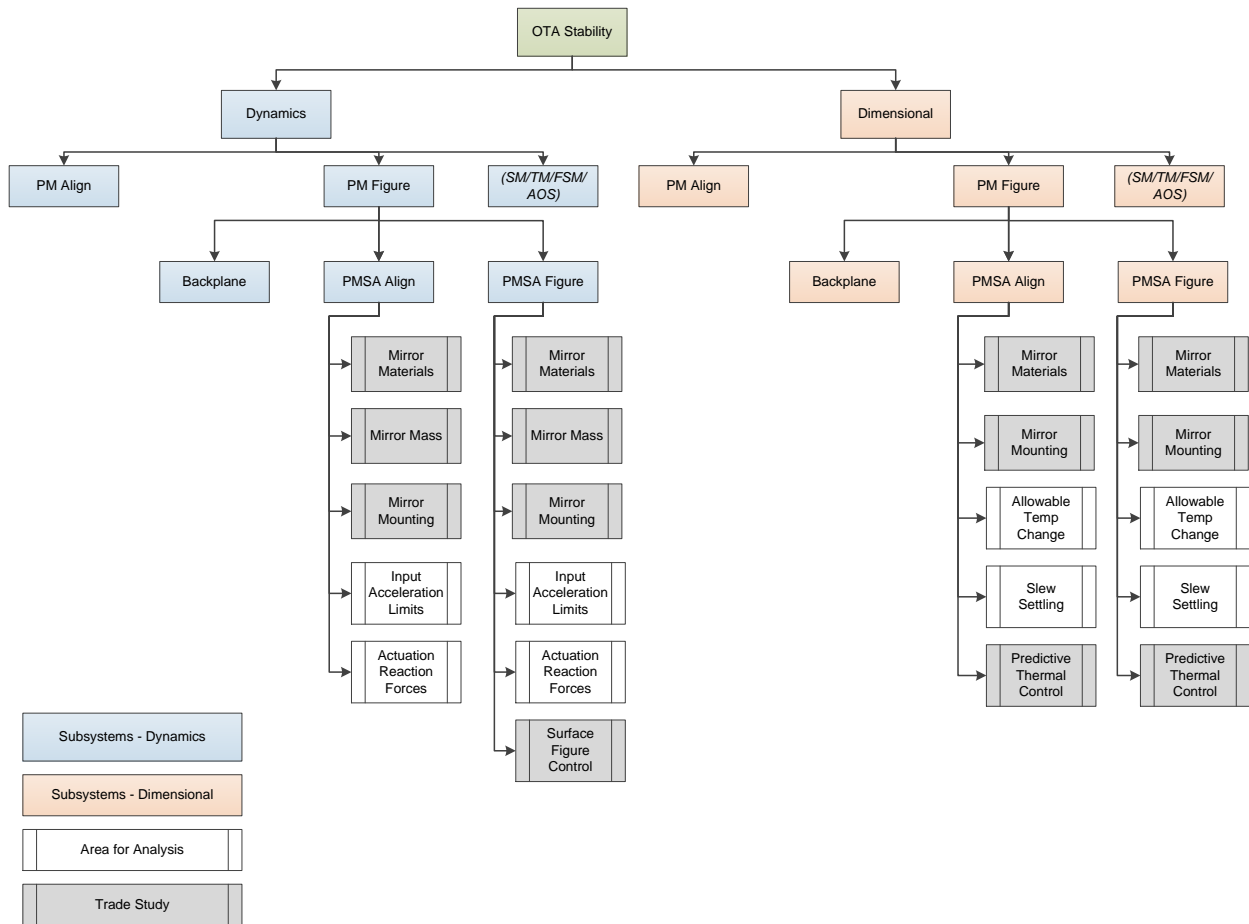

Figure 63: Stable Mirror and Mirror Mounting Analysis Summary – defines areas where analysis/trade studies were performed and maps them to the wavefront stability budget structure.

10.2 Modeling Summary

The diagram in **Figure 64** describes major structural components in the PMSA:

- Lightweight mirror substrate.
- Kinematic mirror struts and flexures connecting the mirror rigidly to a reaction structure.
- Kinematic rigid body actuators connecting the reaction structure to the PMBSS.

Not shown in **Figure 64** are the metrology features needed to align segments, cabling, thermal control hardware, structural interfaces and other details. **Figure 64** includes the entire load path between the PMBSS and the mirror substrate. The LUVOIR control concept includes the use of metrology features (capacitive edge sensors and laser metrology) that have not been included in this analysis. These features influence system stability, either by distorting the mirror itself or by not properly tracking the optical surface due to thermal distortion. Future analysis will address this interaction.
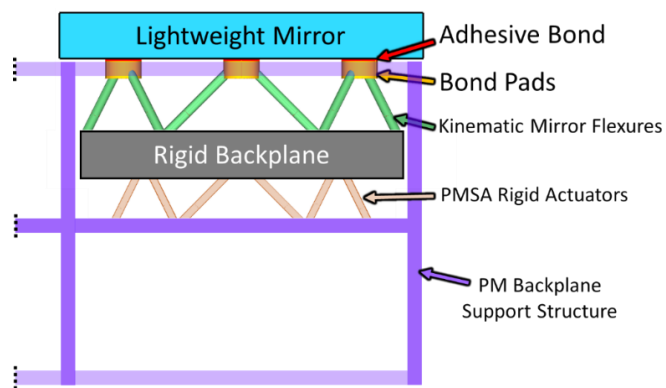
Figure 64: Notional Schematic of PMSA Baseline Design.
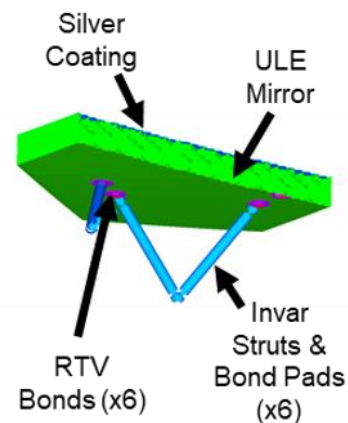
Figure 65: PMSA Finite Element Model for evaluating optical surface sensitivities to local effects.

Figure 65 illustrates the corresponding PMSA FEM which is used to evaluate optical surface sensitivities to stability effects local to the mirror (results in **Figure 66**). The FEM includes a ULE® closed-back construction mirror substrate, invar struts and bond pads, and adhesive bonds. The reaction structure is represented as infinitely rigid, which is an accurate assumption for many of the local effects analyzed, because it is substantially rigid as compared to the mirror flexures. While this FEM is extremely simple, it captures enough detail in the baseline PMSA design to provide rough order of magnitude estimates of optical sensitivities to various effects.

This model assumes:

- The thermal control of the system is ~1 mK
- An RTV adhesive bond is used to mount the mirror
- The composite reaction structure is sufficiently baked out or composed of thin enough members such that it has reached a steady enough hygroscopic state (see Section 9.4)
- Highly-tuned athermal flexures are used

80
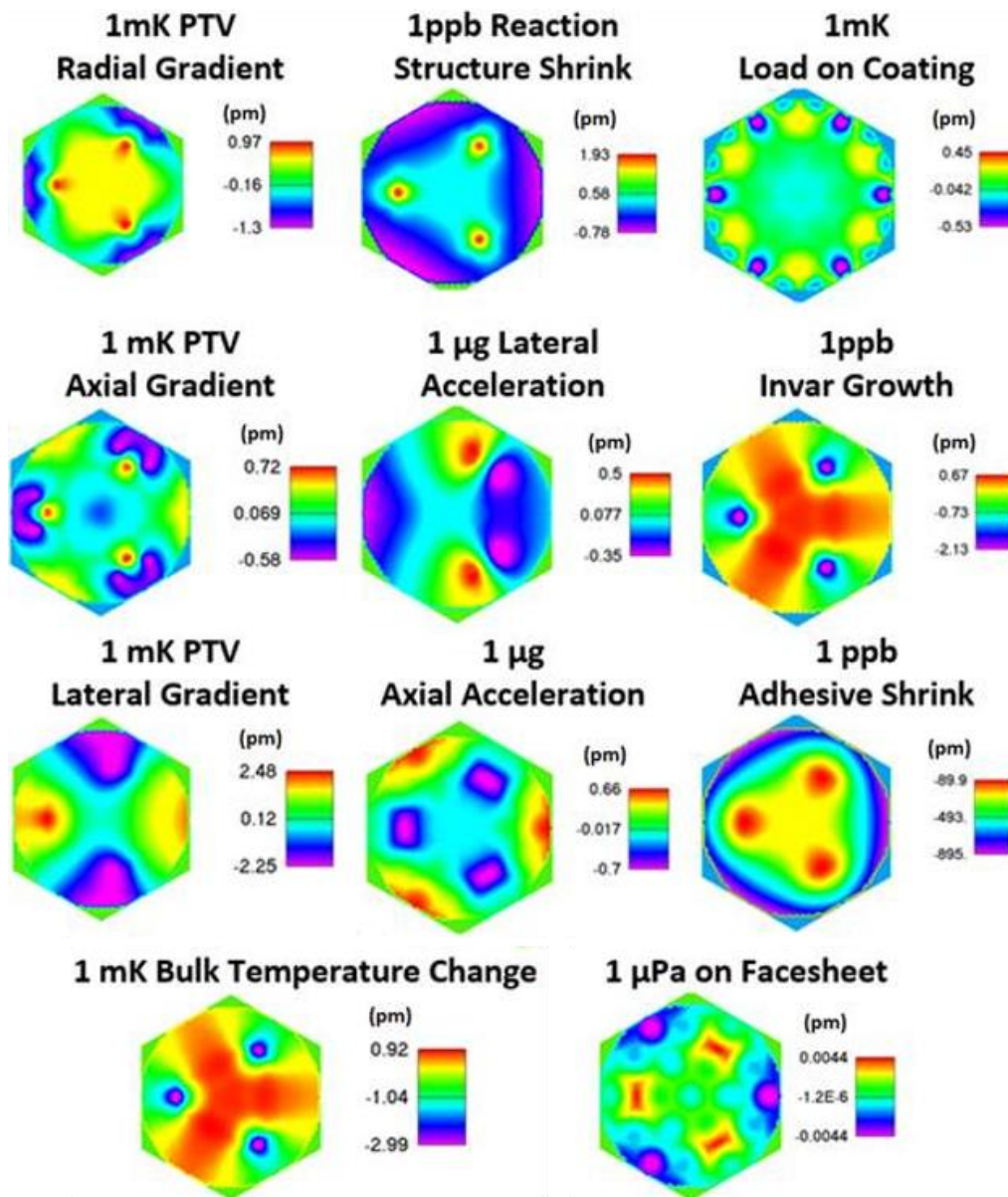
Figure 66: PMSA optical surface sensitivities to various loads.

For evaluation of thermal transients in the mirrors resulting from other parts of the observatory, the basic LUVOIR model was used to create the model in **Figure 67**. For the purposes of model and results simplification, only major thermal components are included. The DTA (Deployable Tower Assembly) and AOE (Aft Optics Enclosure) are assumed to be well-shielded from the PM and thus have been assumed to be at a fixed boundary temperature.
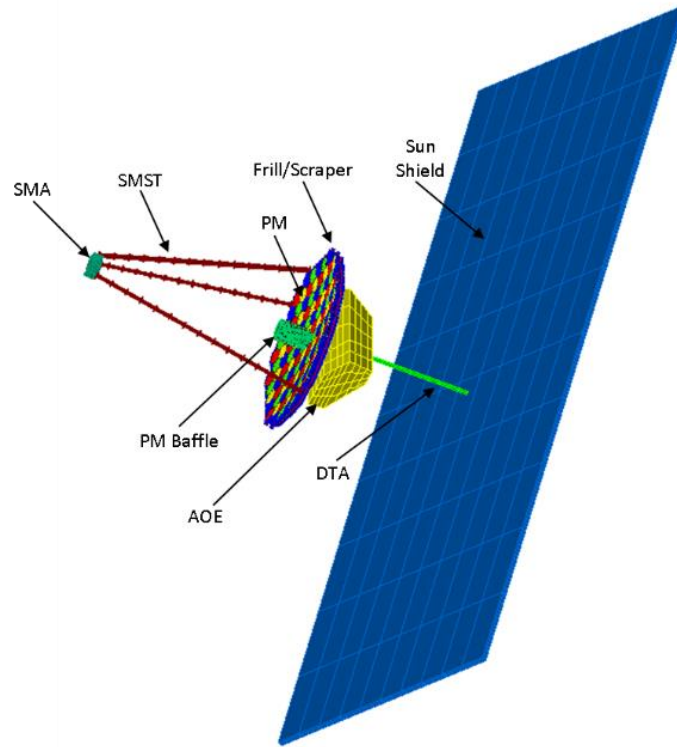
Figure 67: Telescope Model for evaluating thermal transient effects.

Table 21 summarizes the material properties that have been applied throughout the thermal model and **Table 22** summarizes the optical properties.

Table 21: Material Properties for thermal model.

Material	k W/(mC)	cp J/(kgC)	ρ kg/m³	α(mm²/s)
Aluminum 6061 T6	167.3	896.0	2698.8	69.2
Kapton	0.2	1004.4	1410.0	0.1
Composite (M55J / M40)	33.9	880.2	1661.5	23.2
ULE	1.3	766.2	2128.6	0.8

Table 22: Optical Properties for thermal model.

	e	a	a/e
Aluminized Kapton, Al side	0.03	0.12	4
Black Kapton	0.88	0.92	1.05
Composite M55J/M40 Bare	0.8	0.93	1.16
ULE Bare	0.8	0.8	1
ULE Mirror Surface	0.025	0.06	2.4

10.3 Mirror Materials

The trade among three mirror substrate materials -ULE®, ZERODUR® and Silicon Carbide (SiC) – for the PMSAs considers cost, schedule, risk, static performance, and stability performance. Manufacturability, process, integration, and other needs must also be considered. PMSA stability effects that are driven by mirror substrate material largely have to do with system high-spatial frequency errors, which include segment-level power and higher order segment-level zernikes. The segment tip, tilt, and piston stability effects will not largely be driven by substrate material, except by way of mass and thermal characteristics. Instead, the tip, tilt and piston stability effects will largely be driven by performance of the mount assembly, adhesives, support structure, and backplane phenomena. For the secondary mirror, tertiary mirror, and other aft optics, the substrate material selection may drive more than system high-spatial frequency errors, including system low- and mid-spatial frequency errors.

Manufacturer design guidelines were used to generate sample mirrors with identical natural frequencies. This is one of several possible approaches to "leveling the playing field" between differently designed mirrors. Other metrics could have been used to normalize this include mass, global bending stiffness, gravity sag, or surface figure response to a given load. Designs were formed based on manufacturing process, and an attempt was made to best meet typical requirements consistent with launch survivability and UV-surface quality performance for each substrate material design – the resulting finite difference plate models are shown in **Figure 68**. The ULE® design was made using Harris principals of lightweight design and advanced manufacturing. The ZERODUR® design was conceived with some consideration to cost-optimized methods extending the solution space of lightweight spaceborne monolithic ZERODUR® mirrors to larger sizes.[42] The SiC design was formed based on recommendations and rules of thumb from a manufacturer of large lightweight silicon carbide mirrors. The models were made with care to include representation of the parasitic fillet masses which are inherent to lightweight substrate manufacturing approaches.
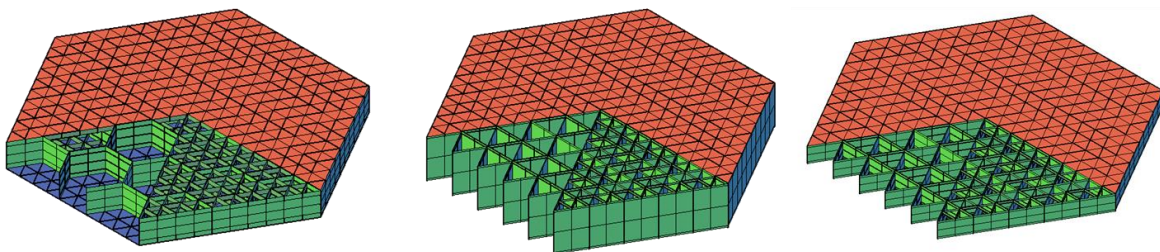
Figure 68: Concept Level LUVOIR PMSA Designs. (From Left to Right) ULE® Design, ZERODUR® Design, SiC Design Note: sections of the front face and cathedral are removed for clarity.

Oftentimes, mirror substrate materials are compared by material properties, which are readily established and available. Material property metrics like CTE are used to compare thermal stability between mirror materials. More sophisticated methods are applied, dividing CTE by thermal conductivity or thermal diffusivity to create a stability metric. Taking one step further, this report

---

[42] Antoine Leys, Tony Hull, Thomas Westerhoff, "Cost-optimized methods extending the solution space of lightweight spaceborne monolithic ZERODUR® mirrors to larger sizes," Proc. SPIE 9573, Optomechanical Engineering 2015, 95730E (2 September 2015); doi: 10.1117/12.2187099

seeks to compare properties and performance of mirror designs which use each material. **Table 23** describes some characteristics commonly compared for the three mirror concepts.

Table 23: Performance Characteristics of Concept PMSA Substrate Designs

|	Substrate Mass	1st mode free-free	Construction	CTE * Steady State Gradient	Global Bending Stiffness
Units	(kg)	(Hz)	-	(ppb)	(kg-Hz^2 x10^6)
ZERODUR®	38	544	Open Back	38	11
ULE®	16	544	Closed Back	36	4.7
SiC	15	544	Open Back	460	4.4

Each material has certain advantages.

- SiC advantages
  - Significantly lower gradient responses through LF1 and LF2
  - Lower bulk responses through LF1
- ULE® advantages
  - Lower gradient and bulk responses in LF2, LF3 and MF
  - Plate matching is highly effective at reducing bulk responses, especially important in LF1
- ZERODUR® advantages
  - Potentially lower CTE and better CTE-uniformity
  - Comparable responses to ULE® and SiC
  - Opportunity to reduce responses, if thinner design with lower natural frequency can be tolerated, which presents a trade with dynamic stability

It is interesting to note that CTE and CTE non-uniformity effects have different influences across the time- and spatial- domains. For example, a local high CTE region in a mirror backplate may be activated by PMSA heaters in the MF domain. but if the same region existed in the mirror front plate, it may have no response. It is important to appreciate these nuisances while relying on modeling and analysis to verify time- and spatial- domain based stability allocations.

10.4 Mirror Mass

Discussions with instrument designers and the LUVOIR STDT led to a notional understanding of how PMSA mass will impact system needs. The discussion evolved in the context of payload capacities of several next-generation launch vehicles, and the need to have a credible mass budget for LUVOIR A. The result was an understanding that if the PMSA design exceeds a certain mass, as illustrated in **Figure 69**, instruments must be removed or reduced to meet the system mass budget. Note that the PMSA mass estimate includes mirror substrates, mount pads, flexures, composite reaction structures, interfaces, rigid-body-actuators and cabling.
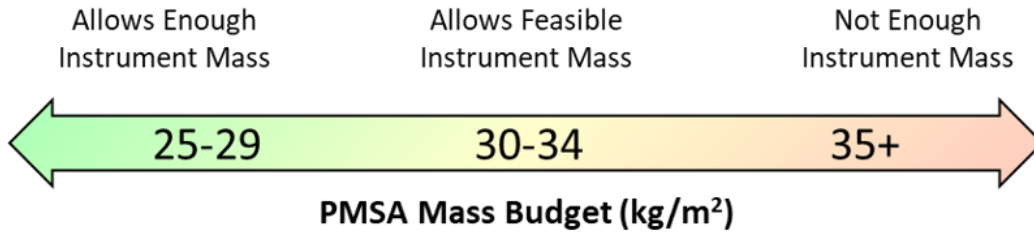
Figure 69: Notional Mass Budget for LUVOIR PMSAs and expected impact on available instrument mass.

Sacrificing or reducing instrument payloads will impact the science LUVOIR A can deliver. The standard design and maturation cycle of a mission will gradually restructure and distribute contingency in the mass budget, which will significantly change this perspective on the influence of PMSA mass.

It is informative to discuss PMSA mass in terms of areal density (or mass per area); this terminology allows for fair comparison of different size segments and apertures. State of the art lightweight mirror manufacturing enables UV-quality mounted mirror assembly masses of 30-34 kg/m^2. Harris has previously demonstrated 10 kg/m^2 glass mirror substrates. When comparing areal density across different hardware and applications, it is important to note the scope of the hardware mass that is accounted for in the areal density, whether the mass includes the substrate alone, or the entire mounted assembly. According to initial LUVOIR A mass budgets, as of the LUVOIR Interim Report, this PMSA mass range allows feasible mass allocation for the LUVOIR A instrument packages.[37] For context, the initial LUVOIR A mass budget was made by the GSFC LUVOIR Study Team using conservative mass contingency factors and the constraint of a payload mass that must fit within the predicted payload capacity of at least two next-generation launch platforms. This context drove the annotations above **Figure 69,** which communicate an understanding of how PMSA mass could impact available instrument mass. The 30-34 kg/m^2 assembly mass considers that a rigid substrate is needed to meet UV-quality static and dynamic WFE requirements.

10.5 Mirror Mounting

Mirror mount pad assemblies serve as the connection which binds the substrate to the rest of the telescope. The mount pad assembly is typically the closest structural component to the optical surface that has a high coefficient of thermal expansion. As a result, the mount pad assembly is a key driver of wavefront error effects from higher-order (astigmatism, trefoil and beyond) bending of the mirror surface.

Struts also play a major role in rigid body motion of PMSA's, including piston, tip, tilt and decenters. Each strut must have a significant lever arm about the mirror vertex, to rigidly support the mirror and maximize the natural frequency of the assembly, improving the dynamic stability performance. However, this significant lever arm means that any growth or shrink of mirror struts due to thermal, creep, hygroscopic or other loads will cause a significant rigid body motion of the mirror.

Analysis predictions describe how thermal loads and invar growth impact stability of the PMSA as a function several different mount designs. One aspect of mount design explored is a simple

invar flexure as compared to a fine-tuned athermalized flexure design. Another aspect of mount design explores a trade between thick, soft RTV bonds as compared to an ultra-thin stiff hydroxyl bond. Hydroxyl bonding has shown some promise in ultra-stable applications and has been proposed for use in the ultra-stable Laser Interferometer Space Antenna, LISA. While hydroxyl bonding may provide a significant advantage with respect to thermal stability for a ULE® bond pad, this may not be the case for an invar bond pad, as is used in our model. While RTV has an enormous CTE compared to other components in the assembly, it is soft enough to relax the influence of the neighboring rigid invar bond pad on the glass, which leads to an overall benefit in residual mount errors. The rate of invar growth (or creep) is relatively well known and was found to be a non-driver for all designs.

The PMSA FEM design shown in **Figure 65** was altered and evolved from the baseline, with significant benefit in terms of bulk temperature response, as shown in **Table 24**. The baseline case included an RTV bond and simple invar strut. The design was altered to include a hydroxyl bond and to include athermal struts. The athermal struts have a significant positive influence on rigid motions, and the RTV has a significant positive influence on residual errors, shown as "RMS Pwr Removed" in **Table 24**. These features are recommended for the PMSA design.

Table 24: Sensitivities to Bulk Thermal Loads for Different Mount Designs

| 1 mK Bulk Delta T Sensitivity				
Degree of Freedom	Baseline	Hydroxyl Bond	Hydroxyl + Athermal Strut	Athermalized Struts + RTV Bond
Surface Piston	1487.5 pm	1094.8 pm	56.0 pm	1.2 pm
Surface Tilt	12.9 p-rad	13.3 p-rad	2.6 p-rad	6.9 p-rad
Surface Decenter	11.3 pm	11.4 pm	1.3 pm	5.2 pm
Pico Radians Clocking	26.9 pm	27.3 pm	4.3 pm	13.7 pm
RMS Mid SF WF	0.5 pm	32.6 pm	35.2 pm	2.3 pm
RMS High SF WF	1.6 pm	19.9 pm	24.0 pm	0.4 pm
RMS Power WF	0.5 pm	31.6 pm	36.7 pm	2.4 pm
RMS Astig WF	0.1 pm	0.1 pm	0.0 pm	0.1 pm
RMS WF Tilt Removed	1.6 pm	36.3 pm	42.6 pm	2.4 pm
RMS Pwr Removed	1.6 pm	19.9 pm	24.0 pm	0.4 pm

10.6   Thermal Effects

The analysis presented in the following sections demonstrates that thermoelastic effects should meet the PMSA stability budget, given thermal control on the order of 3.1 mK over a 10-minute period. This is true when the system is "in control," but not necessarily true after a slew event. The potential delay during which the OTA "quiets down" after a slew is also evaluated and discussed. Slowly drifting effects have also been evaluated, and can be made to be negligible using high-TRL solutions within the existing state of the art.

The highest-risk thermoelastic effects must be controlled on the order of seconds and minutes, up to a few hours to maintain imaging performance. These high-risk effects largely consist of high spatial-frequency residuals from the control systems which are in full effect at these rates. Faster cycling effects are greatly attenuated by OTA heat transfer responses. Slower effects do not generate gradient changes in the OTA and these are passively managed with athermal designs.

10.6.1 Thermal Sensitivities

Figure 70 illustrates the WFE maps with power removed for the effect of 1 mK ΔT in bulk, axial and lateral gradients. The results shown are for the starting baseline design and do not include the impacts of the athermal design of the mirror struts.
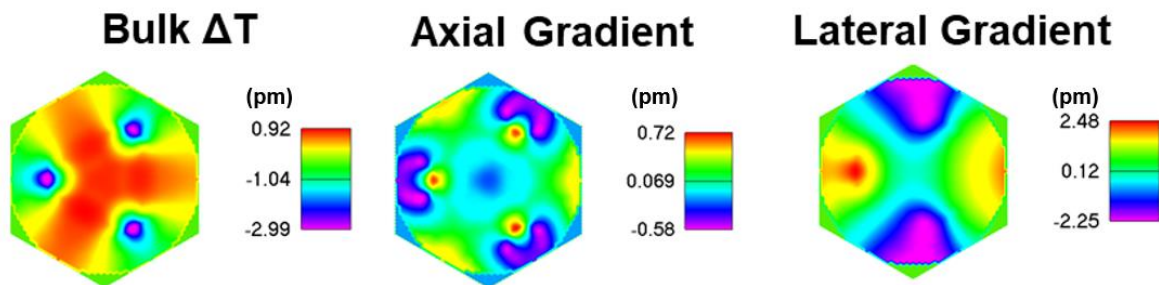
Figure 70: WFE Maps (power removed) due to thermal changes in mounted PMSA temperature.

The results of the analysis describing the impact of the mirror CTE distribution are shown in **Figure 71**. The residual error illustrates interaction between CTE distribution in the glass and the hexagonal mirror core pattern. Given the high spatial frequency natures of this error, it is expected to map to larger radii in the coronagraph dark hole, where there is additional relief in the error budget.
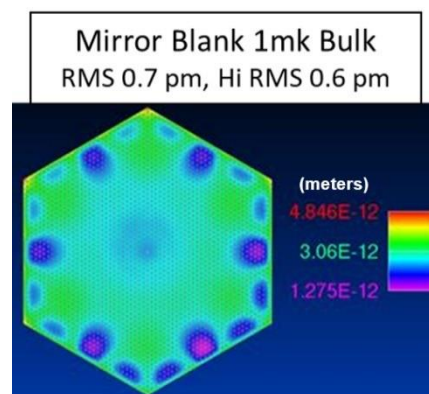
Figure 71: Impact of Mirror Blank CTE Distribution.

87

10.6.2 Thermal Time Constants

Using the thermal transient observatory model from Section 10.2, the impact of varying heat loads into different parts of the observatory was calculated. These calculations were converted to transfer functions so the time constant of different parts of the observatory to the given heat variation can be determined.

In the first case, the base power applied to the PMSA heaters of 2505W was varied +/- 100W at specified periods from 1,000 days to 1 second. All other loads were fixed. At steady state, this load produced a maximum system response of 2.322°C. The Bode plot in **Figure 72** calculates a gain based on this maximum response. This was done so that system time constants can be easily calculated. The results show PMSA Heater LF1 variations must exceed 10K PTV to create a 1 mK PMSA gradient response and must exceed 0.1K to create a 1 mK PMSA bulk response. Since the gain decreases with frequency, the required change in temperature to produce an equivalent response increases.

In the second case, the base power applied to the solar load of 1,230W/m^2 was varied +/- 49 W/m^2 at specified periods from 1,000 days to 1 second. All other loads were fixed. The response of the PMSAs even at low frequencies is so low, as seen in **Figure 73**, that this is not expected to have an impact on the wavefront error budget. Other loads applied at PM Baffle, the PM Scraper, and the SMA showed similar, negligible results.

These sensitivities can be used to solve for allowable power fluctuations within the system to maintain a given wave front error limit. When combined with duty cycle knowledge, they can inform which electrical componentry will play an important role in driving system thermal distortions. At the least, these results help set a lower limit on the power fluctuations that can play a role in influencing the system's temporal response. In doing so, they help bound the thermal prediction problem, giving the analysis a method for showing that, above a given frequency the system will not response fast enough to influence overall system wave front error.
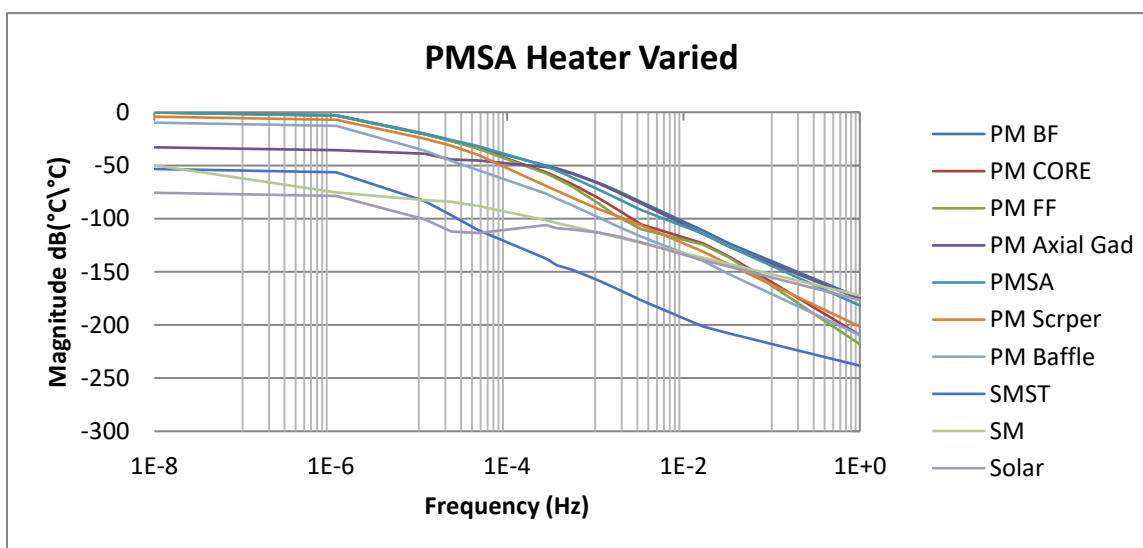

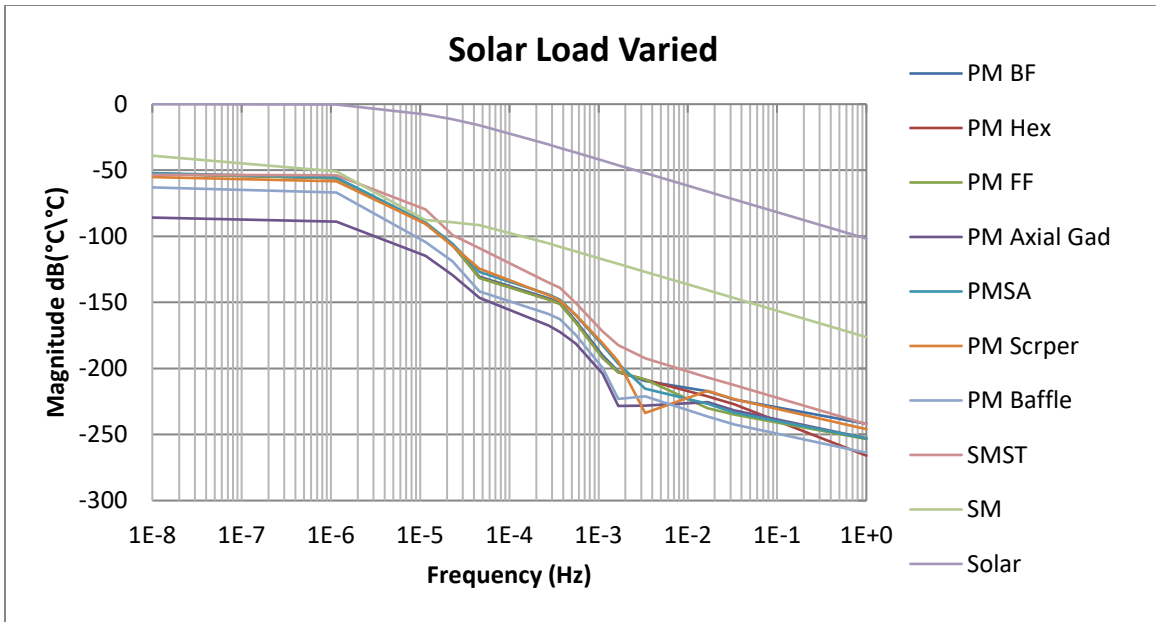**Figure 72: Bode Plot for thermal response to PMSA Heater cycling.**

Figure 73: Bode Plot for thermal response to Solar Load Variation.

These results should remind the reader that all thermal systems behave as powerful low pass filters, in that the faster the period the lower the system response. For example, in the MF and HF frequency bands, responses to heater loads are attenuated by many orders of magnitude. It is also clear that ultra-thin or lightweight components experience the most significant response to fast thermal inputs, and that all responses significantly attenuate thermal inputs in the HF and MF bands. The significance of ultra-thin components, and fast thermal inputs, if any, can be established with more detailed modeling of thermal environments and control systems.

10.6.3 Allowable Temperature Changes

The error budget is used to calculate the allocations for thermal changes that equal [the requirement value /√2] for each effect. A calculation of the allowable change in the following parameters is presented for:

1. Bulk change in PMSA temperature and the calculated rate in mK/h
2. Bulk change in mirror temperature and the calculated rate in mK/h
3. Axial mirror gradient change and the calculated rate in mK/h
4. Lateral mirror gradient change and the calculated rate in mK/h

The allowable thermal variations can be found in **Table 25**. It's important to look at both the actual calculated ΔT and the rate of change to understand the limitations. When evaluating for example the allowable change in bulk ΔT over the mid temporal frequency (MF), the calculated ΔT is only 0.064 mK, which would appear to be an exceptionally small number. But for that change to occur over a 1-second duration, the rate of change is greater than 500 mK per hour. The maximum tolerable rate of change in bulk temperatures is 2.4 mK per hour and the maximum tolerable change in axial gradient is 5.3 mK per hour.

Table 25: Allowable Change in Mirror Temperatures.

Tolerable mK change and rate of chage over spec duration		Acceptable Bulk Change in PMSA Temperature		Acceptable Bulk Change in Mirror Substrate		Axial Gradient Temp change in PMSA		Lateral Gradient Temp change in PMSA	
Alloc	Duration	mK Change	mK/Hour Rate	mK Change	mK/Hour Rate	mK Change	mK/Hour Rate	mK Change	mK/Hour Rate
LF1	86400 s	114.5 mK	3.4 mK/h	80.4 mK	2.4 mK/h	165.5 mK	6.9 mK/h	351.9 mK	10.4 mK/h
LF2	1000 s	4.5 mK	11.4 mK/h	3.1 mK	8.0 mK/h	1.5 mK	5.3 mK/h	13.7 mK	34.9 mK/h
LF3	100 s	4.5 mK	113.6 mK/h	3.1 mK	79.8 mK/h	1.5 mK	53.0 mK/h	13.7 mK	>500 mK/h
MF	1 s	0.064 mK	>500 mK/h	0.045 mK	>500 mK/h	0.040 mK	>500 mK/h	0.195 mK	>500 mK/h
HF	0.1 s	0.064 mK	>500 mK/h	0.045 mK	>500 mK/h	0.003 mK	>500 mK/h	0.034 mK	>500 mK/h

It should be noted that the bulk change in temperature and mirror substrate temperature are quite similar (4.5 mK versus 3.1 mK) over LF2. These are both limited by the high spatial frequency WFE allocations. In fact, except for the axial gradient all the limits are due to the high spatial frequency WFE allocations. The axial gradient is limited by the change in mirror piston which could be improved by a more advanced athermalized design. Gradients may take other forms in operating conditions, and these will affect different WFE stability responses than the basic gradients discussed here.

Correction for Updated Stability Budget: The LF1 allocations are reduced by an order of magnitude in the updated error budget, so the allowable rate will be similarly reduced. The tightest case becomes 0.24 mK/hr for the bulk temperature change of the mirror substrate. However, these requirements are driven by high spatial frequency allocations, which based on the PSD analysis approach will have relief compared to the WFE budget. This analysis will need to be refined in the next phase to account for both effects. Magnitudes are still in the range of ~1 mK so this is not a significant gap – it may require some additional engineering or a larger part of the error allocation.

10.6.4 Slew Phenomena

Each time the telescope slews, the thermal boundary conditions will change for the primary mirror. For example, a change from 0° to 30° exposes the front face of the primary mirror to more of the cold of space, and less of the sunshield; for the rear face of the primary mirror, the opposite is true. This new thermal boundary condition acts as a thermal shock to the system. It can be mitigated by adding layers to the sunshield, but no matter how many layers are added, the appearance of the cold side of the sunshield cannot be made to be identical temperature to the cold of space.

This thermal shock associated with a slew will cause temperatures to change rapidly in the mirror assembly at first, but over time the system will settle as it reaches a new steady state. Analysis using Harris' thermal model indicates that smaller slews result in smaller stability impacts, which is relevant as LUVOIR con ops are planned. Analysis also indicates that some slews may have lesser or different impact on stability if they are executed by attitude control of the spacecraft relative to the sun vector, instead of by attitude control of the OTA This opportunity for enhanced stability should be explored and better understood.

The spacecraft thermal model can predict settling over time following a slew event, given a system of proportional heater control zones. One such prediction is shown in **Figure 74**, based on a LUVOIR-A system thermal model. The thermal modeling process is now able to evaluate how all 120 mirror segments respond to a slew, in terms of temperature rates of change in bulk average and in through-thickness gradients. The process evaluates responses over the course of an

exposure, with bracketing for each of the time-domain requirement ranges (LF1, LF2, LF3, MF, HF). **Figure 74** indicates waiting a certain period before beginning an exposure can improve stability over the course of an exposure, as is expected. Once the sub-allocation for settling is defined, this model can predict the duration that LUVOIR must wait before starting an exposure, after a specific slew event.
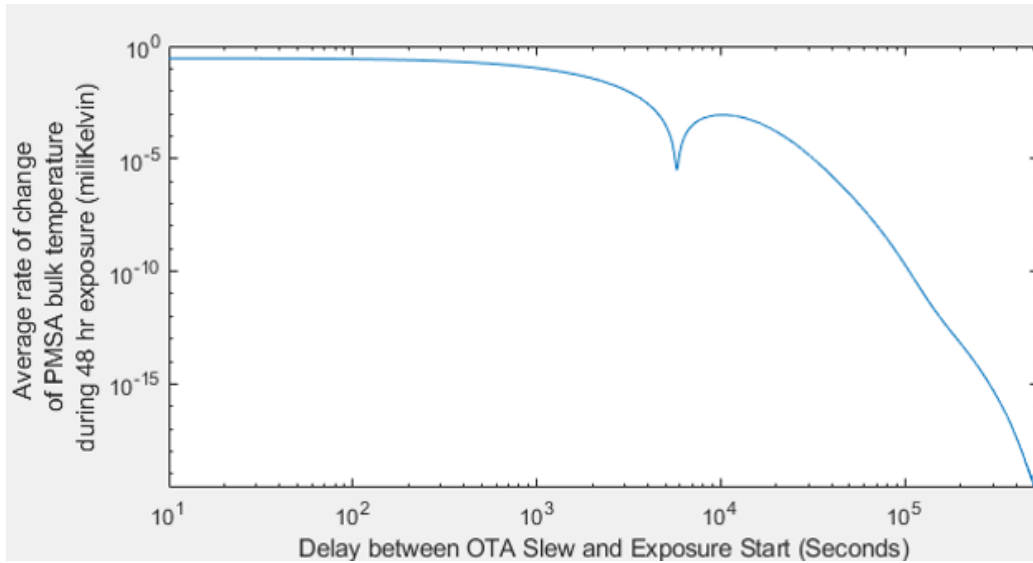
Figure 74: PMSA Settling After a Slew Event. An increased delay between the slew and the start of the science exposure increases expected mirror stability.

10.7 Dynamics

Dynamic stability performance of the mirror substrate is linked to stiffness, but also to density, mass and the natural frequencies of the mirror assembly. These natural frequencies are greatly influenced by the mirror mounts and struts, whose stiffness will play a substantial role in overall PMSA dynamic responses.

10.7.1 Dynamic Input Limits

This section will define acceptable limits for accelerations applied to the PMSAs. With a substrate first free-free mode of 544 Hz for the baseline design, there is very little dynamic energy expected that will excite substrate modes in the lightweight mirror assembly. To simplify this evaluation, all input dynamic disturbances are treated as scaled quasi-static accelerations. **Table 26** describes the values involved in calculating the maximum acceleration input in each band which will not exceed stability requirements.

Table 26: Calculating the Maximum Allowable Acceleration Inputs in Each Band.

Band	LF1	LF2	LF3	MF	HF
How Much Acceleration is Acceptable (μ-g rms)	0.078	0.20	11	11	1161
F_H-F_L(Hz)	0.001	0.009	0.99	49	9950
Acceptable Mean g^2/Hz Across Band	6.08E-12	4.44E-12	1.22E-10	2.47E-12	1.35E-10

The maximum allowable μGrms allowable inputs are determined for each band, based on the allowable errors in that band, and the FEA predicted acceleration responses of the mirror assembly. These allowable maxima were combined with the width of each frequency bucket to establish a mean acceptable g^2/Hz acceleration input across each band. This process follows the steps prescribed by the NASA FEMCI standard.
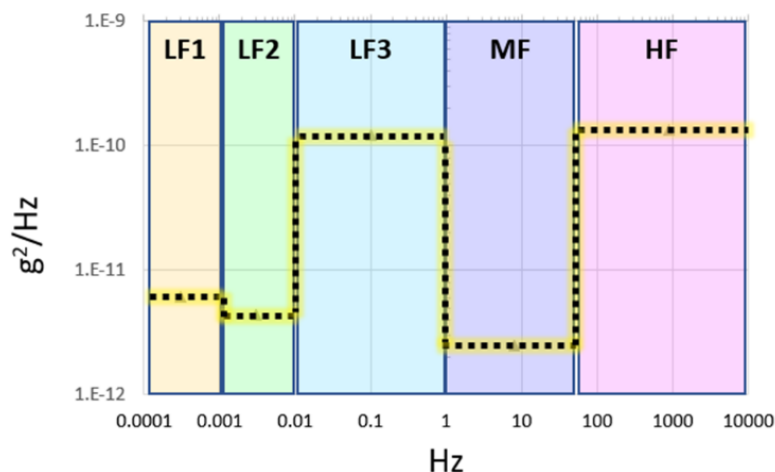
Figure 75: Allowable Acceleration Spectral Density Input at the Base of the Mounted PM Substrate – Mean Allowable Magnitude Plotted for Each Frequency Band.

Figure 75 shows maximum allowable ASD input for the PMSAs for each frequency band defined in the stability budget. The plot assumes the input is flat across the bucket, so while spikes in the acceleration input may exceed these limits, so long as the ASD within that bucket is largely below

the line, stability requirements are met. There was also some limited analysis done to consider the transmittance of the PMSA as a spring-mass-damper system; there are two key takeaways for this phenomenon. First, for frequencies exceeding the PMSA first mode, the PMSA can tolerate even higher inputs than shown in **Figure 75**, as it naturally attenuates higher frequency inputs. Second, for frequencies near the first mode, we should consider the effective damping of the PMSA, and consider whether our tolerances near PMSA natural frequencies may be even tighter than those shown in **Figure 75**, due to PMSA resonance.

This analysis only accounts for the stability budget, optic sensitivities and maximum allowable dynamic disturbances input to the PMSAs; to make meaningful conclusions about dynamic stability meeting allocations, analysis must also system disturbances, controls and passive isolation and damping.

Correction for Updated Stability Budget: The LF1 allocations are reduced by an order of magnitude in the updated error budget, so the allowable limits will be similarly reduced. However, it is not expected that there is significant dynamic input at these very low frequencies.

10.7.1 Launch Survivability

For mirror assemblies, launch survivability is typically driven by the mount assemblies and mirror substrate regions near the mount interface. This is especially true of the brittle substrate materials under consideration: ULE®, ZERODUR® and SiC. This study did not develop high-fidelity stress models, as are typically used to inform launch survivability. This challenge can be met as mirror assemblies in this areal density range have flight heritage. For all analysis that depends on mount geometry and configuration, components were sized based on hand calculations and rules of thumb for meeting survivability requirements. In mirror mount designs, there is always a trade between performance and survival margins. The limited level of effort to address survivability is consistent with the concept level and uncertainty of launch environments.

10.8   PMSA Surface Figure Control

Surface figure control actuation (FCA) is a concept of actively using actuators to try to bend a mirror surface to the ideal optical prescription. There are two ways this might be implemented in LUVOIR PMSAs. First, these actuators might be adjusted to correct fabricated mirror errors and environmental errors and fixed in place. Second, these actuators might actively be used to correct on the order of picometers over the course of an exposure. Both options offer powerful opportunities and consequences for PMSA figure.

In terms of stability, passive FCA will have numerous effects. Because FCA interfaces to the mirror at more than six points, it causes the mirror system to be over-constrained, and prevents the interface from being kinematic. This means any phenomena in the rigid backplane or phenomena in the actuators and struts will bend the mirror surface. To a first order, a well-flexurized kinematic system of six supports will not cause any mirror bending, no matter how the backplane, struts, or rigid body actuators deform. If the FCA is actively controlled, this impact can be overcome on time-scales that are slower than the control loop, because the FCAs are flexurized to only act on the mirror in one DoF, so if the force in that DoF is controlled to be stable, the control loop will mitigate most of the instability associated with the non-kinematic mirror support.

If active FCA is used to actively control figure on the order of picometers over the course of an exposure, several additional challenges are encountered. Inherent control residuals will impact

stability, including hysteresis, control noise and errors, resolution limited step phenomena, repeatability and accuracy of the actuators. Analog-to-digital converters that are flight qualified do not currently address the needs for FCA range of motion and FCA picometer-class resolution. The wavefront sensing and control feedback must be able to give adequate feedback to drive the FCA array at the picometer level across all 120 LUVOIR-A segments, which is currently beyond the state of the art.

FCA is not recommended for the LUVOIR baseline design because of their uncertain impact on stability. FCA should be reserved as an alternative option but is not a clear enabler of picometer class stability.

10.9 Mirror Sub-System Technology Gap Assessment

Based on the wavefront stability error budget, maps were generated showing how technologies and design features each stand to benefit different parts of the spatial- and time-domain spectrums, laid out in **Figure 76**. The intent is that these will provide relevant guidance even as the system controls and stability budget evolves. Predictions are rough order but are based on analysis results where available. For example, ULE® plate-matching is a powerful tool to address LF1 thermal effects which act as bulk temperature changes on the mirror assembly, it is less effective at addressing HF thermal effects, during which the plate temperatures do not necessarily track together.

PMSA Pico Figure Actuation

	lo	mid	hi
LF1			
LF2		Up to 50x	
LF3			
MF			
HF			

PMSA Pico Rigid Actuation

	lo	mid	hi
LF1			
LF2		10-100x	
LF3			
MF			
HF			

Hydroxyl Bonds

	lo	mid	hi
LF1			
LF2			
LF3		Up to 15x	
MF			
HF			

Athermal Struts - SwitchBack

	lo	mid	hi
LF1			
LF2		Struts Approach	
LF3		'Fully Stable'	
MF			
HF			

PMSA On-Board Thermal Control Module

	lo	mid	hi
LF1			
LF2			
LF3		10-100x	
MF			
HF			

ULE Plate-Matching

	lo	mid	hi
LF1			
LF2		>10x	
LF3			
MF			
HF			

Additive Mirror Bond Pads

	lo	mid	hi
LF1			
LF2			
LF3		>10x	
MF			
HF			

Expansion-Neutral Integration-Tolerant Adhesive Joints

	lo	mid	hi
LF1			
LF2		Joints Approach	
LF3		'Fully Stable'	
MF			
HF			

Predictive Thermal Control

	lo	mid	hi
LF1			
LF2		>2x	
LF3			
MF			
HF			

Substrate CTE (Control, Knowledge, Uniformity)

	lo	mid	hi
LF1			
LF2			
LF3		Up to 10x	
MF			
HF			

Additive Substrates

	lo	mid	hi
LF1			
LF2			
LF3		Up to 2x	
MF			
HF			

Athermal Struts - Negative CTE

	lo	mid	hi
LF1			
LF2		Struts Approach	
LF3		'Fully Stable'	
MF			
HF			

Figure 76: Impact of various technologies on spatial-temporal buckets in the wavefront stability budget.

The following list presents a summary of the analysis areas studied and the technology gap classification. There are no technology gaps identified in the area of Stable Mirrors, but significant

engineering work will be required to meet the demanding performance needs in a timely and cost-effective manner. There is a mid-TRL technology gap in the area of Stable Mirror Mounting.

Mirror Gap	Classification	Rationale
UV Quality Glass Mirrors	No Gap	o The analysis has not revealed any major shortcomings given the current light-weighting and polishing capabilities of UV quality glass mirrors.
Material Property Measurement	Engineering Gap	o Need method to more accurately measure material CTE (ULE/Zerodur/SiC)– both bulk and spatial distribution. o Improve uniformity of ULE CTE in manufacturing process.
Integrated Modeling	Engineering/ Knowledge Gap	o Continued system level modeling to understand the magnitude and time constant of the thermal changes anticipated on orbit (especially where expected deformations are close to the stability budget limits). o Investigate potential impacts of Predictive Thermal Control, varied PMSA heater geometries o Include study of coating effects, which may be the dominant phenomena in the MF, HF and other bands.
Mirror Mounting	Mid TRL Gap	o Include segment-level sensing & control/metrology features to the design and evaluate thermal/dynamic impacts. o Vary mounting pad geometry to take advantage of stability relief at higher spatial frequencies (PSD based approach).
Picometer Figure Control Actuation	(Potential) Low TRL Gap	o The impact of FCA on stability is not known. Given the potential complexity to implement, FCA is not recommended unless future iterations of stability budgets and trades studies prove it is required.

11 Ultra-Stable Monolithic Primary Mirrors

Because the focus of the ROSES D.15 solicitation was on > 10 meter segmented aperture telescopes, the ULTRA team chose LUVOIR Architecture A as the baseline design for this study. However, the results presented in this report are certainly applicable to other large, ultra-stable segmented designs as well as ultra-stable monoliths. For example, the HabEx mission concept also includes a high contrast coronagraph that will require a picometers-level ultra-stable telescope.[3] While the primary mirror is monolithic rather than segmented, which eliminates some sources of instability, the following areas of the ULTRA study are still highly relevant for the system architecture:

- Temporal regimes of concern (Section 3.2) – "Quasi-static" errors that cause speckle evolution on the order of a coronagraph exposure are still the most confusing when trying to detect a planet; the available active and passive control systems may be different for a monolith versus a segmented primary which may shift the bandwidth of the driving regimes.
- Spatial regimes of concern (Section 3.2) – a monolith can still have mid-spatial instabilities that results from thermal and dynamic perturbations to its many-point mounting structure.
- PSD based error budgeting (Section 4.6) – this approach will provide maximum relief on the sub-systems by considering the spatial energy distribution in the coronagraph dark hole.
- Thermal and Dynamics inputs (Section 5)– the sources of instability from the environment and spacecraft are comparable, and will have similar impacts on global mirror stability.
- Beam Walk and LOS analysis (Section 6)– the results depend on the specific telescope design but approach and temporal considerations are similar.
- Global active sensing and control (Section 7) – the need for relative positioning of the PM-SM (via a laser truss or similar) are comparable.
- Thermal sensing and control (Section 7.7)– the needs for large-scale structural and optical thermal stability are comparable.
- Ultra-stable structures (Section 0) – the needs for material CTE and CME performance, backplane stability are comparable.

12 Technology Development

12.1 Classification of Technology Gaps

Technology gaps are defined as areas where the system performance cannot meet the system allocation. As a reminder, the gap nomenclature used in this report is defined in **Table 27**.

Table 27: Classification of technology gaps.

Knowledge Gap	Do not have measurements or knowledge of performance at the picometer level, but do not know of anything yet that will cause an issue. May transition to Low- or Mid-TRL gap as knowledge is gained.
Low-TRL Gap	Technologies are identified but need development to show they are feasible.
Mid-TRL Gap	Current technologies appear feasible but need to be proved in flight-like ways through brassboards.
Engineering / Manufacturing Gap	A solution is available, but it takes engineering and process work to make sure it can be built to cost and schedule.
System-Level Gap	Components or subsystems have been proven but need to be integrated into a larger system to characterize interactions.
Architectural Show Stopper	No known technologies can provide a solution.

12.2 LUVOIR Technology Gaps

Based on the analysis presented in the previous sections, each of the technology areas relevant to LUVOIR has been rated for the current TRL level and technology gap classification as in **Figure 77**. For each classification, we have provided a general path forward to advance the TRL.

Given the maturity of the stability budget and the change of approach to PSD, additional work is needed to quantify the specific performance enhancement for some technologies (i.e. 2x vs. 5x improvement). However, we do not expect the general classifications to change.

Area	Active Sensing & Control				Low Disturbance			Structures			Mirrors and Mirror Mounting					Path Forward for TRL Advancement
Technology	Segment Dynamic Sensing & Control	Laser Metrology	System Control Methodology	Thermal Sensing & Control	LOS Stability	Payload Isolation	Low Disturbance Mechanisms	Stable Composite Structures	Microdynamics	Stable Joining (Hinges/Latches)	Stable Mirrors	Mirror Mounting	PMSA Figure Actuation (if needed)	Coronagraph Design (LOWFS/HOWFS)	Infrastructure/ External Metrology	
Current TRL	3	5	2	4	3	5	2	5	2	4	5	4	3	4/5	-	
Knowledge Gap	X		X	X	X		X		X	X		X	(X)			Analysis/ Measurements
Low-TRL Gap	**X**		**X**		**X**								**(X)**			**Component-Level Demo**
Mid-TRL Gap				**X**						**X**		**X**				**Analysis/ Subsystem Demo**
Engineering Gap		X				X		X			X				X	Analysis
System-Level Gap		X				X			X			X				System/ Subsystem Demos
Showstopper																Unknown

Figure 77: ULTRA Study Technology Gap List. Includes current TRL, gap classification, and suggested path forward for TRL advancement. Low TRL gaps (2-3) are the highest priority for near term investment and the immediate path forward is a component level demonstration.

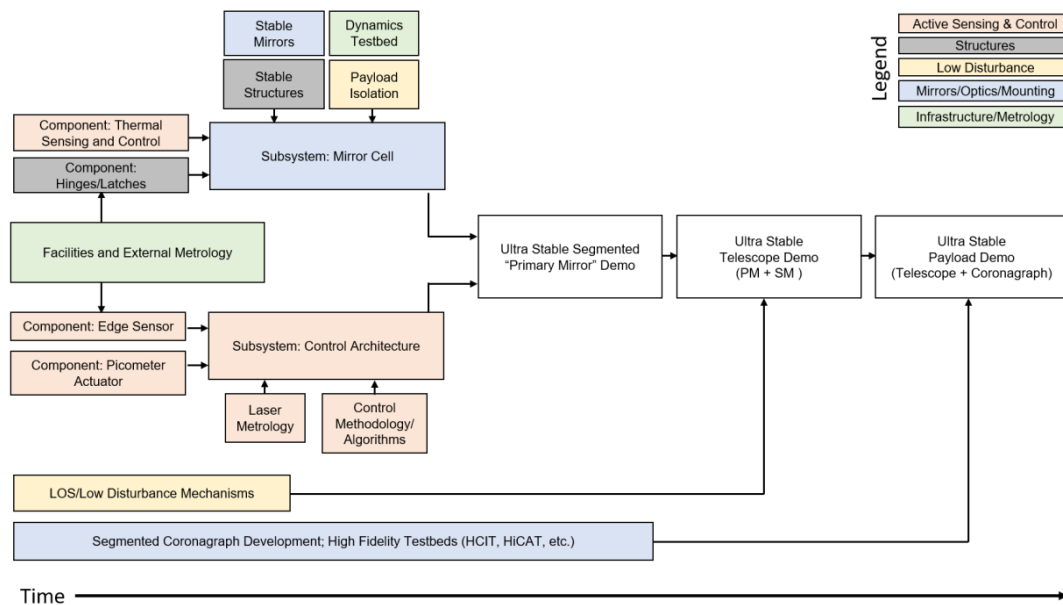## 12.3   Technology Roadmap for Ultra-Stable Systems

The recommended path for technology development for ultra-stable systems is:

1. Increase component TRL
2. Characterize interactions of sub-systems
3. Increase system TRL

Given this path, a detailed roadmap to develop an ultra-stable telescope and coronagraph is shown in **Figure 78**. It begins with demonstrations of two types:

1. Components/subsystems rated as low- and mid-TRL that are required for the stability architecture (ex. Segment sensing and control).
2. Materials and components identified as knowledge gaps so that we can ensure the classification of each technology as low-TRL, mid-TRL, or engineering is correct and complete (ex. Low disturbance mechanisms).

Once their performance in a LUVOIR-like configuration has been demonstrated, they flow into two sub-system testbeds. The first is a sub-scale mirror cell demonstrator that will tie together the optics, mechanics and thermal control to study the stability at the sub-system level. The second is a control system testbed using simplified surrogates of the optics and focuses on active sensing and control architectures to study the performance of nested control loops. The goal of these targeted testbeds is to test the performance of the optomechanical and controls sub-systems and to identify remaining gaps or areas of relief. Once the sub-systems have been demonstrated, they can flow into an integrated "segmented mirror" testbed, which will validate the stability of the phased PM, a "telescope" testbed which adds a secondary mirror to validate the stability of an aligned multi-optic telescope, and finally a "payload" testbed that validates that combined telescope + coronagraph stability.

Figure 78: Roadmap for technology and subscale system demonstrations for ultra-stable optical systems with segmented primary mirrors. This roadmap leverages work being done at NASA centers, universities and industry through a variety of programs (NASA ROSES, IRAD, etc.).

As the demonstrations increase in scale, they leverage existing facilities and testbeds at NASA, universities, and industry. The goal in planning for these demonstrations should be to combine resources to maximize return on investment, rather than duplicating testbeds at multiple locations.

There is a need to balance the most promising technologies with the existing cost and schedule resources. The full development path in **Figure 78** will take a significant amount of time and funding, so the ULTRA study team has identified several areas for near-term investment (the next 2-3 years) that are the highest priority for understanding and substantiating the technical and fiscal feasibility of LUVOIR, which are listed in **Table 28**.

Within these near-term activities, there are a few areas that are critical for success of the proposed LUVOIR A architecture. The results from the ULTRA study corroborate previous analysis that mid spatial frequencies (especially segment-level PTT) will be most damaging to contrast stability in the coronagraph. Thus, low-TRL active sensing and control technologies at the segment level should be given highest priority. In addition, an assessment of the structural stability due to microdynamics and other non-linear impulses as well as the LOS stability using DFP should also be investigated as soon as possible; if the results reveal SOTA techniques are not sufficient, other solutions are currently low-TRL. <u>These priorities will tackle the most difficult parts of the stability problem with the longest lead times first and provide a solid foundation for additional demonstrations and testbeds.</u>

Table 28: Priority areas that can achieve significant advancement in the next 2-3 years. The most difficult aspects of the stability problem and thus the highest priorities are underlined for emphasis.

Modeling/Analysis	- Cross check first order PSD-based stability budgets with end-to-end modeling. - Develop structural and thermal LUVOIR models rooted in known/expected material capability (these models could also be made available to the ultra-stable community as a common platform to evaluate other system elements; some models already in progress from STDT work). - Model nested controls systems.
Component/Subsystem Demonstrations	- <u>Prove stability of hinges/latches with simple deployable tube section, including microdynamics regime.</u> - <u>Prove LOS stability at milliarcsecond level (DFP).</u> - Prove millikelvin thermal sensing and control in structures, light-weighted optics. - <u>Prove picometer-level edge sensing in flight-like geometry at required bandwidth.</u> - <u>Prove picometer-level actuation at required bandwidth and loading; characterize induced dynamics.</u> - Prove integration of sensing/control technologies into PMSAs. - Prove stability of PMSA mounting approach. - Characterize stability of Mirror Cell Subsystem Testbed. - Characterize interaction of nested controls in Control Architecture Testbed.
Facilities/Metrology	- Continue investments in NASA and university facilities to advance precision metrology and environmental facilities capable of ultra-stable measurements. - Leverage above resources to complete component-level demonstrations in a relevant environment (including measurement of stability-related material properties)

12.4 Promising Future Technologies and Approaches (Blue Sky)

This study operates on the principle that existing materials and methods should be used when possible to leverage their flight heritage. If this were not the case, we might also consider the following technologies or approaches to reduce cost/schedule:

- Additive manufacturing for glass and structural composites
- Homogeneous material bonding and joining technologies (athermal performance)
- Efficient optical manufacturing (replication, near net shape machining, active figure control)
- Disturbance/stress free mirror supports
- Advances in photon-counting avalanche photodiodes
- Low-noise electronics
- Integral wireless or fiber onboard communication network to eliminate data cables
- Wireless (reactionless) electrical power transfer
- In space assembly and/or manufacturing

The work in this study to identify technology gaps may reveal which of the above technologies is truly enabling or could significantly impact cost/schedule. As our understanding of the coronagraph requirements, architectural "tall poles" and trade spaces advances, there will be opportunities to re-evaluate these "blue sky" technologies for possible inclusion in the system architecture.

In addition to these promising technologies, there are approaches to technology development that may also lead to cost/schedule/risk reductions. These include:

- Conduct ongoing Mission Architecture studies
  - Fundamental architecture trades can have the biggest impact on mission cost/schedule.
  - It is difficult to re-think the architecture once a program starts.
- Invest in mission and technology development early.
  - Parallel maturation of system architecture concepts, key components and sub-systems will allow programs to perform trades based on mature cost/performance estimates, rather than relying on assessment of "technical risk" for unproven technologies.
  - For a given component/subsystem need, parallel investment in multiple technology solutions can provide several valid options that can be weighted at the system level for the best programmatic solution.
- Engineering subscale system-level pathfinders (a key recommendation of this study)
  - Solve key technical and system-interaction problems well before program execution phase.
  - Efficient way to find "unknown-unknowns"
  - Examples: Webb Testbed Telescope, Webb Core Thermal Test Article, LISA Pathfinder
- Flight demonstrations of sub-systems
  - Overcome ground tests limits where picometer level accuracy may prove extremely difficult (put resources into pathfinder hardware, rather than GSE).
  - Example: Microgravity Experiments for 0-g unloading, microdyamics

- Consider Manufacturing Readiness Level, not just TRL.
    - Solving manufacturing issues can be as costly as technology issues.